



The role of molecular packing on carrier transport in liquid crystalline dyes

Der Fakultät für Mathematik und Naturwissenschaften
der Carl von Ossietzky Universität Oldenburg
zur Erlangung des Grades und Titels eines
Doktors der Naturwissenschaften (Dr. rer. nat.)

angenommene Dissertation

von

Nadine Tchamba Yimga

geboren am 07. 09. 1987 in Bangangté, Kamerun

Erstgutachter: Prof. Dr. Jürgen Parisi

Zweitgutachter: Prof. Dr. Elizabeth von Hauff and Prof. Dr. Veit Wagner

Tag der Disputation: 31 Mai 2017

“For I am not ashamed of the gospel of Christ: for it is the power of God unto salvation to everyone that believeth; to the Jew first, and also to the Greek. For therein is the righteousness of God revealed from faith to faith: as it is written, the just shall live by faith.”

Romans 1: 16-17

Abstract

Organic semiconductors offer the possibility to develop light weight, flexible and cost-effective applications for energy production and optoelectronic industry. However, the difficulty in controlling crystal growth and thin film morphology remain the main hindrances in achieving good electrical transport, which is essential for efficient device performance. In the family of organic semiconductors, liquid crystal (LC) semiconductors offer a unique flexibility in controlling thin film morphology because of their unique self-assembly, and self-healing properties. This thesis investigated charge transport in several novel LC small molecule dyes. The dyes were provided by Merck Chemicals and demonstrated different LC mesophases. Few LC dyes have been investigated to date, and the goal of this thesis was to establish fundamental relationships between chemical structure and opto-electronic response.

As first step, the influence of molecular packing on the optical and electrical properties of the LC dye 4,7-bis[5-(2-fluoro-4-pentyl-phenyl)-2-thienyl]-2,1,3-benzothiadiazole (FPPTB) was investigated. Solution processed FPPTB films were subject to thermal annealing through its phase transition temperatures and characterized with x-ray diffraction (XRD) and polarized optical microscopy. The results demonstrated that cooling FPPTB films from the nematic and isotropic phases increased crystal domain size, but also induced local structural variations in the molecular packing of crystalline FPPTB. High carrier mobilities in the order of $10^{-3} \text{ cm}^2 \text{ V}^{-1} \text{ s}^{-1}$ were achieved in diode structures. The relationship between thermal stability and high carrier mobility values was discussed in terms of the interplay between long range molecular order and increased $\pi - \pi$ interactions between molecular pairs in the FPPTB film.

The influence of variations in the position of the fluorine substitution on molecular packing and ambipolar electrical transport of LC dyes : 4,7-bis[5-[4-(3-ethylheptyl)-2,3-difluorophenyl]-2-thienyl]-2,1,3-Benzothiadiazole (2,3-FFPTB) and 4,7-bis[5-[4-(3-ethylheptyl)-2,6-difluorophenyl]-2-thienyl]-2,1,3-Benzothiadiazole (2,6-FFPTB) was then investigated. Interestingly we observe that the molecule with no mesophases demonstrates higher carrier mobility. These results highlight the complex relationship between short range molecular interactions and long range order in molecular films.

In the second part of this work, the outcome results obtained with LC dyes were compared with those of novel conducting polymers, two regioregular polythiazoles (rr-PTzs) bearing trialkylsilyloxymethyl-side-chains (PTzTHX, PTzTNB) that were synthesized by cooperation

partners at the University of Ulm. The result demonstrated that LC dyes were better hole transporting materials, and could also achieve comparable electron mobilities with the PTzs polymers when the polymers molecular weights were lowered.

Finally, I examine measurement techniques to determine mobility values in more detail. It is commonly observed in the literature, that the charge carrier mobilities measured on the same material using different measurements could show variations in order of magnitude. The reason of discrepancies observed for the results obtained in this thesis using impedance spectroscopy and space charge limited current were thoroughly discussed and the limiting factors for a more accurate measurement identified. This indicated the importance of judicious choice of contact electrodes and the knowledge of the injection barrier prior electrical characterizations in the case of new materials. The overall results highlighted the promising potentials of small molecules LC dyes for future optoelectronic applications and call for further research interest in this class of materials.

Zusammenfassung

Organische Halbleiter eröffnen Möglichkeiten für Leichtbau-, flexible und kostengünstige Anwendungen in der Energieproduktion und optoelektronischen Industrie. Allerdings bleiben die schwierige Kontrolle über das Kristallwachstum und die Morphologie abgedeckter Schichten Hindernisse, um guten elektrischen Ladungstransport zu erhalten, was für die Leistungsfähigkeit entsprechender Bauteile von Bedeutung ist. In der Familie der organischen Halbleiter eröffnen Flüssigkristalle einzigartige Möglichkeiten zur Kontrolle der Schichtmorphologie, denn sie haben einzigartige Eigenschaften bezüglich der Selbstanordnung und Ausheilung von strukturellen Defekten. Diese Doktorarbeit untersucht den Ladungstransport in einigen neuen, molekularen Flüssigkristall-Farbstoffen. Die Farbstoffe wurden von der Firma Merck Chemicals zur Verfügung gestellt und wiesen verschiedene Mesophasen auf. Bisher wurden nur wenige Flüssigkristall-Farbstoffe untersucht, und das Ziel der Doktorarbeit war die Etablierung von Struktur-Eigenschafts-Beziehungen zwischen der chemischen Struktur und dem optoelektronischen Verhalten.

Im ersten Schritt wurden die molekulare Packung sowie die optischen und elektrischen Eigenschaften des Flüssigkristall-Farbstoffs 4,7-bis[5-(2-fluoro-4-pentyl-phenyl)-2-thienyl]-2,1,3-benzothiadiazole (FPPTB) untersucht. Lösungsmittelprozessierte FPPTB-Filme wurden einem thermischen Heizschritt über die Phasenübergangstemperaturen hinaus unterworfen und mittels Röntgenbeugung sowie optischer Mikroskopie mit polarisiertem Licht charakterisiert. Die Ergebnisse zeigen, dass die Abkühlung der FPPTB-Filme aus der nematischen und isotropen Phase die Größe kristalliner Domänen vergrößert, aber gleichzeitig lokale strukturelle Variationen in der molekularen Packung der kristallinen Filme verursacht. Hohe Ladungsträgermobilitäten der Größenordnung $10^{-3} \text{ cm}^2 \text{ V}^{-1} \text{ s}^{-1}$ wurden in Diodenstrukturen erreicht. Der Zusammenhang zwischen der thermischen Stabilität und hohen Ladungsträgermobilität wird vor dem Hintergrund des Zusammenspiels zwischen molekularer Fernordnung und ansteigenden $\pi - \pi$ Wechselwirkungen im Film diskutiert.

Der Einfluss von Variationen der Position der Fluor-Substitution auf die molekulare Ordnung und den ambipolaren Ladungstransport wurde anhand zweier Flüssigkristall-Farbstoffe untersucht:

4,7-bis[5-[4-(3-ethylheptyl)-2,3-difluoro-phenyl]-2-thienyl]-2,1,3-Benzothiadiazole (2,3-FFPTB) und 4,7-bis[5-[4-(3-ethylheptyl)-2,6-difluoro-phenyl]-2-thienyl]-2,1,3-Benzothiadiazole (2,6-FFPTB). Interessanterweise war zu beobachten, dass das Molekül ohne Mesophase eine höhere Ladungsträgermobilität aufweist. Diese Ergebnisse

unterstreichen die komplexen Beziehungen zwischen molekularer Nahordnung und Fernordnung im Film.

Im zweiten Abschnitt der Doktorarbeit werden die Ergebnisse zu den Flüssigkristallen mit Ergebnissen zu neuen leitfähigen Polymeren verglichen. Konkret ging es um zwei regioregulare Polythiazole mit Trialkylsiloxymethyl-Seitengruppen, die von Kooperationspartnern an der Universität Ulm synthetisiert wurden. Die Ergebnisse zeigten, dass die Flüssigkristall-Farbstoffe weitaus bessere Lochtransportmaterialien sind und auch zu den Polymeren vergleichbare Elektronen-Mobilitäten erzielen konnten, wenn die Molekulargewichte der Polymere herabgesetzt wurden.

Weiter habe ich Messmethoden zur Bestimmung der Ladungsträgermobilität untersucht. In der Literatur ist festzustellen, dass Werte, die für das gleiche Material mit unterschiedlichen Methoden erhalten wurden, um Größenordnungen abweichen können. In dieser Doktorarbeit wurden Impedanzspektroskopie und raumladungsbegrenzte Dioden zur Messung der Mobilitäten verwendet, und die Unterschiede detailliert diskutiert. Dies zeigte auch die Bedeutung der Auswahl geeigneter Elektrodenmaterialien und Kenntnisse über Injektionsbarrieren bezüglich der elektrischen Charakterisierung der Materialien auf. Insgesamt unterstreichen die Ergebnisse das vielversprechende Anwendungspotential molekularer Flüssigkristall-Farbstoffe für zukünftige optoelektronische Bauteile und verstärken das Forschungsinteresse an dieser Materialklasse.

Table of Contents

Abstract	I
Zusammenfassung	III
1. Introduction	1
2. Fundamentals of Organic Semiconductors and Liquid Crystal Semiconductors	5
2.1. Organic Semiconductors.....	5
2.1.1. Carbon based materials	5
2.1.2. Charge transport in organic semiconductors	8
2.2. Liquid Crystal semiconductors	10
2.2.1. Introduction to liquid crystals	10
2.2.2. Structure of liquid crystals	12
2.2.3. Charge transport in liquid crystals.....	16
2.3. Basics on experimental techniques used for the study of charge transport in this thesis	21
2.3.1. Impedance spectroscopy	21
2.3.2. Space charge limited current	28
2.4. Liquid crystals for opto-electronics	29
3. Materials and Methods	31
3.1. Materials	31
3.2. Methods	34
3.2.1. Thin film fabrication	34
3.2.2. Device preparation	35
3.2.3. Characterization	37
4. Results and Discussions	41
4.1. Exploiting the high thermal stability of liquid crystal dyes (FPPTB) to achieve high carrier mobility in organic semiconductors	42

4.1.1.	Structure and properties of FPPTB	42
4.1.2.	Molecular packing in FPPTB films.....	46
4.1.3.	Optical properties	50
4.1.4.	Electrical properties.....	52
4.2.	The influence of fluorine substitution on molecular packing and carrier mobility in liquid crystal dyes 2, 6-FPPTB and 2, 3-FFPTB	59
4.2.1.	Molecular properties of 2, 3-FFPTB & 2, 6-FFPTB.....	59
4.2.2.	Optical properties on films	63
4.2.3.	Molecular packing on films.....	65
4.2.4.	Electrical properties: Investigation of Ambipolarity in 2,3-FFPTB and 2,6-FFPTB dyes	77
4.3.	Comparison of the charge carrier transport in novels liquid crystal dyes 2,3-FPPTB and 2,6-FFPTB with a study case of novel n-type conducting polymers.....	85
4.3.1.	Molecular structure of the polymers	85
4.3.2.	Electrical characterization of PTzTHX and PTzTNB.....	86
4.3.3.	Comparison of electron and hole mobilities in PTZs and LCs dyes.....	90
4.4.	Comparison of hole mobilities in Liquid crystal dyes measured with impedance spectroscopy and space charge limited current	93
4.4.1.	Results	93
4.4.2.	Discussion	98
5.	Conclusions.....	104
	Bibliography	107
	Publications and Conference contributions.....	119
	Acknowledgements.....	121
	Curriculum Vitae	124
	Erklärung.....	126

1. Introduction

Organic semiconductors are known over decades now, to be a very promising technology for energy production, as well as for the photonic and optoelectronic industry. They demonstrate great potential in novel electronic applications due to the endless possibilities for creating new materials which can be processed in large scale at low cost. We owe this success in part to their numerous advantages such as chemical flexibility, very good optical properties, and low material usage via solution processing. This makes of this light weight and cost-effective technology a long term alternative for fossil energy in the future. Nevertheless, organic semiconductors show in general more disordered transport, in comparison to their inorganic counterparts^[1-2], which is related to much lower carrier mobilities and carrier life times. The charge carrier lifetime which corresponds to the approximate time scale taken for a minority charge (electron or hole) to recombine with an opposite charge carrier, highly depends among other factors, upon the concentration of charge carriers, hence also upon charge carrier mobility inside the organic semiconductor^[3-4].

Charge carrier mobility remains a key parameter for achieving high device performance in organic electronics. And beside this obvious performances requirement, stability at elevated temperatures, and against corrosive gases like oxygen for examples, are crucial for most commercial applications. The major bottle neck for developing high performance organic electronics is then the compromise between increasing charge carrier mobility while maintaining both good processability (ideally in non-toxic solvents) and good thermal stability of the organic films under operating conditions. But in general, interfaces of organic films, are often chemically and structurally heterogeneous, and their controlled preparation is often non trivial^[5]. This results generally in poor structural integrity and poor thermal stability in films for most of the common solution processed polymers and small molecules^[5-8]. Hence, for electronics applications where large area coverage and structural flexibility are required, this makes it even more challenging to achieve both optimized transport and structure inside devices. To overcome the challenge of structural integrity in order to achieve high mobility, substantial efforts have been directed into molecular design of large pi-conjugated molecules for instance^[9-11], which will facilitate the transport of charge carriers. Unfortunately, there is currently limited knowledge with regard to the design of molecular

alignment in crystal lattices so as to achieve the desired level of mobility ^[8]. The other challenge of poor thermal durability of the films remains also difficult to overcome, because of the low melting points which are often lower than 100°C for polymers and small molecules. This limits the thermal processes that are used for wiring and passivation during device fabrication. ^[8].

Therefore, materials which offer much better control over their thin film structure are of high interest, to achieve that goal of high performance organic electronics. Known to have unique structural characteristics which can be controlled via electric fields or temperature, liquid crystals (LC) semiconductors appear then as a great alternative. This class of materials, which are mostly known for their displays applications, has become part of our daily life today and we find them in our clocks, telephones and calculators, car dashboards, digital cameras, computer displays, flat-panel television display etc. And beyond displays, LCs applications are already found in sensing or laser technology for instance, while new and exciting developments are foreseen for the future ^[12]. However coming to the family of organic electronic materials, LCs are relatively newcomers, and have attracted a growing interest in academia as well as electronic industry the last decades. The first electronically conducting liquid crystals was only reported in 1988 by Washizuka et al. of Sharp Corporation who demonstrated an active-matrix full-color full-motion 14-in display using a thin-film-transistor array ^[13]. Since that time, research in the direction of using LC in organic electronics has made a substantial progress.

Nevertheless, because the field of LC organic semiconductors is still relatively young, there are still issues which need to be tackled, to make their applications in organic electronics a success as it is already the case in displays. In particular, the theory of electronic conduction in liquid crystals is much less well developed than that of electronic conduction in other organic materials ^[14-17]. Also, the structure-property relationship in this class of materials, for instance the relation between molecular structure and conductivity is still not fully understood. As a contribution to tackle these issues, this work at hand aims to add insights, in the understanding of structure-property relationships in LC semiconductors, for improvement of transport properties in organic semiconductors.

Compared to amorphous and polymeric semiconductors, liquid crystals semiconductors also demonstrate easy processing and good chemical flexibility, and they exhibit generally very

high chemical purity and higher carrier mobility in their mesophases ^[14]. Though their mobilities still behind those seen in crystalline organics, what really sets them apart, is the unique flexibility in controlling crystal growth and morphology. This is certainly to be attributed to their self-organizing coupled with their self-aligning and self-healing properties, responsible for most of their commercial usefulness ^[14]. These self-assembly properties of liquid crystalline (LC) semiconductors can be exploited to produce stable, highly ordered molecular films from solution ^[18-19].

According to the pattern of aggregation of molecules and their molecular structures, different types of liquid crystal phases are classified amongst them the discotic and calamitic phases ^[14-15]. To date, tremendous progress has been made in developing LC molecules for field effect transistor applications ^[8, 20-27]. However, though discotic LCs and conducting polymer LCs ^[11] have been investigated in opto-electronic applications ^[28, 29-30], few studies have focused on small molecule LC dyes ^[31].

In this thesis the charge transport properties in newly synthesized soluble liquid crystalline dyes are investigated. These materials are synthesized by Merck Chemicals, Darmstadt, and handled for this work in the scope of a cooperation. All the materials investigated are calamitic LCs, all crystalline at room temperature, and exhibiting liquid crystal mesophase, namely a nematic or smectic phase at higher temperatures, depending on each material molecular structure. To tackle the issue of the limitation of mobility in organic semiconductors arose above, the LC properties of the new materials namely, their self-assembly, high thermal stability and high chemical purity, are exploited to improve transport properties. It is crucial for improving the efficiency of electronic devices to control the morphology of the thin films in order to improve charge carrier transport, and hence increase device performance. Concretely, a systematic control of their opto-electronic properties was carried by controlled cooling from nematic or smectic back to crystalline phase of the materials. The objective being to combine thermal durability and reproducibility of these materials to increase overall device performance. The goal of the thesis is to prepare high mobility crystalline thin films with good thermal stability using LC dyes.

The thesis starts with an overview of organic semiconductors and liquid crystalline semiconductors, with a main focus laid on their charge transport properties, followed by a concise description of the materials investigated. Thereafter, detailed description of device

fabrication and measurement techniques used for characterization are described. Then comes the main part of the work, which discusses main results obtained. Firstly, considering the high thermal stability of the first LC dye studied, the high carrier mobility achieved is discussed in terms of the interplay between short range crystal order and long range intermolecular interactions inside this material. Then follows investigations on two novel LC dyes exhibiting very similar chemical structures, but with a great difference in their melting behavior, leading to different mesophase. The influence of variations in the position of the fluorine substitution on transport properties of these molecules, are studied using X-ray-diffraction (XRD), Raman spectroscopy and electrical characterization. Particularly, an emphasis was set on the influence of the smectic phase on electron transport inside these materials. An efficient ambipolar transport based on efficient hole-conducting (p-type) and electron-conducting (n-type) materials, is highly desirable for electronic and optoelectronic applications such as organic integrated circuits, ambipolar transistors, organic light emitting diodes (OLED) for instance. It appeared then necessary in this work, to investigate the ambipolarity of these two novel materials. The outcomes of the new LC dyes particularly in terms of their hole and electron-transport properties are compared shortly with a studied case of new semiconducting polymers.

Charge carrier mobility was mainly investigated in this thesis, using impedance spectroscopy (IS) as a non-destructive technique, to study fully processed single carrier devices. Space charge limited current (SCLC) was also used as a second method. To close this result section, the mobilities obtained using these two different techniques are compared. The discrepancies observed are discussed and the limiting factors for an accurate measurement of charge carrier mobility in organic films are identified. The thesis ends up with a highlight on major findings, and main conclusions.

2. Fundamentals of Organic Semiconductors and Liquid Crystal Semiconductors

This chapter offers a basic introduction to organic semiconductors in general, with an emphasis laid on their transport properties. Special attention is paid to liquid crystals semiconductors, and a basic introduction to their structural, as well as their electrical transport properties will be discussed.

2.1. Organic Semiconductors

2.1.1. Carbon based materials

Organic semiconductors are a class of materials made up mostly by carbon and hydrogen atoms. They combine the electronic advantages of semiconducting materials with the chemical and mechanical advantages of organic compounds such as plastics^[32].

The investigations of organic solids date back to the early 20th century, where first studies on conductivity, photoconductivity, the photoelectric effect, and fluorescence of these materials were reported^[2]. However, the revolution in the field came with the first successful doping of conducting polymers in the 1970ies signifying a breakthrough in electronics. The discovery and advances in doping conducting polymers was awarded with Nobel Prize in Chemistry in the year 2000^[33-35]. An important step was also reached in the 1980ies, when the first organic light emitting diode (OLED) and the first photovoltaic (PV) cell both based on small molecules were reported^[36-37]. Since then, the field of organic semiconductors has emerged to a major division in solid state physics, and has found its application essentially in organic light emitting diodes (OLED) used for display and lighting applications, organic field-effect transistors (OFET), and organic photovoltaics (OPV).

Organic semiconductors are essentially carbon based materials, classified in two major classes which are: the low molecular weight materials such as small molecules or oligomers, and large molecular weight materials such as polymers^[33]. The key feature of these organic semiconductor materials is a backbone consisting of alternated single and double bonds, resulting in a π -conjugated network which confers them their semiconducting properties^[38]. A single carbon atom has four valence electrons in its outer shell; the electronic configuration corresponds in the ground state to $1s^2 2s^2 2p^2 (1s^{\uparrow\downarrow} 2s^{\uparrow\downarrow} 2p_x^{\uparrow} 2p_y^{\uparrow} 2p_z)$. In conjugated systems,

the s and p orbitals hybridize to form three sp^2 orbitals (resulting from the hybridization of 2s with $2p_x$ and $2p_y$). In this configuration, the three hybridized sp^2 orbitals form three equivalent single σ -bonds, coplanar to the carbon atom and positioned 120° apart from each other. The 4th un-hybridized orbital ($2p_z$) is perpendicular to the plane of the sp^2 hybridization, and form an additional π -bond with the p_z orbital of the neighboring carbon atom. The p_z -orbitals can then be extended over all carbon atoms, leading to the formation of a delocalized band, the π -orbitals, responsible of the conductive nature of the material [39]. In comparison to the σ -bonds constituting the backbone of the molecules, π -bonds are significantly weaker, due to the lower overlap of the p_z -orbitals [33]. An illustration of these orbitals is given in Figure 2.1-a), which depicts one of the simplest conjugated π -electron systems.

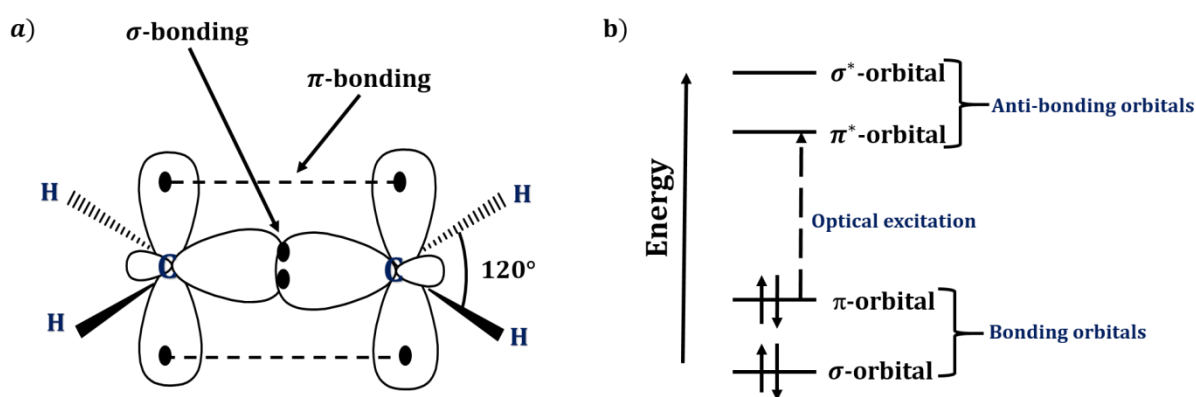


Figure 2.1: a) σ and π bonds in ethane, as an example for one of the simplest conjugated π -electron systems; b) The energy levels of a π -conjugated molecule. The lowest electronic excitation is between the bonding π -orbital and the antibonding π^* -orbital [Adapted after [33]].

The overlap resulting from the strong σ -bonds may interfere constructively or destructively to yield a bonding and antibonding molecular σ and σ^* orbital. Similarly, the overlap resulting from the remaining weaker π -bonds yields a bonding and antibonding molecular π and π^* orbital. Therefore, the σ orbitals are located deeper in energy than the π orbital, and the lowest electronic excitations of conjugated molecules are the π - π^* transitions as depicted in the Figure 2.1-b). In the ground state of the molecule, all bonding orbitals are filled with two electrons of antiparallel spin while the antibonding orbitals are empty. Thus, the highest occupied molecular π -orbital, is identified as the HOMO and the lowest unoccupied molecular π^* -orbital represents the LUMO. The HOMO and LUMO form the frontier orbitals

of the organic semiconductor, and are separated by an energy gap which can be seen in analogy to their inorganic counterpart, as the valence band and conduction band, respectively [32-33]. This energy gap, usually called the optical band gap, is typically between 1.5 and 3 eV for organic semiconductors, leading to light absorption or emission in the visible spectral range [33]. The energy gap is determinant in the understanding of physical characteristics such as electronic and optical properties of organic semiconductors. Its value depends on the structure of the material and decreases for an increasing number of repeat units comprising the molecule [39].

In general, any excitation process such as light absorption for example, which promotes an electron in an antibonding orbital and a missing electron (hole) in a bonding orbital, leads to the formation of a neutral excitation, i.e. an exciton, which is localized on the molecule. Due to the low relative dielectric constant in organic semiconductors (on the order of $\epsilon \approx 3$), coulomb attraction between electron and hole is strong, resulting in an exciton binding energy ranging from of 0.5 eV to more than 1 eV [32]. The nature of bonding in organic semiconductors is fundamentally different from their inorganic counterparts. Inorganic semiconductors are covalently bounded amongst each other, while bounds between molecules are van-der-Waals-bonded. This implies a considerably weaker intermolecular bonding as compared to covalently bonded inorganic semiconductors. As consequence, delocalization of electronic wavefunctions amongst neighboring molecules is much weaker, which has direct implications for their optical properties and charge carrier transport [33].

A major advantage of organic semiconductors is that a large variety of semiconducting materials (small molecules and polymers) can be designed and synthesized according to application requirements. Amongst the two classes of materials, a main difference lies in their method of processing. Small molecules are primarily vacuum deposited by sublimation or evaporation to form highly ordered films. But since several years now, the viability of solution-processed small molecules in devices has been largely demonstrated [40-43]. On the other hand, conjugated polymers are not thermally stable enough for sublimation, and can only be processed from solution, by spin-coating or printing techniques [33]. While polymer chemistry is very flexible, small molecules offer the advantage of high chemical purity and flexible processing strategies. Solution processing offers interesting potential for low cost processing and large scale production. However, solution processed semiconductor films are

associated with higher structural and energetic disorder, resulting in decreased carrier mobility and increased carrier trapping and recombination. A major research focus in the field of organic electronics is to improve the electrical properties of organic thin films to achieve better device performance.

2.1.2. Charge transport in organic semiconductors

Due to a rather large band gap that causes their intrinsic charge carrier concentration to be very low, organic semiconductors are inherently insulators. However, for charge transport to take place there must be a charge on the molecular unit which might be an electron removed from a bonding orbital, or an additional electron accommodated to the anti-bonding orbital^[32]. This implies that conductivity in this class of material can only be extrinsic and results generally from the injection or extraction of an electron at the electrodes, from doping through reduction or oxidation of the molecule by a dopant molecule, and from the exothermic dissociation of an exciton in a molecule by electron transfer to an adjacent molecule^[2, 32].

The weaker intermolecular interactions which characterize the organic semiconductor hinder the movement of charges, causing the energy site within the material to be strongly localized. Charge transport in such a disordered system is therefore described by hopping transport of charges between localized energy sites. A basic concept to analyze the charge carrier mobility in this case, is the Gaussian disorder model (GDM)^[44, 45] that describes hopping within various sites.

The density of state (DOS)^[44] fits perfectly as a model to describe charge transport in disordered organic materials, which usually exhibit a Gaussian shape for their absorption band. The Gaussian density of state is given in this case by:

$$g(E) = \frac{N}{\sqrt{2\pi}\sigma} \exp\left(-\frac{E^2}{2\sigma^2}\right) \quad (1)$$

where N is the number of energy sites per unit volume. The energy E is measured relative to the center of the DOS, with the distribution width σ . In such model, a charge carrier moves by uncorrelated hops in a broad density of states and thermal activation is required to overcome the energy differences between different sites^[32].

Miller-Abraham's formalism ^[32, 46] is used in general to describe hopping mechanism in organic materials, and defines the hopping rate by the following equation:

$$v_{ij} = v_0 \cdot \exp\left(-2 \cdot \gamma \cdot a \cdot \frac{r_{ij}}{a}\right) \times \exp\left(-\frac{\varepsilon_j - \varepsilon_i}{K_B T}\right) \quad ; \varepsilon_j > \varepsilon_i \quad (2a)$$

$$v_{ij} = v_0 \cdot \exp\left(-2 \cdot \gamma \cdot a \cdot \frac{r_{ij}}{a}\right) \times 1 \quad ; \varepsilon_j \leq \varepsilon_i \quad (2b)$$

where v_{ij} is the hopping rate between the occupied site i and the unoccupied site j ; r_{ij}/a the relative distance between the localized site i and j ; γ is the inverse localization radius of the electronic wave function; a is the lattice constant; K_B the Boltzmann constant and v_0 a frequency factor.

The GDM model used to describe transport here is largely based on Monte Carlo simulation ^[44], which can be visualized as an ideal experiment with absolute control over any relevant parameter necessary to reproduce charge transport properties of real samples accurately ^[47]. In such experiment, independent charge carriers are generated at arbitrary energy sites and one follows their random motion under the action of an applied electric field. Charges placed at higher energy tend to relax energetically towards quasi-equilibrium while the hopping rate and the velocity of charges decrease during the relaxation ^[32]. V. I. Arkhipov et al ^[48] showed that carrier mobility at equilibrium is a factorized function of temperature and concentration of localized states.

The hopping mechanism of transport could be simplified by the concept of transport energy E_t first introduced by Don Monroe ^[49], which reduces the hopping transport to trap-controlled band transport. This concept is based on the notion that an energetically upward jump of a carrier into a hopping site belonging to the transport level is followed by its several downward jumps, which effectively reduce hopping to trap-controlled transport. The transport energy E_t is the minimum energy to which carriers must jump in order to contribute to the dc conductivity ^[50]. The band transport as described in the literature ^[50-52], demonstrated that hopping transport processes revolve around the energy transport E_t within the system. Practically all carriers, localized in a deep tail of the DOS distribution, will eventually jump

upwards to one of the shallower states whose energies are close to E_t . And charge carriers in the shallow energy sites, will hop downwards to lower energy sites that are close by.

The probability that a carrier will hop to some site of a specific energy, depends generally on the temperature, the density-of-state distribution, the localization radius, and the energy of the starting site ^[50].

Typically, organic semiconductors are unipolar materials, i.e. they preferentially transport one type of charge (electron or hole). And in case ambipolar transport is observed, the mobility for one type of charge carrier (electron or hole), is largely dominant over the other ^[53]. Hole transporting materials are denoted as p-type while the electron transporting materials are denoted as n-type. The key parameter that quantifies charge transport is the mobility, and the performance of organic semiconductors in device application critically depends on its value. Many factors influence transport in organic semiconductor such as molecular packing in film, electronic and structural disorder, presence of impurities and temperature ^[1]. Regarding molecular packing, for example, favorable local molecular interactions that promote a high degree of electronic coupling are necessary for obtaining high carrier mobility values. Additionally long range molecular order in the bulk structure of the film is also important ^[1]. Generally, the deposition of organic material from solution onto a substrate leads to the formation of large nucleation sites separated by grain boundaries. While the individual crystalline grains are well ordered, the grains are usually randomly aligned throughout the film. Grain boundaries are known to significantly affect the charge transport in organic materials and it has been demonstrated that mobility increases with grain size, i.e. the reduction of grain boundary density ^[54-56]. One bottleneck for obtaining solution processed organic films with high carrier mobilities are the formation of grain boundaries. Therefore, the control of crystal growth and morphology in organic thin films remains a challenge for further developments in organic electronics.

2.2. Liquid Crystal semiconductors

2.2.1. Introduction to liquid crystals

In 1888 an Austrian botanist, Friedrich Reinitzer observed a ‘strange’ material (cholesteryl benzoate) that exhibited a mesophase between solid state and liquid state ^[57]. He later

collaborated with the German scientist Otto Lehmann, who studied the material and discovered that the liquid at the mesophase exhibited a double refraction effect, characteristic of a crystal. He named then the material “fliessende krystalle” and this is how the term “liquid crystal” was born ^[58]. However after this discovery, the scientific community did not show great interest in liquid crystal (LC) research, until the middle of the 20th century. The developments started when a dynamic scattering mode (DSM) was discovered in 1964 after Heilmeyer and other scientists of Radio Cooperation of America (RCA) laboratories observed an interesting effect in certain classes of nematic liquid crystals. This gave birth to the first liquid crystal display (LCD) ^[59] and in May 1968, RCA members held a conference to announce the discovery of a totally new type of electronic display ^[60]. In 1973, the world's first liquid crystal product, a pocket calculator was developed by Tomio Wada working at Sharp ^[61]. Despite this success story, researches in LC materials remain confined until the early 80ies, to their potential for display applications. The major milestone was reached in 1988, when the first electronically conducting liquid crystal was reported by Washizuka et al. of Sharp Corporation ^[13]. This introduced liquid crystals in the field of organic electronic materials, and since then, substantial literature on ‘liquid crystal semiconductors’ has developed.

In general, liquid crystals are designated as a state of matter intermediate between that of a crystalline solid and an isotropic liquid. This is because, they possess many of the mechanical properties of a liquid, such as high fluidity, inability to support shear formation, and coalescence of droplets, while at the same time they are similar to crystals in that they exhibit anisotropy in their optical, electrical, and magnetic properties ^[62]. The liquid crystal phases are called *mesomorphic phases*, where mesomorphic means of *intermediate form*. In term of phase diagram they have some degree of molecular alignment between the long-range, three-dimensional order of a crystalline solid and the total disorder of the (isotropic) liquid ^[14]. Hence as far as both temperature and composition are concerned, liquid crystal phases lie between solids and liquids. However, it is important to mention that the great interest in liquid crystals lies in the fact that they possess unique and distinct properties, which are not always classified between those of solids and those of liquids.

Liquid crystals (LCs) combine molecular order and mobility from nanoscale to macroscale or in other words from molecular level to macroscopic levels. This unique combination enables

such systems to respond to different external stimuli such as temperature, magnetic field, electric field, mechanical stress, light, chemical reaction, and electrochemical reaction by finding a new configuration of minimum energy ^[63]. As example, a field of about $100 \text{ mV}\mu\text{m}^{-1}$ will reorient the molecules in a typical liquid crystal display (LCD) cell, while fields of 4 or 5 orders of magnitude larger are usually unable to align the molecules in either crystalline solids or (isotropic) liquids ^[14]. Similarly, the response of liquid crystals to slight changes of temperature is often noticeable while it is insignificant in solids and liquids. In practice, when a mesomorphic material in the crystal state is subjected to heating, the energy supplied disrupts the crystalline lattice leading to the LC phase. As the temperature rises, the LC will absorb further energy becoming an isotropic liquid.

An illustration is given on Figure 2.2 where order and viscosity, as well as response to electric fields of liquid crystals are compared to those of the solids and liquids. A sketch of their response to temperature is also given.

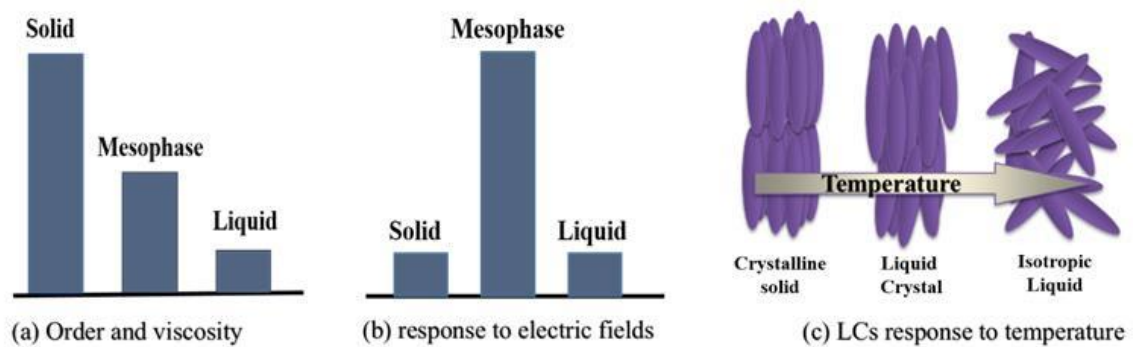


Figure 2.2: Liquid crystal properties compared to those of solids and liquids in **a)** order and viscosity **b)** response to electric fields (Adapted after Ref. [14]); **c)** LCs response to temperature. **N.B:** In **a)** and **b)**, the y-scale reflects the order of magnitude of the parameters indicated on the x-scale, and it is arbitrary.

2.2.2. Structure of liquid crystals

Dozens of thermodynamically stable liquid crystalline phases are possible, depending on molecular structure and intermolecular interactions, each sufficiently distinct in structure and properties to the others ^[14]. Amongst the most common ones, we have nematic, smectic, columnar and cholesteric phase.

Nematic Phase

This phase is the simplest and least-ordered phase of liquid crystals and is characterized by molecules with directional but without a positional order. The liquid crystals are oriented in a common direction along the director, \mathbf{n} (see an illustration Figure 2.3-a)). The magnitude of \mathbf{n} is taken to be unity. The locally preferred direction may vary throughout the medium, although in the unstrained (i.e. at equilibrium, under no strain or pressure) nematic phase it does not ^[64].

The most fundamental property of a liquid crystal is its anisotropy ^[62]. Hence the physical properties of the system strongly depend on the average alignment of the director \mathbf{n} . Nematic phase has low viscosity in general and the molecules are as free to flow as those in the isotropic liquid ^[14]. Among the LC dyes studied in this thesis, **FPPTB** exhibits the nematic phase

Smectic Phase

In the smectic phase, molecules demonstrate both directional and positional order, forming layers or planes. Motion is restricted to within these planes, but planes may slide with respect to one another ^[62]. There are over a dozen variants of smectic phases, indicated by letters of the alphabet from A to K (excepted D), with a variety of combinations of short-range and long-range ordering. But the most common ones are the smectic A (smA) and smectic C (smC). In the smectic A, the molecules are aligned perpendicular to the layers, with no long-range crystalline order within a layer (see Figure 2.3-b)). The layers can slide freely over one another. In the smectic C phase, the preferred axis is not perpendicular to the layers, so that this phase has biaxial symmetry (see Figure 2.3-c)) ^[14, 62]. The LC dye **2,3-FFPTB** studied in this work exhibits two smectic phases.

Columnar Phase

The columnar phase is a class of liquid-crystalline phases in which molecules assemble into cylindrical structures to act as mesogens (see Figure 2.3-d)). This mesophase is characterized by stacked columns of molecules (ordered or disordered), with the columns packed together to form a two-dimensional crystalline array. Columnar liquid crystals are grouped by their structural order and the ways of packing of the columns. Disk-shaped mesogens can orient themselves in a layer-like fashion known as the discotic nematic phase. If the disks pack into stacks, the phase is called discotic columnar ^[14, 64].

Cholesteric Phase

The cholesteric phase also called chiral nematic phase, is similar to the nematic phase in having long-range orientational order, with the centers of mass of molecules possessing no long-range positional order. It differs from the nematic phase in that the director varies in direction in a regular way, throughout the medium ^[62]. Typically, the molecules in the cholesteric phase are aligned at a slight angle to one another. The alignment is favored by intermolecular forces resulting from the chiral center contained in the nematic mesogenic molecules constituting the mesophase. This gives rise to the formation of a stack of very thin 2D nematic-like layers structure, with the director in each layer twisted with respect to those above and below (see Figure 2.3-e) ^[65].

Materials may display one or more of these liquid crystal phases. The phases occur in general in the following order with decreasing temperature: isotropic liquid, nematic, smectic A, smectic C, crystal. Figure 2.3 shows a simplified picture of the relative arrangement of molecules in the liquid crystal phases described above. Some liquid crystals often show no mesophase between the crystalline solid and the isotropic liquid phase. In this case, the LC subjected to increasing temperature, will gradually loses its long range positional order to become an isotropic liquid after reaching the melting point. The LC dye **2,6-FFPTB** investigated in this thesis is an example.

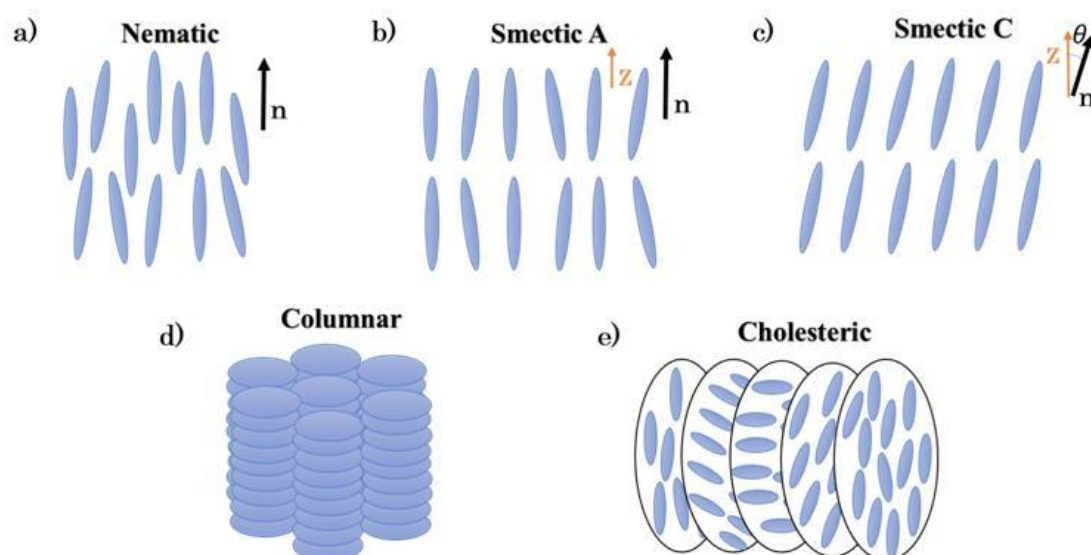


Figure 2.3: The arrangement of molecules in liquid crystal phases. **a)** The **nematic phase**. The molecules tend to point on average in a particular direction (director \mathbf{n}), but with no positional order. **b)** the **smectic A phase (SmA)** where the director \mathbf{n} points in the same direction as the layer normal, \mathbf{z} ; and **c)** the **smectic C phase (SmC)** where the director, \mathbf{n} , points at some angle θ to the layer normal, \mathbf{z} ; **d)** **columnar phase**. The disk-shaped mesogens pack themselves into stacked columns **e)** the **cholesteric phase**. The molecules tend to have the same alignment which varies regularly through the medium and the molecules show no positional order. [Adapted after <http://cnx.org/content/m46154/1.2/>]

The LC phases could be classified into two different categories namely calamitic and discotic phases. When the pattern of aggregation of molecules is rod-like, these are said to be **calamitic**. Calamitics may form highly fluid liquid crystal phases, which are still able to maintain an extended pattern of alignment with the molecular long-axes all lying parallel. Inversely **discotic** molecules, are flattened and disc-like, and may form liquid crystal phases where the planes of the molecules tend to lie parallel, but where the molecules are free to slide over one another. It is possible for large amounts of thermal motion to be accommodated without destroying the structure of the phase in both type of aggregation. Especially, rotational motion about the long axes of calamitics and about the short axes of discotics can occur without destroying the overall pattern of molecular alignment. Calamitic molecules usually aggregate into layers giving the smectic phases while the discotic molecules have tendency to form stacks resulting in columnar phases^[14]. All the LC dyes investigated in this thesis are calamitic.

There are in principle two distinct ways of converting a solid crystalline material into a liquid crystalline phase: by heating or by adding a solvent. Thermotropic mesophases are created by heating and lyotropic mesophases are formed by adding solvent, which usually is water. This restricts lyotropic mesophase to temperature range over which water is liquid. The major distinction between these two systems concerns the patterns of aggregation of the molecules. Conventionally, lyotropic molecules aggregate into micelles as a result of both hydrophobic and hydrophilic regions they possess. Those micelles allow the hydrophobic parts of molecules to reduce their contact with the water subphase ^[14].

2.2.3. Charge transport in liquid crystals

To ensure efficient charge transport in organic materials, charges must be able to move from molecule to molecule without being trapped or scattered ^[1]. This means that thin films free of grain boundaries and structural defects are highly desirable to reduce recombination and trapping in organic electronic materials. However, controlling crystal growth morphology of solution processed organic semiconductors in order to obtain thin films free of grain boundaries, remains extremely difficult. In that sense, liquid crystals offer a unique opportunity for morphology control of thin films, making it possible to achieve films free of grain boundaries and reduced densities of structural defects. Combined with the self-assembly and self-aligning properties, the fluidic nature of liquid crystals enables self-healing to reduce defects in films. This offers the possibility to increase the charge carrier mobility via morphology control by simply heating and cooling of the film and exploiting the self-aligning properties of the liquid crystal mesophases.

Investigations on electrical transport in liquid crystals date back to late 60ies, when the electrical conductivity in various LCs was first measured ^[66-68]. These early research efforts established conduction in LC to be ionic, and it was thought to be so until late 70ies. However, after the discovery of discotic liquid crystals in 1977 ^[69], quest of electronic conduction in LC drew considerable attention leading in the 90ies to the establishment of electronic conduction in both discotic and calamitic phases of LCs ^[70-75]. A report of Jun-ichi Hannah et al. in 2009 ^[17], clearly demonstrated that the intrinsic conduction is electronic in the nematic phase of highly purified samples. Since that time, it is understood that the intrinsic conduction mechanism of liquid crystals, irrespective of the mesophase, is electronic.

Their study helped to understand that ionic conduction also often observed in liquid crystals, is extrinsic and due to chemical impurities; which impurities can be ionized by a charge trapped and/or auto ionization under illumination ^[14-15].

In the context of organic semiconductor materials, the LCs electronic conduction i.e. conduction of electrons and holes, is intermediate to those of amorphous solids and molecular crystals as illustrated by diagram in Figure 2.4. LC mesophases generally demonstrate carrier mobilities ranging from $10^{-3} \text{cm}^2 \text{V}^{-1} \text{s}^{-1}$ to $10^{-1} \text{cm}^2 \text{V}^{-1} \text{s}^{-1}$. Nevertheless, field effect mobility values over $0.1 \text{cm}^2/\text{Vs}$ and even exceeding $10 \text{cm}^2/\text{Vs}$ have been demonstrated in recent years in highly ordered smectic phases. These values are very comparable to carrier mobilities measured in molecular crystals ^[8, 76].

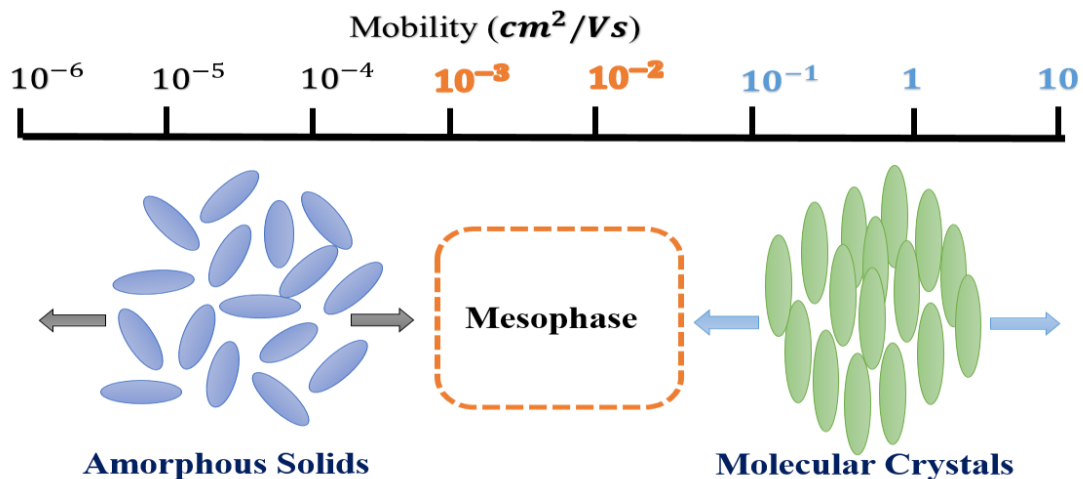


Figure 2.4: Diagram of mobility in organic semiconductors materials: Comparison of LC with amorphous solids and molecular crystal [adapted after Ref 15].

- Ionic and Electronic conduction in liquid crystals

Conduction in LC was considered to be ionic for a long time, before the electronic conduction has been proved. This is due to the fluidic nature of LC which implies two possible conduction mechanisms: ionic and electronic. The ionic conduction is characterized by ionized molecules drifting in an applied electric field and is favoured in less viscous medium. This is because the ionized molecules experience friction from the medium during drift. Inversely, electronic conduction characterized by the migration of electrons from molecule to molecule, is favoured in a viscous medium because the ionic conduction is suppressed ^[14]. Though electronic conduction is generally higher than ionic conduction because no mass

transport is required, these two conduction mechanisms are not always easy to distinguish from mobility measurements. For example, a mobility value over $10^{-3} \text{cm}^2 \text{V}^{-1} \text{s}^{-1}$ is clearly attributed to electronic conduction, while a value lower than $10^{-4} \text{cm}^2 \text{V}^{-1} \text{s}^{-1}$ could be accounted for ionic or electronic conduction. However, temperature dependence and dilution effects are convenient ways mostly used to differentiate among these two conduction mechanisms^[14]. It has been demonstrated that ionic conduction strongly depends on temperature, while electronic conduction in different mesophases hardly depends on temperature. It is also proved that, dilution can enhance mobility for ionic conduction in a mesophase diluted with a diluent having a low viscosity, whereas it inversely reduces electronic conduction^[77-78]. Nevertheless the electronic conduction only, is intrinsic to LCs. The ionic conduction is extrinsic in nature, because induced in general by chemical impurities. For this reason the focus in the next section, is set on electronic conduction in mesophase for the description of charge carrier transport in liquid crystals.

- Charge transport in liquid crystalline semiconductors

A typical liquid crystalline conjugated molecule has a rigid aromatic π -conjugated core with long flexible hydrocarbon chains attached, which give the molecule an enhanced shape anisotropy, namely a calamitic or discotic shape^[14]. This self-organized π -conjugated aromatic core moiety in the liquid crystal phases is very effective as an electronic carrier conduction path, i.e. a path for electrons and holes, resulting in good charge transport properties^[79].

In a highly ordered mesophase, the shortest inter-molecular distance of 3.5 Å, is not short enough to guarantee a band-like transport of electrons and holes, because of weak intermolecular interactions. This suggests that the conduction in LC mesophases is governed by a hopping mechanism, as in other organic semiconductors, through localized states rather than the band conduction through extended states^[14]. In hopping model where good overlap between the orbitals is required, the chemical composition and local molecular ordering of the liquid crystal director strongly influence charge hopping rates, while the presence of defects and overall morphology define the global charge carrier pathway^[80].

The mechanism of carrier transport in the mesophase is determined by a balance between the viscosity and the intermolecular transfer integral^[16]. The transfer integral from a molecule A

(donating orbital) to a molecule B (receiving orbital), usually denoted as J can be defined as [81].

$$J = \langle \Phi_A | H | \Phi_B \rangle \quad (3)$$

where H represents the Hamiltonian for the system, Φ represents the multi-electron wavefunction of the molecule and the labels A and B denote whether the charge is localized on molecule A or B . J represents the overlap of electronic orbitals between neighboring molecules and it is determined by intermolecular distance and orientation as well as variations in molecular conformation [76]. To increase the intermolecular transfer integral, the π -conjugated system should be extended as large as possible while the insulating alkyl chains should be as short as possible [82]. In smectic phase for instance, the large degree of intermolecular orbital overlap within layers leads to increased intermolecular transfer integrals, enhancing electronic transfer. This is not the case in nematic phases in general, where fast intermolecular charge transfer is limited [16].

LC phases are characterized by both dynamic molecular motion and molecular order. While charge transfer in the mesophase is hardly affected by the rotational motion, the molecular order highly affects the hopping rate. Hence, the mobility increases when the molecular order is increased both in columnar and smectic mesophases. Another feature that affects the carrier transport properties of LC is the anisotropic molecular shape. Indeed, the anisotropy in mobility attains a few orders of magnitude or even more in a typical liquid crystal. This large anisotropy in mobility results in one-dimensional carrier transport along the columns in discotic columnar phases and two dimensional carrier transport within the layers in smectic phases [14]. This makes it consequent in terms of device applications, to control the molecular orientation in liquid crystalline films for devices.

Investigations of charge transport in disc-like (discotic) LCs, confirmed that they form ordered one dimensional columns with excellent $\pi - \pi$ stacking [82-85]. However carrier transport is limited by structural defects in the one-dimensional columnar structures. Rod-like (calamitic) LCs, on the other hand, generally form two dimensional ordered layered films [18]. But also, a three-dimensional conduction similar to that in amorphous solids is observed in the nematic liquid crystals, where oriented liquid crystalline molecules sit randomly without positional order [86]. Carrier transport is more robust against structural defects in calamitic LC

films than in discotic LC films ^[15]; however, overlap between the π orbitals of neighboring molecules is also more limited ^[82]. Carrier mobility can be optimized in calamitic LC films by slowly cooling the film through progressively ordered smectic phases to optimize $\pi - \pi$ stacking and reduce structural defects in the film ^[20-22].

One of the unique features of carrier transport in LC materials is the ambipolar transport. Namely, they most often transport both holes and electrons, a phenomenon which is rarely observed in amorphous and crystalline organic semiconductors. Ambipolar transport has been observed in numerous mesophases of highly purified materials ^[87-88]. Another distinct feature of charge carrier transport in mesophase is the temperature and electric field independence of mobility at room temperature and above. However, unlike amorphous materials, LCs are not exempted from structural defects such as dislocations and inhomogeneous boundaries ^[14]. Nevertheless, in the case of smectic mesophase for instance, it has been shown that these structural defects hardly affect the carrier transport properties ^[89-91]. H Maeda et al ^[89-90] investigated the effect of defects in the bulk and at the domain boundary on carrier transport in smectic mesophases of 2-phenylnaphthalene derivatives. They observed non-dispersive carrier transports for all the cells and found that neither cell thickness nor domain sizes affected the carrier transport. It was concluded that the bulk contains few deep defects and that the domain boundary is electrically inactive in these mesophases ^[89]. They also investigated the charge transport properties in the same class materials with a focus on the electrical nature of the boundaries at the phase transition from liquid crystalline phase into the crystal phase. It was found that at the initial stage, the defective nature of the crystalline boundaries takes the shape of shallow traps, successively followed by that of deep traps. They also observed that the polydomain allowance for the carrier transport in mesophases disappears completely when the phase transition takes place into the crystalline phases ^[90]. Hong Zhang and Jun-ichi Hanna ^[91] studied photoconductive properties in a smectic liquid crystalline photoconductor of 2-(48-octylphenyl)-6-dodecyoxynaphthalene (8-PNP-O12) using the time-of-flight measurement. Their findings demonstrated that the $\mu\tau$ (μ : mobility and τ : charge carrier lifetime) products depended on neither a domain size in the polydomain texture nor an electric field. The results of these studies support the argument that local carrier transport at defect sites is made possible by the flexibility of the molecular orientation in mesophases, or the soft structure of mesophases. This outstanding feature of carrier transport

in LC materials set them apart from crystalline materials and provides a great benefit for large scale device applications^[14].

2.3. Basics on experimental techniques used for the study of charge transport in this thesis

2.3.1. Impedance spectroscopy

The extraction of charge carrier mobility in this work was mainly investigated using impedance spectroscopy. Impedance spectroscopy has received an increased attention these last decades, in the study of charge transport in organic materials. This frequency resolved non-destructive technique offers the advantage of a time-dependent measurement, and allows at the same time, a quantitative analysis of dielectric and electric properties of components under investigations.

According to Ohm's law, the resistance R in an ideal resistor is defined as the ratio of the voltage $V(t)$ to the current $I(t)$. However dielectric and semi-conducting materials exhibit a complex response to time-varying electric fields. In this context, the simple concept of resistance is replaced by the more general concept of impedance Z , which is the complex resistance.

Impedance $Z(\omega, t)$ is a frequency-dependent, complex parameter composed of a real component and an imaginary component:

$$Z(\omega, t) = \frac{V(\omega, t)}{I(\omega, t)} = Re(Z(\omega, t)) + i.Im(Z(\omega, t)) \quad (4)$$

where $V(\omega, t)$ and $I(\omega, t)$ are the voltage and the current respectively, both dependent on frequency ω and time t ; $Re(Z)$ represents the real part of the impedance and $Im(Z)$ its imaginary part both measured in ohm $[\Omega]$. i is the complex number^[92]. A representation of the impedance in the complex plane is shown in Figure 2.5.

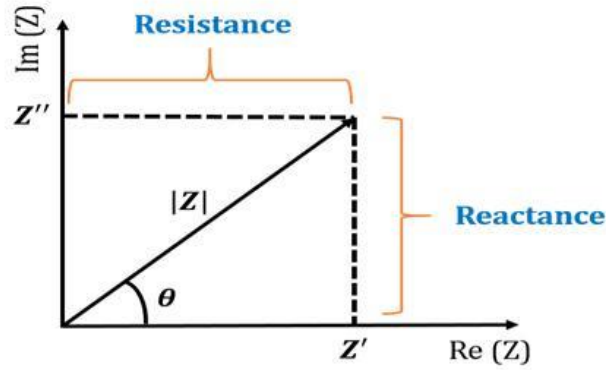


Figure 2.5: The impedance Z as a complex magnitude plotted as a planar vector using rectangular and polar coordinates.

$Re(Z)$ is usually denoted as Z' , and refers to the resistance (i.e. the resistance to current flow) of the sample under investigation, while $Im(Z)$ denoted as Z'' refers to the reactance (i.e. resistance of sample to polarization). Information about the electrical properties of the full electrode-material system are derived from the resulting structure of the $Z(\omega, t)$ vs ω response analysis ^[92].

In practice, impedance spectroscopy consists of applying a small AC voltage with amplitude V_{AC} on a sample, which can be superimposed by an offset DC voltage component V_{DC} , according to the equation:

$$V(\omega, t) = V_{DC} + V_{AC} \cdot \sin(\omega t) \quad (5)$$

The AC current response measured in return corresponds to a DC offset current I_{DC} and an AC current I_{AC} , shifted by a phase angle φ with respect to $V(\omega, t)$:

$$I(\omega, t) = I_{DC} + I_{AC} \cdot \sin(\omega t + \varphi) \quad (6)$$

Figure 2.6 illustrates this principle, where an AC voltage is applied to a probing point of the J-V curve of a diode, and the AC current is measured in return.

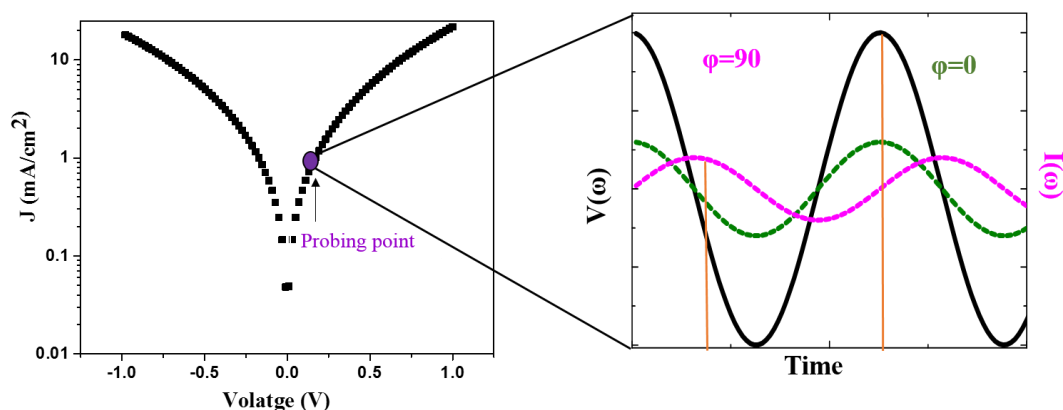


Figure 2.6: Schematic of an impedance spectroscopy measurement: A small AC voltage $V(\omega)$ applied at a certain probing point of the I -V curve, results in an AC current $I(\omega)$. The ratio $V(\omega) / I(\omega)$ gives the complex resistance $Z(\omega)$ (impedance).

Several parameters such as conductivity, dielectric permittivity, mobilities of charges in the bulk material, and capacitance of the electrode-semiconductor interface can be derived from a single impedance measurement. Several other functions related to impedance Z can be derived such as: the complex conductivity (admittance), the modulus function M and the complex dielectric constant or dielectric permittivity ϵ [92]. The formulas of these different parameters are given in Table 2.1 below.

Table 2.1: Impedance-Related Functions. Where G is the conductance and B the susceptance; ω is the angular frequency and C is the capacitance.

Impedance related parameters	Formula
Complex admittance Y	$Y = Z^{-1} = G + i.B$
Modulus function M	$M = j\omega CZ$
Complex dielectric constant ϵ	$\epsilon = M^{-1} = Y/j\omega C$

Impedance measurement analysis

The frequency-dependent impedance spectra of an organic material are plotted in the complex plane, which resulted plots are known as Nyquist plots [92]. An example of impedance outputs from a single measurement is sketched in Figure 2.7-a). To quantitatively describe the impedance data, an equivalent circuit model is necessary. In this model, the impedance can be

well approximated by that of an equivalent circuit made up of an ideal resistor and a capacitor for the case of an organic layer as depicted in Figure 2.7-b), where this equivalent circuit is given together with its corresponding representation in the complex plane (Cole-Cole plot). In such a circuit, a resistance represents a conductive path, and a given resistor in the circuit might account for the bulk conductivity of the material ^[92].

An important parameter of the circuit is the time constant τ which corresponds to the relaxation time of charge in the system. This relaxation time of the capacitor (oscillator) is defined as the time needed by the charge carriers to travel in the oscillating circuit. It is given as the product of the resistance and the capacitance: $\tau = R.C = 1/\omega_0$. Where ω_0 refers to the resonance frequency.

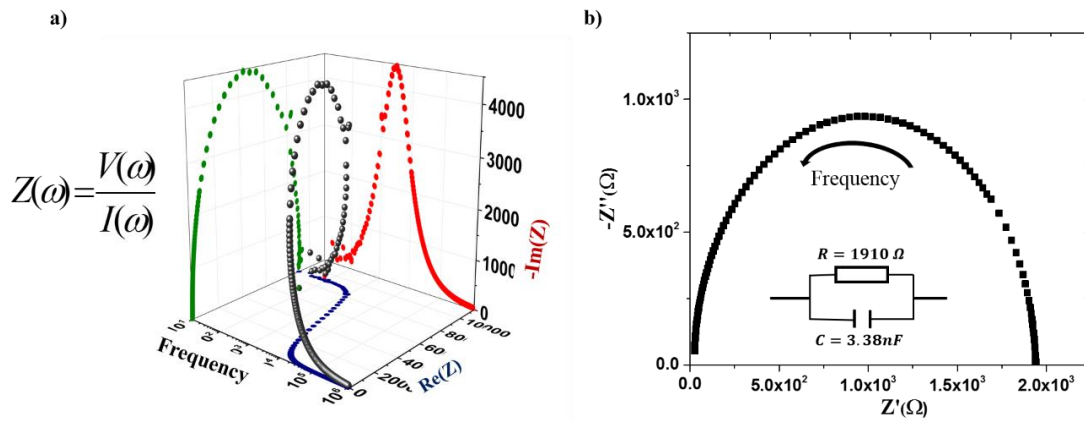


Figure 2.7: a) Bode and Nyquist plots resulted from impedance measurement b) Typical representation of a Cole-Cole plot in the complex plane. The inset shows the equivalent circuit R-C with $R = 1910 \Omega$ and $C = 3.38 \text{ nF}$.

The impedance of a single capacitor is given by:

$$Z_C = \frac{1}{i\omega C} \quad (7)$$

For an equivalent circuit with the R-C in parallel as shown in Figure 2.7-b), the admittances of two elements are added to give the equivalent impedance as follow:

$$Y = Z^{-1} = \frac{1}{R} + i\omega C \quad (8)$$

The impedance of an RC element is then derived from the above equation as:

$$Z = \frac{R}{1+i\omega RC} = \frac{R}{1+i\omega\tau} \quad (10)$$

From Equation 10, the frequency response of the R-C element, results in a semi-circle in the complex plane as shown in Figure 2.7-b). From this semi-circle, one can estimate the parameters R and C and hence deduce the quantitative estimates of conductivity, relaxation times and interfacial capacitance for instance. At low frequencies, the capacitor does not respond to the small AC stimulus applied, and the electrical properties of the circuit are determined only by the resistance. Hence, the semicircle crosses the real axis at the resistance R ($R = 1910 \Omega$ for the example on the figure). As the frequencies increase, the imaginary part of the impedance ($Im(Z)$) which accounts for the capacitor, increase until the oscillating circuit reaches the resonance; the capacitive behavior is dominating at higher frequencies. For very high frequencies, the oscillating circuit stops responding to the AC excitation and the $Im(Z)$ approaches the origin. The semicircle is characteristic of a single time constant, i.e. of a single R-C element in parallel. In general for real devices built up of multiples layers and interfaces, more than one R-C element have to be considered for the equivalent circuit model, in order to describe accurately the behavior of the sample.

In the complex plane data plots such as the one in Figure 2.7-b), the frequency is an implicit variable. This absence of explicit frequency dependence information is a considerable drawback, for this means that the time constant cannot be extracted from the plot directly. Nevertheless the Nyquist plot can be analyzed to see if there is a single relaxation time, or a distribution of relaxation times. If the data is properly fitted with an RC element, the relaxation time can then be extracted. To this end, it is useful to apply the plot of impedance with respect to frequency. Practically, the impedance is plotted with log frequency on the x-axis while both the absolute value of the impedance and phase-shift are plotted on the y-axis. The resulting plots such as $-Im(Z)$ vs f and $Re(Z)$ vs f as shown in Figure 2.7-a) are generally termed Bode plots^[92].

Extraction of charge carrier mobility using Bode Plots of impedance

The extraction of charge carrier mobility in organic materials using impedance spectroscopy has been considered in the literature since several years. Studying PPV-based hole-only devices with impedance spectroscopy, Martens et al^[93] demonstrated that the transit of injected carriers leads to an inductive contribution to the device admittance. Specifically, they

demonstrated that the finite transit time τ of holes in the devices is reflected in the admittance. Their study also demonstrated that the specific frequency dependence of the response reflects the wide distribution in transit times of the injected carriers due to dispersive transport. In another study, Marten et al ^[94] determined simultaneously the electron and hole mobility in polymer light emitting diodes (PLEDs) using admittance spectroscopy. They demonstrated that charge transport at time-scale τ is reflected in the frequency domain around $\omega \approx \tau^{-1}$. Later, S. W. Tsang et al ^[95] demonstrated that the imaginary part of the complex admittance (susceptance) is related to the carrier transport properties of the materials. They found that the plot of the negative differential susceptance $-\Delta B$ ($-\Delta B = -\omega(C-C_{\text{geo}})$) against frequency f ($\omega/2\pi$) can be used to determine the average transit time τ_{DC} of carriers inside an organic film. C and C_{geo} are respectively, the frequency dependent and geometric capacitances of the organic film. Assuming no dispersion of transport they show that, the position at which the maximum in $-\Delta B$ occurs (*i.e.* at τ^{-1}), is related to the average transit time τ_{DC} by the relation:

$$\tau_{DC} = 0.56. \tau \quad (11)$$

They verified their findings by studying successfully the hole mobility in *m*-MTDATA using admittance spectroscopy.

Tripathi et al ^[96] refined the previous analysis, for the case of small molecule *m*-MTDATA and polymeric MEH-PPV and demonstrated that instead of differential susceptance, the frequency dependence of imaginary part of impedance ($-\text{Im}(Z)$ vs f) is a simpler and more convenient method of determination of mobility. With their method they demonstrated that in real device condition, the true transient time τ_{DC} in an organic semiconductor is related to the peak frequency by:

$$\tau_{DC} = \kappa. \frac{1}{f_0} \quad (12)$$

Where κ is a numerical factor that relates the time constant τ from the frequency-dependent data to the DC transit time of charge carrier τ_{DC} , and f_0 is the frequency peak extracted from $-\text{Im}(Z)$ vs f plot.

This indicates that, as the voltage across the sample varies, the average transit time and hence the peak frequency shifts enabling determination of mobility as a function of electric field. The validity of this method was verified for a wide variety of materials for the case of a simple equivalent circuit in the transit time regime. Also, the robustness of the technique was proved even in the case of dispersive transport ^[96].

Though the value of κ is not clearly defined from the literature ^[94-96], Tsang et al demonstrated that for organic materials with low dispersion, $\kappa = 0.56\tau$ and $\kappa = (0.56 \pm 0.1) \cdot \tau$ for materials with higher dispersion ^[95]. The mobility is related to the transient time by the relation ^[95-96]:

$$\mu = \frac{d^2}{\tau_{DC}V_{DC}} = \frac{d^2}{\kappa \cdot V_{DC}} \cdot f_0 \quad (13)$$

where d is the layer thickness, V_{DC} the applied bias field and τ_{DC} the transit time as already defined.

For the measurements in this thesis, we usually applied frequencies between 1 MHz to 10 Hz, and 1 KHz to 10Hz, with a small AC voltage of 10-20 mV. V_{DC} values range was usually taken from 0.1 to 0.5V.

Assumptions made for impedance spectroscopy

In general prior to impedance measurements, several requirements must be considered. Practically for accurate IS measurement, the strict condition of an Ohmic contact at one of the electrode/organic interfaces i.e., at either the anode or cathode, must be met. A judicious choice of metal electrodes for the device under investigation is then necessary. The charge carrier mobility is also assumed to be independent of the electric field inside the material ^[97]. Moreover, since the peak frequency used to determine mobility with this technique is related to the transit time of charge carrier, there must be no or very low injection barrier at the organic/metal electrode interface, to ensure efficient extraction of charge carrier mobility. The influence of parameters such as barrier height or contact resistance on the determination of carrier mobility using IS is further discussed in the result section (Chapter 4.4).

2.3.2. Space charge limited current

Charge carrier mobilities in organic materials can also be obtained from the J-V characteristics of a simple diode structure (anode/organic/cathode). In this case one of the most common methods used is the SCLC method. This technique offers the advantage of simpler experimental apparatus for it only requires a commonly available source measurement unit.

In organic semiconductors in general, charge carriers mobilities are typically low. Nevertheless, if by a judicious choice of metal electrodes charges can be efficiently injected into the device, the device limiting factor that remains is the ability of the material to transport the charge through the bulk. In such low mobility materials, if a low voltage is applied, the resulting current is linear following ohms law. At higher voltage, the low mobility of the carriers prevents carrier transport and extraction, leading to charge build up in the semiconductor layer. In these conditions, a space charge effect is observed and the current varies as a function of $V^{3/2}$ according to Child's law ^[98]. The Child's Law behaviour of a space charge limited current that applies in a vacuum diode is generally limited in the case of organic semiconductor and insulating materials. In this case Child's law is replaced by the Mott-Gurney law ^[99] as described below.

The Mott-Gurney theory preconizes that, by choosing metal contacts with appropriate work functions to form Ohmic contacts with the HOMO (hole-only) or LUMO (electron-only) level of the organic semiconductor, the injection of a single carrier type inside the device is then insured. Moreover, with the assumption made of an independent field mobility (i.e. μ , constant) for the organic semiconductor, the current inside a single carrier device follows a SCLC behavior and the current density at higher voltage can be described by the Mott-Gurney law given by ^[99-101]:

$$J = \frac{9}{8} \epsilon_0 \epsilon \mu \frac{V^2}{d^3} \quad (14)$$

Where μ is the mobility, ϵ_0 is the permittivity of free space, ϵ the dielectric constant of the material, V the applied voltage and d the thickness of the film.

At lower voltages, the J-V characteristics follow the microscopic ohm's law given by:

$$J = nq\mu \frac{V}{d} \quad (15)$$

With n the charge carrier concentration, and q the elementary charge. At higher voltages, the SCLC effect appears, and the transition between the two regimes is characterized by a change in a slope of the J-V curve which switches from a slope 1 to a slope 2. By fitting the J-V curve relatively to these two slopes, charge carrier density, and then mobility can be then determined using the two equation (14) and (15).

Assumptions made for space charge limited current

The SCLC as defined with the above equation assumes a trap-free transport. Besides this requirement, the SCLC theory also needs an efficient charge injection to be applicable. This is because, sufficient current must be injected into the organic semiconductor film to maintain a current that is bulk-limited rather than interface-limited ^[102]. For this reason, the work function of the electrode contact must be aligned to HOMO and LUMO levels of the organic semiconductor. There is also a minimum thickness requirement for the SCLC technique ^[97], because the injection efficiency can be more problematic in the case of too thin film ^[102]. Additionally, as result of disorders, defects or contamination for instance, traps can hinder transport in organic semiconductor material. In such condition, the SCLC condition is met, if the ratio of free carriers to trapped carries is independent of voltage ^[102]. Further considerations for the use of SCLC in the determination of charge carrier mobility are discussed in the chapter 4.4 of the result section.

To extract hole and electron mobility for single carrier's devices using the SCLC method in this thesis, the dark J-V currents were fitted by the Mott–Gurney equation.

2.4. Liquid crystals for opto-electronics

In the recent years, numerous studies have been published on liquid crystals for opto-electronic applications ^[8, 11, 21, 23-30, 79, 103-105]. Amongst them, most focus has been laid on LCs with large bandgaps for applications in OFETs ^[8, 23-26] and a tremendous progress has been made generally in developing LCs for field effect transistors applications ^[8, 21-29, 103-104]. As result, very high field effect mobility could be achieved in OFETs benefiting of an optimized thin film structure lately. For example, Hiroaki Iino et al. published recently a highly ordered smectic liquid crystal with field effect mobility in excess of $10 \text{ cm}^2/Vs$ ^[8]. Some works have

also been done in developing discotic LC ^[28] and conducting LC polymers ^[11, 29, 30, 104-105] for optoelectronic applications. These efforts has led to achieve efficiencies in organic solar cells approaching 10% ^[11, 105] using novel conducting LC polymers. Kumar, M et al ^[106] in a recent review gave also an idea of the progress that has been made in the development of LCs for OPV applications. However, when it comes to small molecule LC dyes for opto-electronic applications, not much work has been done up to date and very few have been reported in the literature ^[31]. In the only work found, Soberats, B et al ^[31] reported on a liquid crystal dye exhibiting interesting properties for application in smart windows.

In a review, Mary O'Neill and S.M. Kelly ^[107] discussed some limiting issues LC for optoelectronics applications. The major limiting factor identified was that of a non-optimized LC morphology. It was found for instance that aggregation induces luminescence quenching. This signifies that the self-assembly properties can be negative for opto-electronic applications as the aggregation is not well understood. This point has been specially addressed in the scope of this work, where the self-assembly properties of LC dyes in relation with an optimized thin film morphology and enhanced electronic performance have been thoroughly studied.

The present thesis comes then as a direct contribution in the use of small molecule LC dyes for optoelectronic applications. For this, the strategy employed is to address the shortcomings associated with organic materials such as poor structural integrity or low thermal stability, by using novel small molecules LC dyes to prepare high mobility crystalline thin films with good thermal stability and optimized thin film structure.

3. Materials and Methods

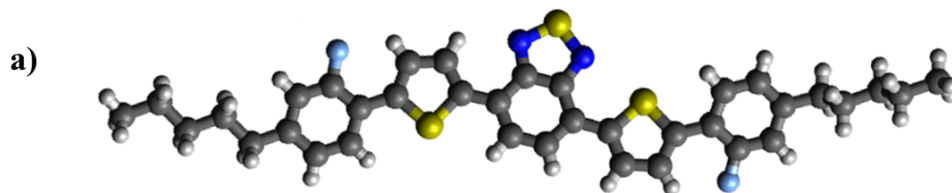
In this chapter I present, the different materials investigated, followed by a detailed description of thin films and devices preparation, as well as the characterizations applied for measurements.

3.1. Materials

Materials investigated in the scope of this work, are liquid crystalline dyes: 4,7-bis[5-(2-fluoro-4-pentyl-phenyl)-2-thienyl]-2,1,3-benzothiadiazole (**FPPTB**), 4,7-bis[5-[4-(3-ethylheptyl)-2,3-difluoro-phenyl]-2-thienyl]-2,1,3-Benzothiadiazole (**2,3-FFPTB**) and 4,7-bis[5-[4-(3-ethylheptyl)-2,6-difluoro-phenyl]-2-thienyl]-2,1,3-Benzothiadiazole (**2,6-FFPTB**) all synthesized by Merck Chemicals, Darmstadt. At the difference of FPPTB which has a shorter soluble group, 2, 3-FFPTB and 2, 6-FFPTB display an additional soluble ethylheptyl group, as well as an additional fluorine molecule on the benzene ring. These materials were all well soluble in most of the common organic solvents, with FPPTB yielding the best reproducibility in anhydrous tetrahydrofuran (THF), and 2, 3-FFPTB & 2, 6-FFPTB in anhydrous chloroform (CHCl_3). Both solvents were purchased from Sigma-Aldrich.

FPPTB dye:

Figure 3.1-a) shows the molecular structure of FPPTB. It crystallizes in a triclinic lattice with the lattice parameters $a = 4.85 \text{ \AA}$, $b = 15.96 \text{ \AA}$, $c = 21.35 \text{ \AA}$ and $\alpha = 69.86^\circ$, $\beta = 85.97^\circ$ and $\gamma = 86.59^\circ$. The differential scanning calorimetry (DSC) predicts the melting point at $M_p = 149^\circ\text{C}$ and an isotropic melt at temperatures above $229,7^\circ\text{C}$ (see Figure 3.1-b)). FPPTB is crystalline at room temperature.



b)

Transition	Temperature (°C)	Enthalpy (cal/mol)
Crystalline → Nematic	149	7000
Nematic → Isotropic	229.7	200

Figure 3.1: a) Chemical structure of FPPTB and b) phase transition temperatures and enthalpies determined by DSC.

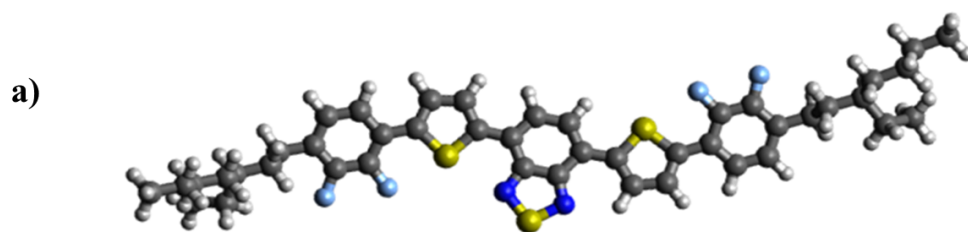
While processing it in films, FPPTB has always been annealed subsequently, relative to its phase transition temperatures, and cooled down before characterization (for steady state measurement) or implementation inside devices. Selected properties of the material, with the different annealing temperatures applied on films during fabrication, are summarized in the Table 3.1.

Table 3.1: Annealing temperatures used for films of **FPPTB** during fabrication.

Consideration of phase transition	Crystalline	Crystalline	Just before transition from crystalline to nematic	Nematic	Isotropic
Annealing Temperature of films (°C)	As spun	100	140	165	250

2, 3-FFPTB dye:

Figure 3.2-a) shows the molecular structure of 2,3-FFPTB. DSC performed on 2,3-FFPTB (Figure 3.2-b)) indicates that, it is crystalline at room temperature and shows a melting point at 116 °C. It exhibits two smectic phases at about 103 °C and 116 °C respectively, and turns to an isotropic melt above 141 °C.



b)

Transition	Temperature (°C)	Enthalpy (cal/mol)
Crystalline → Smectic I	103	6400
Smectic I → Smectic II	116	300
Smectic II → Isotropic	141	340

Figure 3.2: a) Chemical structure of 2,3-FFPTB and b) phase transition temperatures and enthalpies determined by DSC.

2,3-FFPTB undergoes the same film processing as FPPTB, namely the films were annealed up to different temperatures related to its phase transitions, and cooled down before characterization. Table 3.2 summarizes the temperatures used during film preparation.

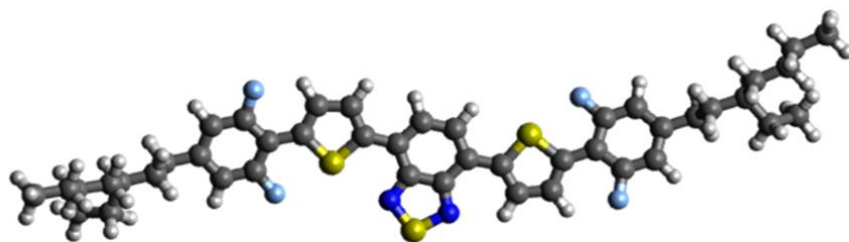
Table 3.2: Annealing temperatures used for films of 2,3-FFPTB during fabrication.

Consideration of phase transition	Crystalline	Just before transition from crystalline to Smectic I	Smectic I	Smectic II	Isotropic
Annealing Temperature of films (°C)	As spun	80	105	120	160

2, 6-FFPTB dye:

2,6-FFPTB has a very similar molecular structure with 2, 3-FFPTB as depicted in Figure 3.3-a), with the only difference lying in the substitution of fluorine molecules on the benzene ring along the chemical backbone. The fluorine molecules are ortho-substituted in 2,3-FFPTB, while they are para-substituted in 2,6-FFPTB, which induces a difference in terms of melting behavior among the two compounds. 2,6-FFPTB shows a melting point at $M_p = 131\text{ }^\circ\text{C}$, and is crystalline at room temperature. This dye also shows no liquid crystal phase (nematic or smectic), but only a crystalline phase which turns into an isotropic melt above $131\text{ }^\circ\text{C}$.

a)



b)

Transition	Temperature (°C)	Enthalpy (cal/mol)
Crystalline → Isotropic	131	7900

Figure 3.3: a) Chemical structure of 2,6-FFPTB and b) phase transition temperatures and enthalpies determined by DSC.

2,6-FFPTB films were cooled down from different temperatures related to its phase transition before characterization. The different annealing temperatures applied on films during fabrication, are summarized in the Table 3.3.

Table 3.3: Annealing temperatures used for **2,6-FFPTB** films during fabrication.

Consideration of phase transition	Crystalline	Just before the transition from crystalline to isotropic	Isotropic
Annealing Temperature of films (°C)	As spun	120	160

3.2. Methods

3.2.1. Thin film fabrication

For results discussed in chapter 4, pristine films of FPPTB, 2, 3-FFPTB & 2, 6-FFPTB, used for optical measurements as well as structural analysis, were prepared from a tetrahydrofuran (THF) solution for FPPTB, and chloroform (CHCl₃) for 2, 3-FFPTB & 2, 6-FFPTB. The solutions were spin-coated onto amorphous glass for X-ray diffraction and optical measurements, and on amorphous glass coated indium tin oxide (ITO) for devices. For this, substrates were cleaned beforehand with detergent and rinsed with deionized water. A

successive cleaning followed, using an ultrasonic bath in acetone, 2-propanol, deionized water and ethanol for 10 min each. The substrates were dried thereafter under nitrogen flow, were treated for 15 min with an ozone pro-cleaner or oxygen plasma. Cleaned substrates were then transferred inside an inert environment, and solutions prepared beforehand and stirred overnight were spin coated at different rate according to the material, on top of the substrates. The resulting layer thickness, measured with a DEKTAK profiler (Veeco DEKTAK 6M, Stylus Profiler equipped with a camera) confirmed a thickness of about 250 ± 5 nm for FFPTB (20mg/ml); 130 ± 5 nm and 230 ± 5 nm for 2, 6-FFPTB; 125 ± 5 nm and 170 ± 5 nm for 2, 3-FFPTB from concentrations of 15mg.ml⁻¹ and 20 mg.ml⁻¹, respectively. The samples were thereafter annealed considering phase transitions for each material, at different temperatures as indicated in Tables 3.1, 3.2, 3.3 and subsequently cooled down to room temperature before characterization. While the characterization concerned was in-situ, the samples were used as spun.

3.2.2. Device preparation

For electrical characterization of FPPTB, hole-only devices were prepared with the following architecture: ITO/PEDOT: PSS/ FPPTB /MoO₃/Ag. For this, patterned ITO substrates were etched beforehand in hydrochloric acid, before cleaning and treatment. After the ozone treatment, PEDOT: PSS (Clevios PVP, AL4083) was spin-coated on top of the substrates, under ambient conditions at 3.500 r.p.m. for 30 seconds using a WS-650M7-23NPPB model spin coater. After this step, samples were transferred inside a glove box filled with nitrogen, and baked at 140 °C for 15 min on an ETL 7420 model hotplate. A solution of FPPTB prepared beforehand and stirred overnight was spin coated at different rates on top of the substrate. For the mobility reported in this thesis, samples were prepared from a 20 mg/mL THF solution and spin-coated at 1000 r.p.m for 60 seconds. Some samples were then annealed at different temperature considering the phase transition of FPPTB (See Table 3.1). For metal contacts, samples were then transferred inside an evaporation chamber, where 8 nm of MoO₃ and 100 nm Ag were deposited under a high vacuum pressure of about 10⁻⁷ mbar. The overlap of the ITO with the metal contacts was measured to be 0.12 cm² for FPPTB single carrier devices.

For electrical measurements of 2,3-FFPTB and 2,6-FFPTB, hole-only and electron-only devices were manufactured, with architectures as follows: ITO/PEDOT:PSS/dye/MoO₃/Ag and ITO/PFN/dye /Ca/Al (dye: 2,6-FFPTB or 2,3-FFPTB). The choice of Poly[9,9-bis(3'-*N,N*-dimethylamino)propyl)-2,7-fluorene)-alt-2,7-(9,9-dioctylfluorene)] (PFN) polymer is justified here by its use in the literature as an efficient electron-injection layer, enabling a significant enhancement in device performance ^[108-109]. ITO substrates were patterned and etched in hydrochloric acid before cleaning. For the hole-only devices, PEDOT: PSS was spun on the substrates at 3.500 r.p.m. for 30 seconds (spin coater model WS-650M7-23NPPB).and baked at 140 °C for 10 minutes in an oven under ambient conditions. Substrates were directly transferred afterwards inside the nitrogen filled glove box. 2,6-FFPTB & 2,3-FFPTB were then spin-coated on top and annealed according to the details given above in Tables 3.2 and 3.3.. For electron-only devices, a PFN interlayer dissolved in methanol (2 mg.ml⁻¹) and acetic acid (2μl.ml⁻¹), was spun at 4000 rpm for 30 second on top of cleaned substrates and samples dried overnight at room temperature. Substrate edges were cleaned in both cases afterward, to ensure a good cathodic contact. 2,6-FFPTB & 2,3-FFPTB were spin-coated on the substrates and some samples were then annealed the same way as for hole-only devices. For metal contacts, MoO₃ (8 nm) and Ag (100 nm) for hole-only diodes, and Ca (20 nm) and Al (100 nm) for electron-only diodes were deposited sequentially inside an evaporation chamber at a pressure of 10⁻⁷ mbar. The overlap of the ITO with the metal contacts measured was 0.1 cm² for 2, 6-FFPTB and 2, 3-FFPTB single carrier devices.

Device preparation and characterization of new polymers discussed in comparative study with LCs dyes.

For electrical characterization of regioregular polythiazoles (rr-PTzs) polymers, electron-only devices & hole-only devices under the following architectures: ITO/PFN/PTzTHX or PTzTNB/Ca/Al and ITO/PEDOT: PSS/PTzTHX or PTzTNB /MoO₃/Ag respectively were fabricated. For this, patterned ITO glasses were successively cleaned by detergent, acetone, 2-propanol, deionized water and ethanol in an ultra-sonic bath for a sequence of 10 min each. The substrates were treated afterward using Ozone procleaner for 15 min. For electron-only and hole-only devices, a same protocol as with LC dyes device was used for PFN and PEDOT: PSS interlayers respectively. For both device architectures, a solution of rr-PTzs, prepared with 5 mg ml⁻¹ in chloroform for PTzTHX and 5 mg ml⁻¹+10% ODCB as additive

for PTzTNB was spun onto the substrates at 1200 rpm for 60 s. Some PTzTHX samples were annealed under an inert environment at 185 °C for 10 minutes and subsequently cooled, and some PTzTNB samples were annealed at 150 °C for 30 minutes before subsequent cooling. The active layer thicknesses were determined to be about 95 ± 5 nm for PTzTHX and 85 ± 5 nm for PTzTNB, measured with a DEKTAK profilometer. The samples were then transferred inside an evaporation chamber where top contacts were deposited under a vacuum pressure of 10^{-7} mbar. 20 nm Ca and 100 nm Al constituted the top contact for electron-only devices, while 8 nm MoO₃ and 100 nm Ag were deposited for hole-only devices.

3.2.3. Characterization

Polarized Optical Microscopy (POM)

Liquid crystal materials are known to interact strongly with the polarized light. Their refractive index depends on the polarization and propagation direction of light and this is responsible of their birefringent property ^[110]. Polarization optical microscopy (POM), is a high sensitive, contrast-enhancing technique widely used in analyzing birefringent materials, and yields generally high quality images. In case of liquid crystal materials, this technique allows the observation of phase transitions of the mesophase. This is usually performed under in-situ conditions, with the analyzed specimen gradually heated up, on a host stage linked to the polarized microscope while the change in the mesophase texture is observed.

To observe the phase transition temperature of FPPTB, in-situ measurement was done, using a Zeiss Axio 100 POM microscope equipped with Linkam stage controlled by a Linkam TMS 94 temperature and cooling stage. Measurement was done under an inert environment for the sample, mounted inside a sealed holder connected to a nitrogen flow and heated at the rate of $10\text{ }^{\circ}\text{C}/\text{min}$ and cooled down at a rate of $20\text{ }^{\circ}\text{C}/\text{min}$. For steady state measurement of FPPTB, 2,6-FPPTB & 2,3-FPPTB thin films, an Olympus U-CMAD3 microscope was used for analysis of the microstructure of thin films. In both cases, the microscopes were equipped with polarizers, positioned in the light path at the bottom of the sample, and analyzers (a second polarizer), placed in the optical pathway between the objective rear aperture and the observation tubes. To practically observe birefringence, the direct transmitted light going through the sample, was blocked with a polarizer oriented at 90 degrees to illumination. Birefringence gives indication of large ordered domains in the thin films. With both

microscopes, images with maximum resolution of $10\ \mu\text{m}$ could be digitalized, and for the results discussed in this thesis, the selected resolution is $60\ \mu\text{m}$.

X-ray diffraction (XRD)

X-ray diffraction (XRD) is one of the fundamental experimental techniques used to analyze atomic structure of new materials. Typically, X-Ray diffraction occurs when a beam of monochromatic X-rays of wavelength λ , collide with crystalline atoms, resulting in a strong scattering which occurs in specific directions only. In the case of this study, X-rays are emitted by bombarding metal targets with high velocity electrons accelerated by strong electric field in the range of 40.0 kV and 40.0 mA, using a Cu $K\alpha$ source. While POM is used as a qualitative tool for analysis of LCs, XRD offers a more quantitative analysis giving information about the crystal structure of materials such as lattice parameters, or crystalline orientation and molecular packing on film.

In-situ measurements were performed by means of a solid anode X-ray tube from a X'Pert Pro PANalytical X-rays diffractometer, equipped with a high temperature chamber linked to a temperature controller unit TCU 1000N Anton Paar, as well as multiple stages (Eulerian Cradle, Sample spinner) for measurement at standard conditions. The steady state samples were annealed up to different phase transition temperatures, and subsequently cooled before XRD pattern being recorded in a $(2\theta, \omega)$ scan configuration using an Eulerian cradle stage. For in-situ measurements, the sample as spun, was placed in a hot stage, and mounted in a high temperature chamber, monitored with a temperature controller. Under an argon flow, the sample was gradually heated up or cooled down at the rate of $30\ ^\circ\text{C}/\text{min}$ while the XRD pattern was recorded also in a $(2\theta, \omega)$ scan at specific temperatures. For the data analysis discussed in this thesis, the software High Score plus, combined with Data Viewer from PANalytical was first used for background subtraction, and the extraction of crystal lattice parameters such as the peak positions, the relative intensity of the reflections and the full width at half maximum (FWHM). The XRD patterns as displayed in the results section was plotted and treated using Origin 2016.

Optical Spectroscopy (Absorption and Photoluminescence)

UV–visible spectra in solution and on films were recorded at room temperature using a Cary 500 UV–visible spectrometer connected to a computer unit. Photoluminescence (PL) in

solution as well as on film was measured with a Fluorolog Horiba, Jobin Yvon linked to a computer unit and equipped with excitation and emission spectrometers, as well as an infrared compound, an iRH 320 spectrometer. Samples were usually excited at the respective wavelengths of 375 nm, 450 nm, and 530 nm. For more accuracy and minimization of scattering effects, the same measurements both for absorption and PL were repeated using analogous setups, equipped with an integrating sphere.

Impedance

For this work, impedance measurements were performed using a Metrohm-Autolab electrochemical setup (PGSTAT302N) equipped with a FRA32M module. This was used in the frequency range from 1 MHz down to 10 Hz for FPPTB and PTzs samples and from 1 KHz down to 10Hz for 2,6-FFPTB and 2,3-FFPTB samples, with an AC voltage amplitude $V_{AC} = 20$ mV or smaller used to probe the device. The offset DC voltage applied V_{DC} , was usually in the range of 0 to 0.5 V in the step of 0.1 V. To avoid or to cancel any background noise, sample's holder built as a Faraday cage for low frequencies, is connected with the instrument's ground plug.

Data extraction for electrical analysis and equivalent circuit modelling were recorded and extracted using the software package NOVA-1.10.3.

Raman Spectroscopy

Raman measurements (transient and Steady-state) for this work, were recorded by Dr. Simon Boehme at the VU Amsterdam. I used Origin 2016 for plotting and analysis of data discussed in this thesis.

Current - Voltage (I-V) measurement

I-V measurements for the single carrier devices in dark were performed under a nitrogen environment inside a glove box using a Keithley 2400 source meter, connected to a computer interface and controlled by a LabVIEW program. Usually for this, a voltage range from -1 V to 1 V or -3 V to 3 V was applied to the diode and the resulting current was measured.

Simulations

All the calculations on the LC dyes used in comparison with the experimental results in this work were provided by Merck. These calculations include the HOMO/LUMO orbitals for all LC dyes, the transfer integrals for holes ($J+$) and electrons ($J-$) for the molecular pairs in the FPPTB crystal and simulated XRD pattern of FFPTB; the electrostatic potential maps of 2,3-FPPTB & 2,6-FPPTB as well as the simulated Raman spectra of 2,3-FPPTB and 2,6-FPPTB.

4. Results and Discussions

-Most of the results discussed in the first chapter of this result section, entitled “Exploiting the high thermal stability of liquid crystals dyes (FPPTB) to achieve high carrier mobility in organic semiconductors”, have been published already in the following article:

Tchamba Yimga, N., Ramanan, C., Borchert, H., Parisi, J., Untenecker, H., Kirsch, P., & von Hauff, E. Interplay between long range crystal order and short range molecular interactions tunes carrier mobility in liquid crystal dyes. *ACS Appl. Mater. Interfaces* **2017**, 9(7), 6228.

-Part of the results discussed in the third chapter of this result section, entitled “Comparison of the charge carrier transport in novels liquid crystal (LC) dyes 2,3-FPPTB and 2,6-FFPTB with a study case of novel n-type conducting polymers”, have been published already in the following article:

Jäger, J., **Tchamba Yimga, N.**, Urdanpilleta, M., von Hauff, E., & Pammer, F. Toward n-type analogues to poly (3-alkylthiophene) s: influence of side-chain variation on bulk-morphology and electron transport characteristics of head-to-tail regioregular poly (4-alkylthiazole) s. *J. Mater. Chem. C* **2016**, 4(13), 2587-2597.

4.1. Exploiting the high thermal stability of liquid crystal dyes (FPPTB) to achieve high carrier mobility in organic semiconductors

In this chapter LC properties such as self-assembly, and high thermal stability of a newly synthesized LC dye, FPPTB, are exploited to achieve high carrier mobility inside devices and access the potential of this material for organic electronics. Concretely, the influence of molecular packing on the optical and electrical properties of the liquid crystalline dye 4,7-bis[5-(2-fluoro-4-pentyl-phenyl)-2-thienyl]-2,1,3-benzothiadiazole (FPPTB) is investigated.

4.1.1. Structure and properties of FPPTB

Figure 4.1-a) shows the molecular structure of FPPTB. The calculated highest occupied molecular orbital (HOMO) and lowest unoccupied molecular orbital (LUMO) are -5.35 eV and -2.85 eV, respectively, yielding an optical band gap of FPPTB 2.50 eV (496 nm). From the geometry of the HOMO and LUMO orbitals, it is observed that the hole wavefunction is delocalized over the conjugated backbone while the electron wavefunction is localized on the benzothiadiazole acceptor unit.

From X-ray diffraction (XRD) patterns taken from single crystals of FPPTB, the unit cell was determined to be triclinic with the lattice parameters $a = 4.85 \text{ \AA}$, $b = 15.96 \text{ \AA}$, $c = 21.35 \text{ \AA}$ and $\alpha = 69.86^\circ$, $\beta = 85.97^\circ$ and $\gamma = 86.59^\circ$. The crystal structure in the (100) direction is shown in Figure 4.1-b) and the relative positions of the four nearest neighbours in the FPPTB crystal are shown in Figure 4.1-c).

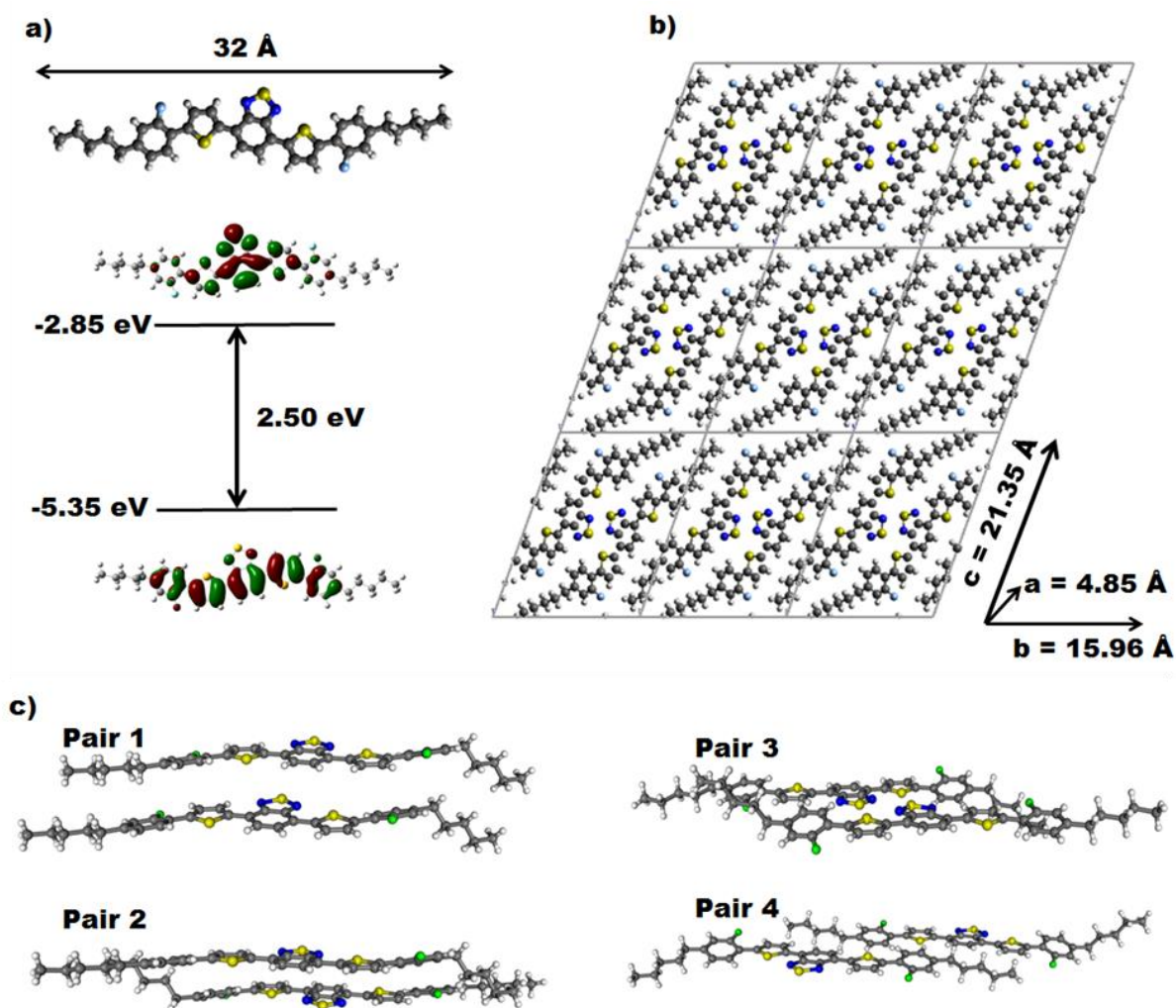


Figure 4.1: a) Molecular structure and the calculated HOMO and LUMO of FPPTB b) triclinic lattice of FPPTB showing 9 unit cells depicted in the (100) direction c) four nearest molecular pairs in the crystal.

The powder XRD pattern of FPPTB was calculated from the unit cell parameters using the freeware *Mercury*. The experimental pattern from powder was also measured and the result compared with the calculated one shows a good agreement as depicted in Figure 4.2 below.

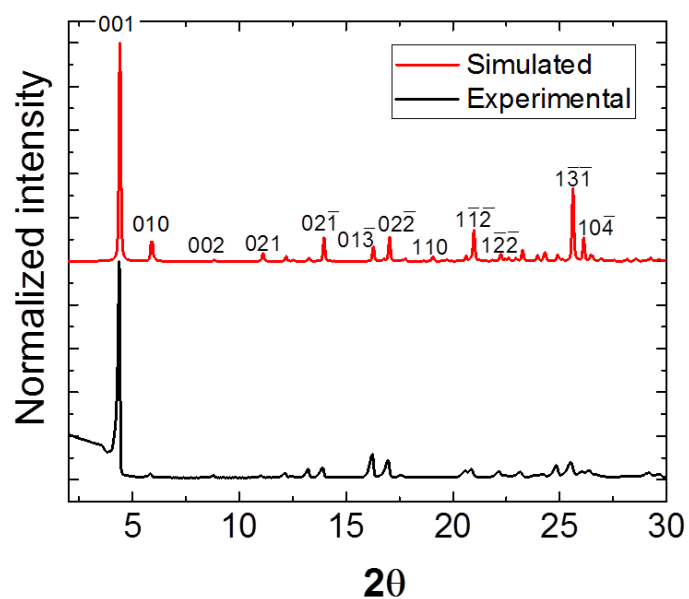


Figure 4.2: Normalized simulated (red line) and experimental (black line) XRD patterns. The most prominent peaks are labelled.

Figure 4.3 shows the absorption (black line) and emission spectra (red and blue lines) of FPPTB in dilute THF solution. The absorption spectrum exhibits two peaks, and the molar extinction coefficient of FPPTB was found to be $40\,000\text{ M}^{-1}\text{ cm}^{-1}$ at 345 nm and $29\,000\text{ M}^{-1}\text{ cm}^{-1}$ at 491 nm. The maximum at 491 nm agrees with the calculated optical bandgap of FPPTB of 496 nm. The emission spectrum is red shifted with respect to the absorption spectrum and centered at 610 nm. Any dependence of the fluorescence spectra on excitation wavelength was observed, and emission spectra taken for excitation at 350 nm and 480 nm are shown.

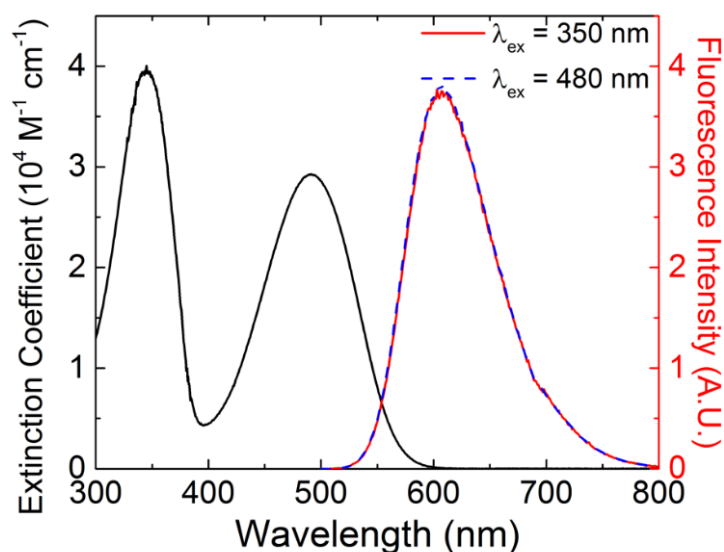


Figure 4.3: Absorption spectrum (black line) and emission spectra taken at excitation wavelengths of 350 nm (red line) and 480 nm (blue line) of FPPTB in solution (THF).

To confirm DSC measurements, in-situ polarized optical microscopy (POM) on FPPTB film spun on glass were performed. The POM studies were done during heating and cooling of the sample to monitor variations in the phase transition temperatures. Figure 4.4 shows the POM images taken from a FPPTB film during heating. Birefringence was observed in the films indicating highly ordered domains, while increasing the temperature of the stage from room temperature up to 160 °C (Figure 4.4-a). The transition to the nematic phase is observed to begin above 160 °C (Figure 4.4-a) and b), and is complete at 165 °C (Figure 4.4-c). Finally the LC film melts and the isotropic phase is observed at 247 °C (Figure 4.4-d).

Upon cooling the transition from the isotropic to nematic phase is very comparable to the heating cycle. Only the transition from nematic to crystalline changes relative to the heating cycle, and this transition was observed at 135 °C during cooling. Generally some shifts were observed in the transition temperatures with respect to the DSC results. This may be due to additional interactions in thin film. The phase transition temperatures observed during the POM measurements are summarized in Table 4.1. Measurements were repeated on ITO substrates, and no variations in the phase transitions temperature was observed.

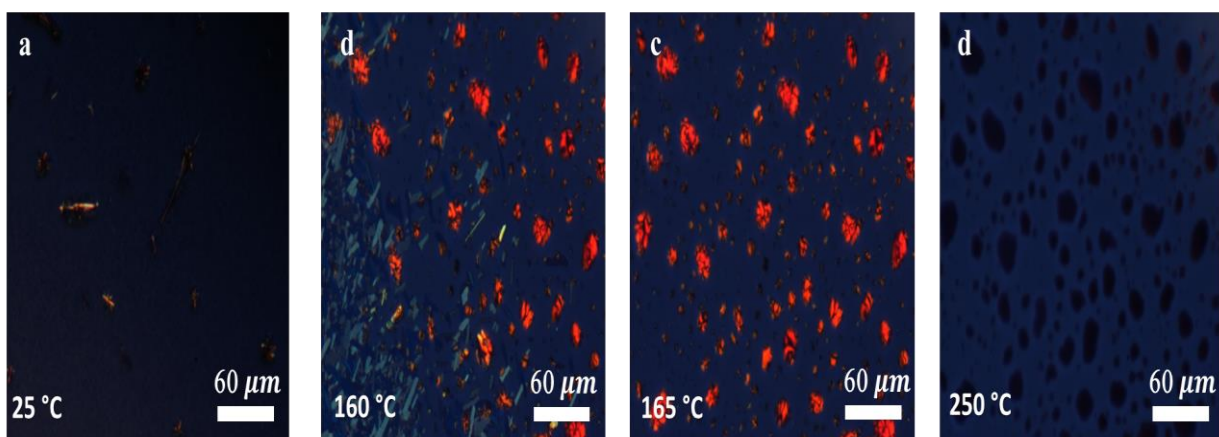


Figure 4.4: FPPTB thin film spin-coated on glass slide observed under a polarized optical microscope (POM) at **a)** room temperature and a stage temperature of **b)** 160 °C (transition crystalline → nematic) **c)** 165 °C (nematic phase) **d)** 250 °C (isotropic melt) during heating at the rate of 10 °C/min.

Table 4.1: Phase transition temperature of FPPTB during heating (10 °C/min) and cooling (20 °C/min) on film, performed on glass.

	Phase transition temperature during heating	Phase transition temperature during cooling
Phase		
Crystalline	< 160	< 135
Nematic	160	135
Isotropic	249	246

4.1.2. Molecular packing in FPPTB films

The temperature-dependent molecular packing of FPPTB thin films was studied, to determine the influence of intermolecular interactions and molecular interactions with the substrate^[111] on the phase transition temperatures and film structure. Normalized XRD patterns taken from a FPPTB film during heating and cooling are depicted in Figure 4.5-a) and Figure 4.5-b), respectively. As-spun FPPTB films demonstrated a weak peak at $2\theta = 2.72^\circ$, which corresponds to a lattice spacing of 32.5 Å. This value is consistent with the length of the FPPTB molecule. This indicates that although FPPTB is crystalline at room temperature, spin

casting FPPTB films does not enable film formation consistent with the packing structure shown in Figure 4.1-b). Instead, as-spun films demonstrate head-to-head molecular stacking. When the film is heated to 70 °C an additional peak at $2\theta = 4.14^\circ$ (lattice spacing of 21.3 Å) is observed. At 100 °C a prominent peak at $2\theta = 3.77^\circ$ (lattice spacing of 23.46 Å) emerges, while the intensity of the peak at 4.14 (lattice spacing of 21.3 Å) decreases and the peak at $2\theta = 2.72^\circ$ disappears. At 140 °C the peak at $2\theta = 3.77^\circ$ (lattice spacing of 23.46 Å) is the most prominent, and a second weaker peak at $2\theta = 7.54^\circ$ is observed. Because this peak is hardly visible in Figure 4.5-a), it is shown in higher magnification in Figure 4.6-b). This pair of peaks is consistent with the (001) and (002) planes (See Figure 4.2). This indicates the formation of highly ordered FPPTB molecular layers oriented parallel to the substrate, with the c-axis of the unit cell oriented perpendicular to the substrate at temperatures between 100 °C and 140 °C. At 155 °C any peaks associated with crystalline structure was observed, indicating the film is in the nematic phase at this temperature.

During the cooling cycle, no peaks associated with the crystal structure are observed in spectra taken between 250 °C and 140 °C (Figure 4.5-b)). This gives indication that the film is still in the nematic phase at 140 °C during cooling. Peaks associated with the crystal structure first emerge in spectra taken at 100 °C and 70 °C, but with reduced relative intensity compared to the heating cycle.

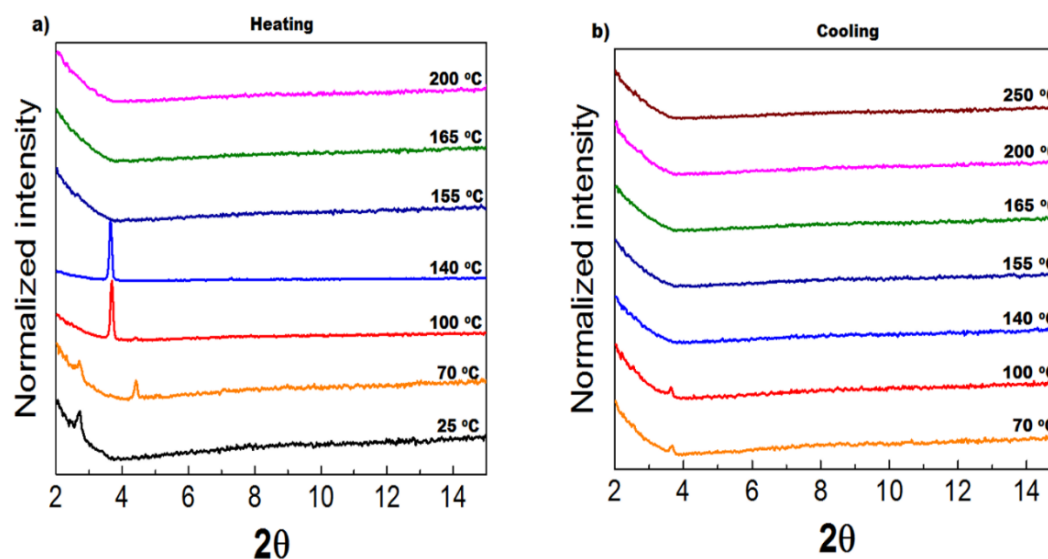


Figure 4.5: In-situ XRD patterns of an FPPTB film taken during a) heating and b) cooling.

The effect of cooling from the different phases (crystalline, nematic and isotropic) on molecular packing in FPPTB films at room temperature was thereafter investigated. As-spun FPPTB films (crystalline phase), and FPPTB films annealed at 140 °C (just below the transition crystalline → nematic), 165 °C (nematic phase) and 250 °C (isotropic melt) were prepared and the FPPTB films were characterized after cooling to room temperature (crystalline phase). The normalized XRD patterns of an as-spun FPPTB film (black) and FPPTB films annealed at 140 °C (blue), 165 °C (green) and 250 °C (wine) is shown in Figure 4.6-a). The pattern from the as-spun film is consistent with the pattern of the as-spun film in Figure 4.5-a), and demonstrates signatures of head to head stacking of FPPTB molecules. Annealed FPPTB films, on the other hand, yield XRD peaks consistent with molecular crystal packing depicted in Figure 4.1-b), and the $\Delta\theta$ peaks corresponding to the (001) and (002) crystal planes were observed. FPPTB films annealed at 140 °C demonstrate the most prominent and narrow peaks. In contrast, FPPTB annealed at 165 °C (nematic phase) and 250 °C (isotropic melt) show a slight shift in the peaks, and the (001) peak shifts from $2\theta = 3.77^\circ$ to $2\theta = 3.74^\circ$, corresponding to a slight increase in the lattice spacing from 23.46 Å to 23.59 Å. In addition the relative intensity of both the (001) and (002) peaks decreases, and the peaks broaden. This effect is illustrated in Figure 4.6-b) shows the zoom in of the XRD pattern centered on the (002) peak. Shifting of molecules in the unit cell relative to nearest neighbors induces variations in local order (resulting in peak broadening) as well as a change in the dimensions of the unit cell (resulting in peak shifting).

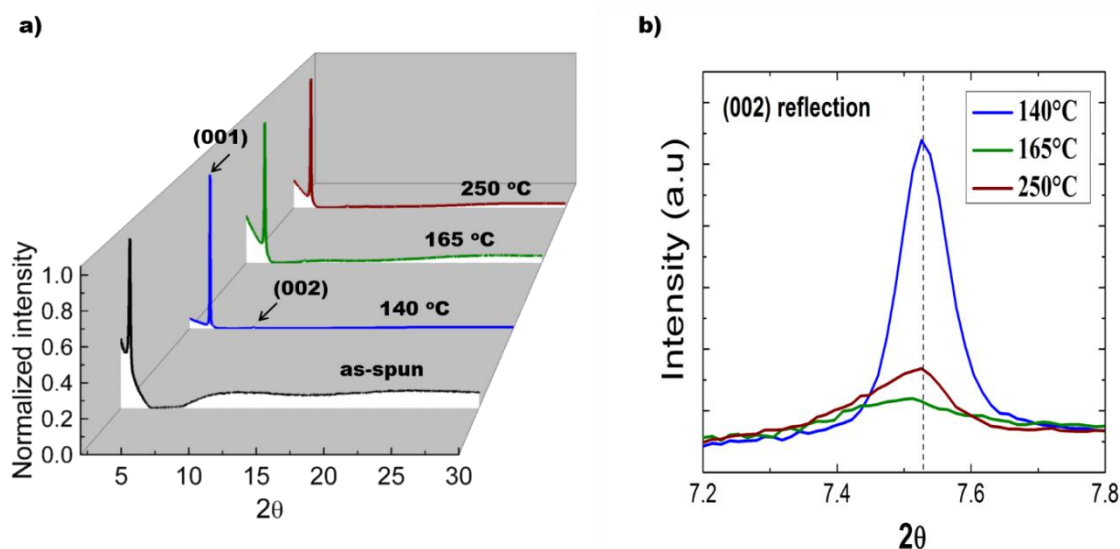


Figure 4.6: a) normalized XRD patterns of as-spun FPPTB (black), and FPPTB films annealed at 140 °C (blue), 165 °C (green) and 250 °C (wine) b) non-normalized XRD patterns of films annealed at FPPTB films annealed at 140 °C (blue), 165 °C (green) and 250 °C (wine).

Polarized optical microscopy images of the FPPTB films as-spun as well as those annealed at 140 °C, 165 °C and 250 °C are shown in Figure 4.7-a), b), c) and d) respectively. All of the films are crystalline and the size of the crystal domains increases with annealing temperature.

Obtaining crystalline films with LC materials generally requires cooling through ordered smectic phases to avoid grain boundaries, cracking and droplet formation due to de-wetting [8,21]. Despite the lack of a smectic phase for FPPTB, an excellent film coverage was observed (Figure 4.7) and it was also found that the structural integrity is high even for films that were cooled from the isotropic melt. This was attributed to increased short range intermolecular interactions in the nematic phase and isotropic melt. This leads to asymmetric heating and cooling behavior; the transition between the nematic and crystalline phase occurs at lower temperatures during film cooling than film heating. During cooling, the intermolecular interactions promote local molecular displacement in the crystal packing, as evidenced by broadening and shifting of the (001) and (002) signatures (Figure 4.6 b)). As a result, slow cooling from the nematic phase (165 °C) and the isotropic melt (250 °C) promotes the formation of large domains with local structural defects in the molecular packing structure, compared to FPPTB films annealed in the crystalline phase (140 °C).

The difference in the temperature of the transition from crystalline \rightarrow nematic during heating, and nematic \rightarrow crystalline during cooling was advantageous for realizing thermally stable organic films for device applications^[8]. FPPTB films can be deposited and processed in a wide temperature window, allowing for more flexibility in film fabrication. At the same time, FPPTB film structure and integrity is maintained at elevated operating temperatures (up to 140 °C).

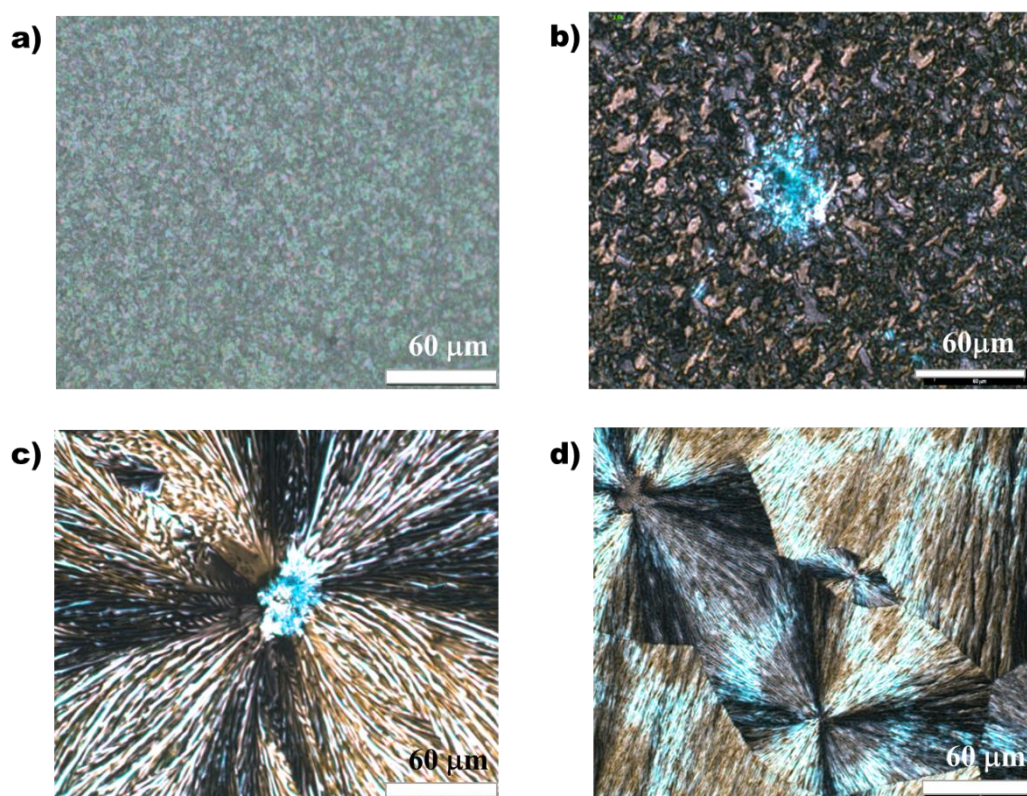


Figure 4.7: Polarized optical microscopy images of **a)** as-spun FPPTB and FPPTB films annealed at **b)** 140 °C, **c)** 165 °C and **d)** 250 °C. These textures were taken at a magnification of 20x, at a scale of 60 μm in length.

4.1.3. Optical properties

Emission spectra of as-spun FPPTB films (black squares) and FPPTB films annealed at 100 °C (red triangles), 140 °C (blue circles), 165 °C (green stars) and 250 °C (wine crosses) are shown in Figure 4.8-a). It is observed that emission yield is highest in FPPTB films with ordered packing structure (140 °C and 100 °C), intermediate in FPPTB films which exhibit

variations in local molecular packing (165 °C and 250 °C), and lowest in FPPTB films with reduced long range order (as-spun).

To gain more insight into the role of molecular packing on the emission line shape, the normalized spectra (Figure 4.8-b)) was investigated in more detail. It was observed that emission line shape is dependent on annealing conditions, although films annealed at 165 °C (nematic) and 250 °C (isotropic) exhibit identical spectral form when normalized.

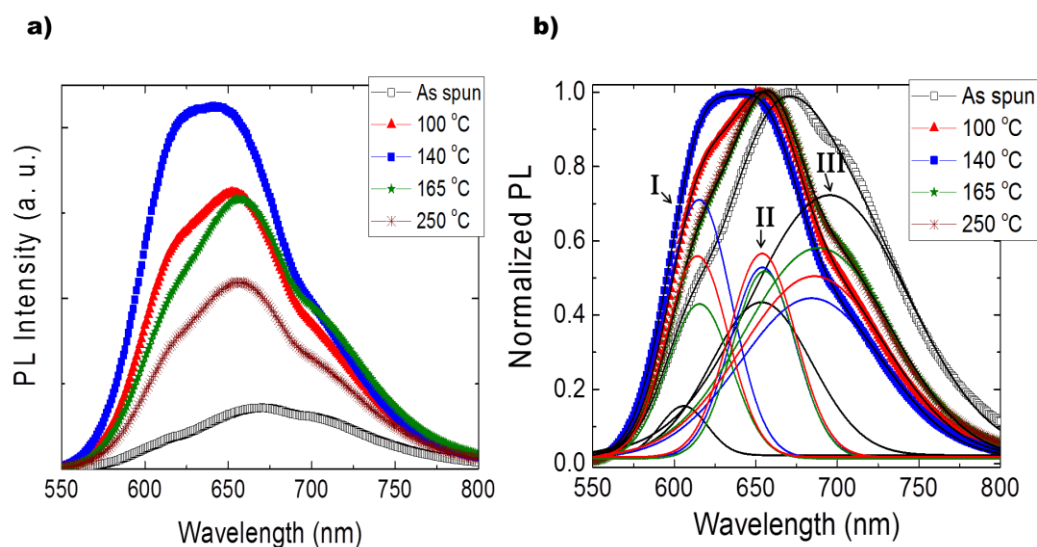


Figure 4.8: **a)** Emission spectra of as-spun FPPTB films (black squares) and FPPTB films annealed at 100 °C (red triangles), 140 °C (blue circles), 165 °C (green stars) and 250 °C (wine crosses). **b)** Normalized emission spectra from the FPPTB films fitted along with three Gaussian distributions, which are denoted as: **I** – high energy, **II** – intermediate energy and **III** – low energy contribution, respectively.

Gas-to-crystal shifts in the optical spectra of crystalline organic films are determined by variations in packing structure as well as localized, site-dependent interactions, which can lead to distinct features in the spectra.^[112] The emission spectra from the FPPTB films is fitted as a combination of three Gaussian distributions, which were denoted as the **I** – high energy, **II** – intermediate energy and **III** – low energy contribution, respectively. This simple model is used to fit all the spectra and the peak position of the Gaussian distributions were free fitting parameters. It was found that the peak positions of the three distributions are nearly identical for all samples, and that the relative intensity of each distribution determined the spectral lineshape.

The high energy feature **I** is centered at 605 nm for the as spun FPPTB film and broadens and shifts to 615 nm for all the annealed films. The intensity is highest in FPPTB films annealed in the crystalline phase (100 °C and 140 °C), lower in FPPTB annealed at in the nematic phase (165 °C) and isotropic melt (250 °C) and lowest in as-spun FPPTB films. The peak position of this feature is slightly red-shifted from the monomer emission in solution (600 nm), and this feature is attributed to monomer-like emission from molecules in bulk FPPTB crystallites. Quenching of emission from this feature is consistent with reduced long range crystal order (as-spun FPPTB) as well as local changes in FPPTB packing (FPPTB annealed at 165 °C and 250 °C).

The intermediate energy feature **II** is centered at 653 nm, and no change in peak position with annealing was observed. The intensity is lowest and the distribution is the broadest in the PL spectrum from the as-spun film. The width of this distribution is identical for the annealed FPPTB films, and the relative intensity varies only slightly between the PL spectra taken from these samples. This feature is attributed to coupling between molecular pairs in bulk FPPTB crystallites (Figure 4.1-b) and Figure 4.1-c)).

Finally the low energy feature **III** is considered. The relative intensity and peak position of this feature show the most dependence on annealing conditions of all three features. The relative intensity is the highest for the as-spun FPPTB film (695 nm) and lowest for the FPPTB film annealed at 140 °C (684 nm). The increase in peak intensity and width, as well as the red-shifting of peak position of the Gaussian feature directly correlate with reduced long range molecular order in the films. For this reason this feature is tentatively attributed to variations in short-range coupling between molecular pairs in the FPPTB crystal.

4.1.4. Electrical properties

The geometry of the FPPTB HOMO (Figure 4.1) indicates that the hole wavefunction is delocalized over the conjugated backbone and hole transport occurs via π - π overlap between neighboring molecules. FPPTB forms stacked layers running perpendicular to the substrate, and transport is limited by charge transfer between layers. The geometry of the LUMO, on the other hand, indicates that electron transfer is determined primarily by alignment of the benzodithiazole acceptor units between molecular pairs. Shifts in molecular pairs can increase lateral electron mobility along the (100) and (010) direction. For carrier transport in

FPPTB diodes, however, changes in molecular placement along the direction of transport, i.e. along the c-axis, are most relevant. For this reason we focus on studying hole transport in FPPTB. “Hole only” diodes were prepared according to the details in the experimental section, with the architecture given in Figure 4.9-a).

The current density-voltage (JV) characteristics are shown in Figure 4.9-b) for diodes prepared with as spun FPPTB films (black squares) and FPPTB films annealed at 140 °C (blue circles), 100 °C (red triangles), 165 °C (green stars) and 250 °C (wine crosses). The current density of annealed FPPTB is higher than in as-spun FPPTB films, and current density increases with increasing annealing temperature. Diodes prepared with FPPTB films annealed at 100 °C and 140 °C demonstrate very similar JV characteristics, while FPPTB annealed at 250 °C has the highest current density of all samples.

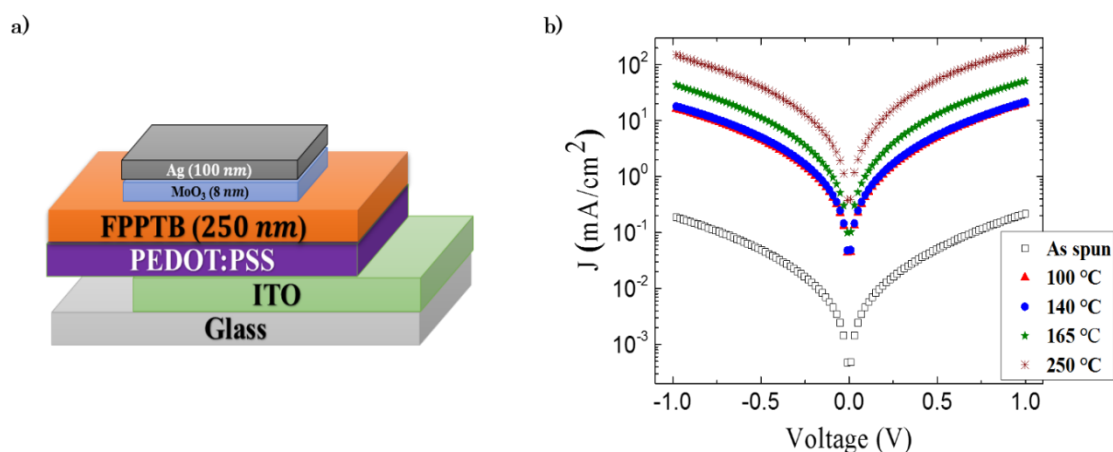


Figure 4.9: a) Single carrier device architecture ; b) The current density-voltage (JV) characteristics for diodes prepared with as spun FPPTB films (black squares) and FPPTB films annealed at 140 °C (blue circles), 100 °C (red triangles), 165 °C (green stars) and 250 °C (wine crosses).

Impedance spectroscopy was performed in order to understand the electrical properties of FPPTB in more detail. In particular the influence of annealing on film resistance and dispersive transport phenomena was investigated. Liquid crystalline semiconductors generally demonstrate narrow energetic distributions for electronic transport with reduced trapping and limited or no dispersive transport.^[15] Structural and chemical defects, however, cause dispersive carrier transport^[113] manifested as voltage-dependent mobility values.^[111]

The Nyquist plots ($-Z''$ versus Z') from the impedance data taken over a frequency range between 1 MHz and 10 Hz are shown in Figure 4.10-a). The experimental (symbols) data were taken at a DC offset of 0 V and fit with an equivalent circuit model (lines). Because the impedance values are much higher for diodes prepared with as-spun FPPTB films, Figure 4.10-a) shows all the data, while for clarity Figure 4.10-b) depicts a zoom-in of the impedance data from the diodes prepared with annealed films (100 °C – red triangles, 140 °C – blue circles, 165 °C – green stars and 250 °C – wine crosses).

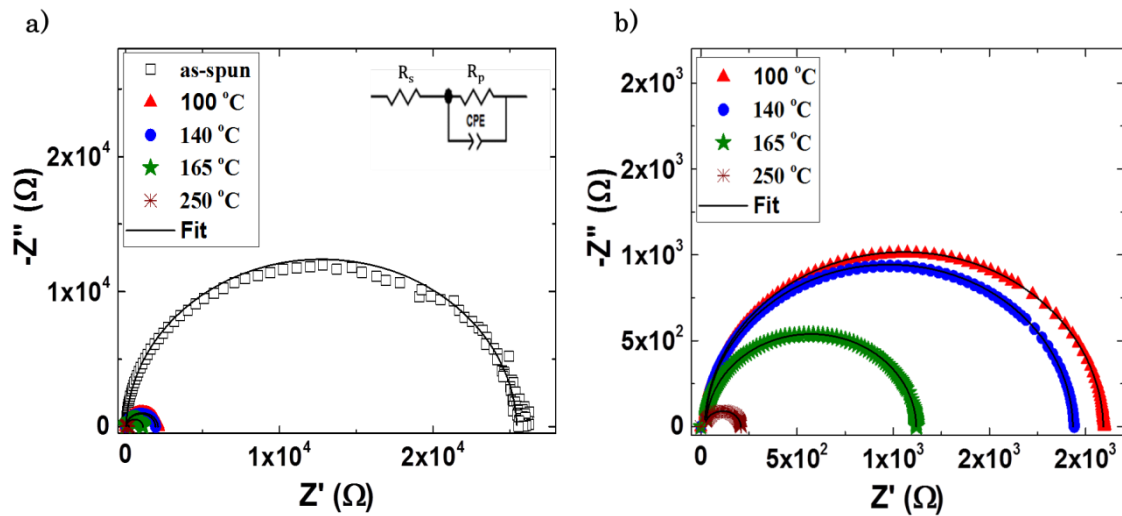


Figure 4.10: a) The Cole-Cole plots ($-Z''$ versus Z') from the impedance data taken over a frequency range between 1 MHz and 10 Hz). b) Zoom-in of the impedance data from the diodes prepared with annealed films (100 °C – red triangles, 140 °C – blue circles, 165 °C – green stars and 250 °C – wine crosses).

A simple equivalent circuit was applied to model the data, consisting of a series resistance (R_s) and a resistor (R_p) in parallel with a constant phase element (CPE). The equivalent circuit diagram is shown in the inset of Figure 4.10-a). R_s is determined by the contact resistance, and is therefore frequency-independent and comparable between samples. A series resistance R_s will shift the frequency dependent data towards higher values on the real axis Z as illustrate in Figure 4.12-a). The values of the R_p -CPE element are determined by the electrical properties of the FPPTB film.

CPE values depend on the frequency-dependent capacitance of the film. Specifically the CPE accounts for non-idealities in the device capacitance, i.e. dispersive transport, and is given by

$$CPE = \frac{1}{Z_o(i\omega)^n} \quad (16)$$

where Z_o is the impedance of the **CPE** at low frequency (1 rad/s), and n is a dimensionless parameter between 0 and 1. If $n = 1$, the **CPE** reduces to an ideal capacitor and if $n = 0$, the **CPE** reduces to an ideal resistor. The values of the circuit elements, along with the annealing temperatures for each sample, are summarized in Table 4.2. It is noted that the value of n for all of the samples was between 0.98 (as-spun FPPTB) and 0.99 (annealed FPPTB) indicating nearly ideal capacitive behavior, and negligible dispersive transport, independent of annealing conditions. The capacitive value of the **CPE** element (taken at $\omega = 1$ rad/s) varies slightly between the samples, from 3.46 nF to 5.84 nF, and no trend with annealing is observed. The most significant difference between the electrical properties of the FPPTB films is the decrease in R_p with annealing temperature, from 25400 Ω (as-spun FPPTB) to 188 Ω (FPPTB annealed at 250 $^{\circ}\text{C}$). The decrease in FPPTB film resistance with annealing temperature is consistent with the increase in crystal domain size observed in Figure 4.7, i.e. the decrease in grain boundaries in the film.

Table 4.2: Values for circuit elements (R_s , R_p and CPE) for diodes prepared with FPPTB which was not annealed, and annealed at 100 $^{\circ}\text{C}$, 140 $^{\circ}\text{C}$, 165 $^{\circ}\text{C}$ and 250 $^{\circ}\text{C}$.

Annealing temperature ($^{\circ}\text{C}$)	R_s (Ω)	R_p (Ω)	CPE at $\omega = 1$ rad/s (nF)	N
As spun	21.7	25400	3.46	0.98
100	19.7	2072	4.48	0.99
140	23.2	1910	3.38	0.99
165	25.9	1094	3.34	0.99
250	19.7	188	5.84	0.99

Figure 4.11-a) shows the Bode plots for $-Z''$ versus f spectra for the samples. The charge carrier mobility μ can be determined from these data according to the equation (13), described in the second chapter.

The hole mobility values versus annealing temperature are shown in Figure 4.11-b). Carrier mobility increases over two orders of magnitude from $\mu = (2.2 \pm 0.4) \times 10^{-5} \text{cm}^2 \text{V}^{-1} \text{s}^{-1}$ in

as spun films to $\mu = (5.0 \pm 0.8) \times 10^{-3} \text{ cm}^2 \text{ V}^{-1} \text{ s}^{-1}$ in films annealed at 250 °C. There was no voltage dependence in the carrier mobility observed, consistent with non-dispersive transport.

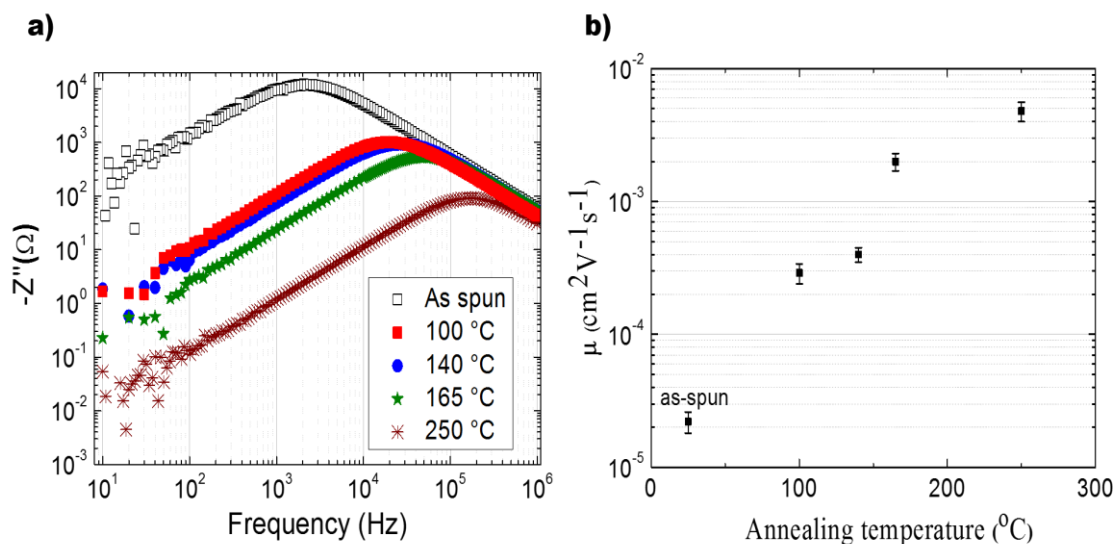


Figure 4.11: a) Bode plots for $-Z''$ versus f spectra for the samples of FPPTB with annealed films (100 °C – red triangles, 140 °C – blue circles, 165 °C – green stars and 250 °C – wine crosses) and **b)** The carrier mobility in FPPTB versus annealing temperature.

The increase in the carrier mobility with annealing temperature by two orders of magnitude is consistent with the decrease in the FPPTB film resistance. The resistance and conductivity values vs annealing temperature are plotted in Figure 4.12-b). This confirms that the conductance drastically increases upon annealing, which also demonstrates the consistency of impedance spectroscopy as a tool to extract the mobility ($\text{Im } Z$ vs f).

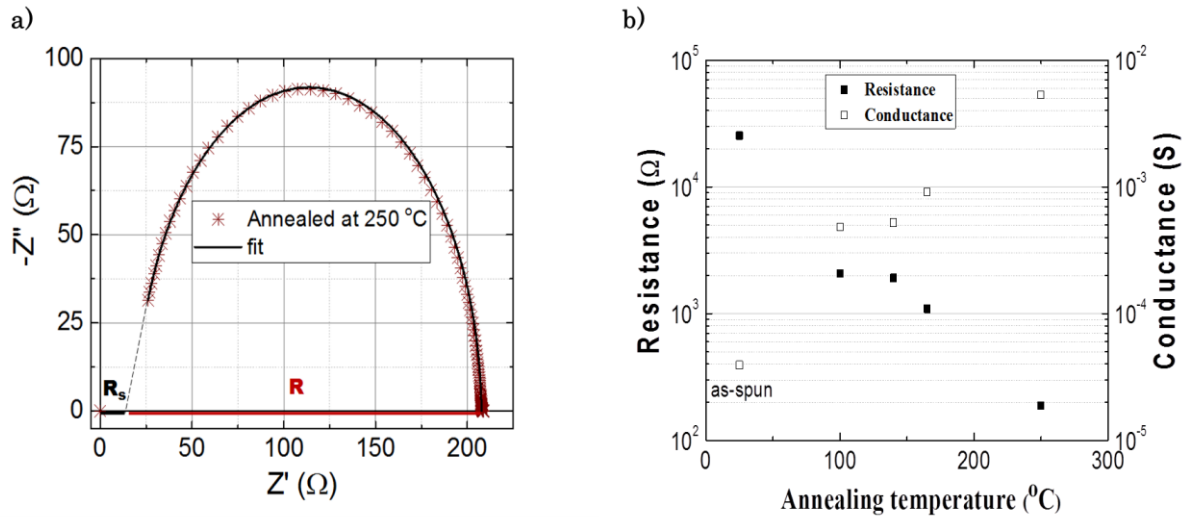


Figure 4.12: a) Cole-Cole plot ($-Z''$ versus Z') of impedance data taken over a frequency range between 1 MHz and 10 Hz) for a diode prepared with FPPTB annealed film at 250 °C. The solid line shows the simulation using a simple R-CPE equivalent circuit. The dashed line is intended as a guide for the eye to demonstrate the shift of the frequency dependent data along the real axis. The series resistance R_s and total device resistance R are labelled. b) Resistance and conductivity values vs annealing temperature in FPPTB.

The increase in carrier mobility with annealing temperature is considered in terms of the interplay between long range crystalline order and short range π - π interactions in FPPTB films. It is observed that crystal domain size in FPPTB films (Figure 4.7-a) – d)) increases with annealing temperature, corresponding to a decrease in the density of grain boundaries in the film. This is consistent with a decrease in FPPTB film resistance R_p and an increase in carrier mobility.^[54, 114] However annealing FPPTB at higher temperatures also induces local variations in molecular packing. This is evidenced by slight increase in the unit cell along the (001) plane and increased emission quenching in films annealed in the nematic phase and isotropic melt.

Local shifts in molecular position will influence the overlap of the electronic wavefunction between molecular pairs, and therefore the electron transfer rate^[76,115]. In particular, changes in intermolecular distances in the crystal packing structure that are mediated by short range π - π interactions may lead to smaller intermolecular distances and increased electron transfer rates. Relative slipping of molecules in the (100) and (010) planes, corresponding to increased π - π interactions between molecular pairs 2 – 4, would promote increased two dimensional hole transfer through the films^[27, 115]. This is consistent with the increase in carrier mobility

that was observed when cooling FPPTB films from the nematic phase and isotropic melt, which in turn is correlated with a decreased density of grain boundaries in the films.

Summary

The novel calamitic LC dye FPPTB was investigated. FPPTB is easily processed from solution and forms crystalline films at temperatures below 149 °C, exhibits a nematic phase at temperatures between 149 °C and 230 °C and is isotropic at temperatures above 230 °C. XRD and luminescence data revealed that annealing FPPTB films at temperatures just below the crystalline → nematic transition (140 °C) yielded films with the best crystalline order. Cooling FPPTB films from the nematic phase and isotropic melt led to decreased density of grain boundaries in the films. However, evidence of local structural defects in the crystal packing were observed in the XRD patterns from these films, and was attributed to increased short-range coupling between molecular pairs at higher temperatures which persisted upon cooling the films to the crystalline phase. Carrier mobility was observed to increase over two orders of magnitude with annealing, from $\mu = (2.2 \pm 0.4) \times 10^{-5} \text{ cm}^2 \text{ V}^{-1} \text{ s}^{-1}$ in as spun FPPTB films to $\mu = (5.0 \pm 0.8) \times 10^{-3} \text{ cm}^2 \text{ V}^{-1} \text{ s}^{-1}$ in FPPTB films cooled from the isotropic melt. The resultant correlation between charge carrier mobility and annealing is explained by an interplay between long and short range order interactions in these 3-dimensional structures. These results demonstrate that for LCs such as FPPTB, judicious choice of processing conditions can be used to tune electronic parameters for targeted device design.

4.2. The influence of fluorine substitution on molecular packing and carrier mobility in liquid crystal dyes 2, 6-FPPTB and 2, 3-FPPTB

In the precedent chapter, the results lead to the conclusion that charge carrier transport in conjugated liquid crystal dyes is governed by the interplay between the long range crystal order, and the short range molecular interaction in the film. In this current chapter, the focus is to understand how small modifications in molecular structure of LC dyes influence molecular packing and charge carrier mobility. For this, two liquid crystal dyes namely 2,3-FPPTB and 2,6-FPPTB exhibiting very similar molecular structures with a significant difference in their mesophase, are investigated.

4.2.1. Molecular properties of 2, 3-FPPTB & 2, 6-FPPTB

Molecular structures of 2,3-FPPTB and 2, 6-FPPTB are given in Figure 4.13 together with their HOMO and LUMO orbitals. The calculated HOMO and LUMO are respectively -4.95 eV and -2.56 eV for 2, 3-FPPTB; and -5.00 eV and -2.60 eV for 2, 6-FPPTB. The two molecular compounds exhibit similar band gaps as shown in Figure 4.13.

The phase transition temperatures and enthalpies of both compounds as detailed in the second chapter, indicated significant difference in mesophase amongst the two molecular compounds, which is attributed to the position of fluorine molecules on the molecular backbones.

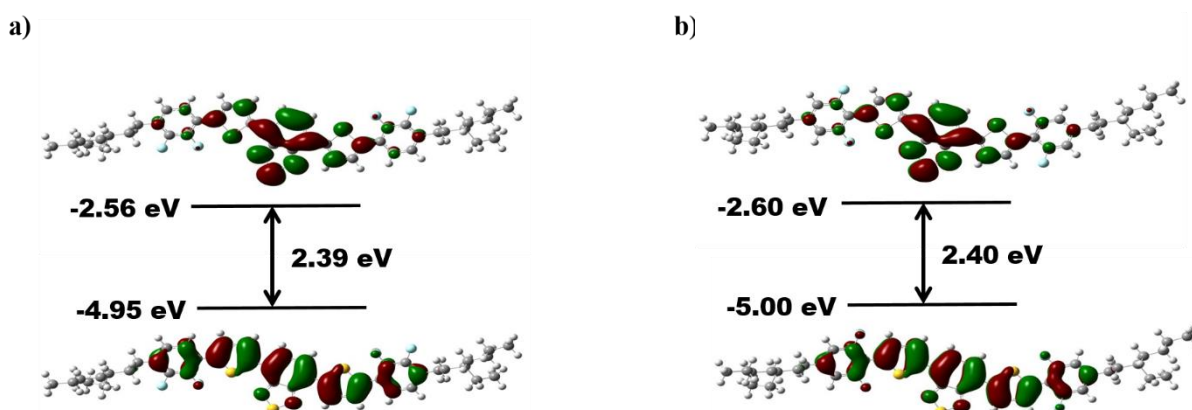


Figure 4.13: Molecular structure together with the calculated (HOMO) and (LUMO) of FPPTB of a) 2,3-FPPTB; b) 2,6-FPPTB.

The molecular electrostatic potential (MEP) maps of 2,3-FFPTB and 2,6-FFPTB molecules were also calculated and the corresponding maps are depicted in Figure 4.14. Electrostatic potential maps are three dimensional diagrams of molecules enabling the visualization of charge distributions and charge related properties of molecules. This map allows measuring the electrostatic potential energy along the molecular backbone, essentially reflecting the strength of the nearby charges, nuclei and electrons, as a function of position. The colour spectrum (Figure 4.14) indicates the varying intensities of the electrostatic potential energy values. The red and blue colours refer to the lowest and the highest electrostatic potential energy value respectively. Consequently, the areas of low potential (red) are characterized by an abundance of electrons while those of high potential (blue), are characterized by a relative absence of electrons ^[116].

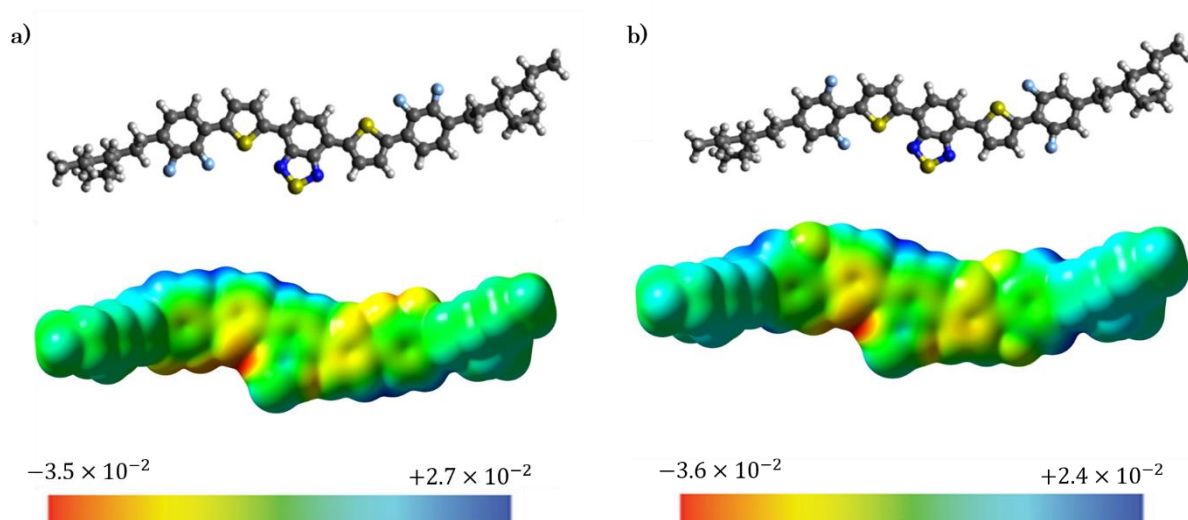


Figure 4.14: Molecular structure given with the MEP maps of **a)** 2,3-FFPTB; **b)** 2,6-FFPTB. The color map scales indicate the most positive potential region (deepest blue color) and most negative potential regions (deepest red color) in the active sites of 2,3-FFPTB and 2,6-FFPTB.

A significant difference in the electrostatic maps of the two molecules was not observed. For the lowest potential regions where electrons is densely distributed, the measured energies were -3.5×10^{-2} and -3.6×10^{-2} for 2,3-FFPTB and 2,6-FFPTB respectively; for highest potential regions with less density in electrons, these were $+2.7 \times 10^{-2}$ and 2.4×10^{-2} for 2,3-FFPTB and 2,6-FFPTB respectively, as indicated in the Figure. However, the small

variations observed in the maps can significantly influence the molecular packing of the two molecules [117-119].

For this work, Raman measurements were recorded by Dr. Simon Boehme at the VU Amsterdam, by the mean of a confocal Renishaw inVia spectrometer, using cw-laser excitation at 785 nm. An objective with 50x magnification was employed both for the excitation and the collection of the scattered light. The measurements were performed on liquid crystal films spincoated on CaF₂ substrates, for elimination/minimization of fluorescence background effects.

Figure 4.15-a) shows the normalized Raman spectra of 2,3-FFPTB (red) and 2,6-FFPTB (blue). As depicted in the figure, the spectra are very similar in terms of bands intensity and wavenumber shifts but show differences in the regions 1420 – 1470 cm⁻¹ and 1510 – 1560 cm⁻¹. In the spectral regions 1420 – 1470 cm⁻¹ and 1510 – 1560 cm⁻¹ shown as zoom-in in Figure 4.15-b), 2,3-FFPTB appears to show an additional mode at 1450 cm⁻¹ which is not seen in 2,6-FFPTB. The Raman active vibrations in this region involve C-C, C-F bonds and C-C-F stretching which are localized on the benzene rings [120-122].

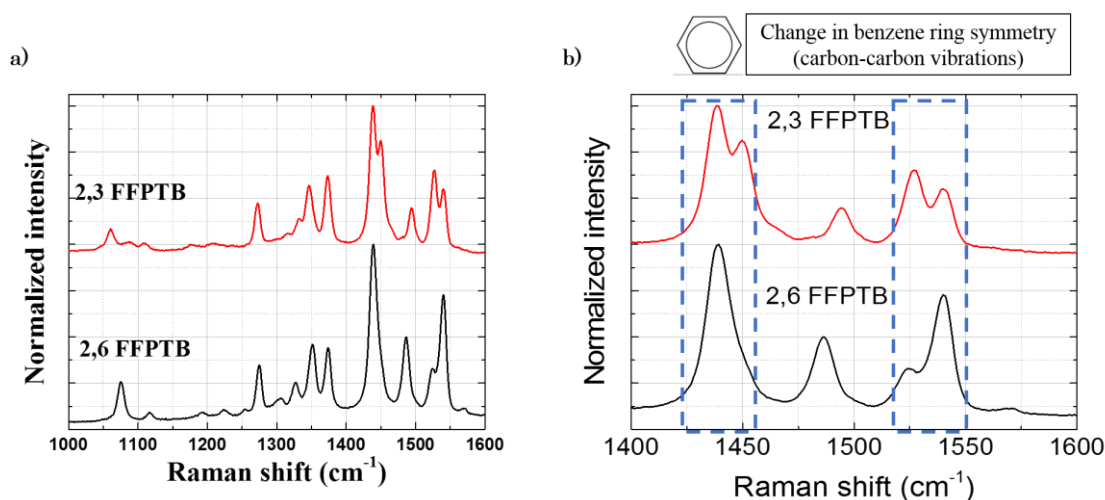


Figure 4.15: a) The Raman spectra (fingerprint region) of 2,3-FFPTB (red) and 2,6-FFPTB (black); b) Zoom-in in the spectral region 1420 – 1470 cm⁻¹, where the contribution of benzene ring is affected by the fluorine substitution.

The Raman signatures exhibit strong contributions from vibrational modes associated with the benzene ring, and these are influenced by the location of the F substitution (ortho or para).

Figure 4.16 shows the comparison between measured and theoretically calculated Raman spectra. The calculated spectra qualitatively reproduce the experimental spectra, with an exception of a red-shift (of $\sim 50 \text{ cm}^{-1}$).

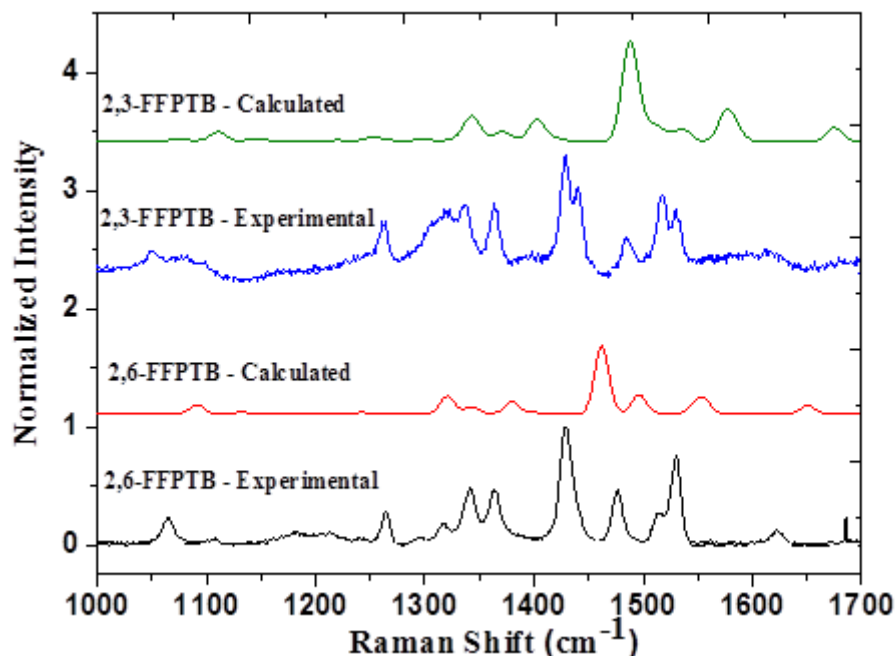


Figure 4.16: Normalized Raman spectra of 2,6-FFPTB: Experimental (black line) and calculated (red line) and 2,3-FFPTB: Experimental (blue line) and experimental (green line).

The experimental spectrum is confirmed by the theoretically calculated spectra. The differences are attributed to modification of the vibrational modes related to the benzene ring.

Figure 4.17) shows the absorption spectra of 2,6-FFPTB (dark-blue) and 2,3-FFPTB (red) together with their emission spectra taken at excitation wavelengths of 450 nm (2,6-FFPTB) and 490 nm (2,3-FFPTB) in solution (CHCl_3). The fluorescence spectra were taken at different excitation wavelengths (375nm, 450nm, 490nm and 530nm), and no dependence of the spectra on the wavelength was observed. As expected from the optical band values, the absorption and emission spectra of 2,3-FFPTB and 2,6-FFPTB are very similar, and the 2,3-FFPTB spectra are slightly red-shifted from that of 2,6-FFPTB subsequent to the slight decrease of its optical band gap (2,49 eV) relatively to 2,6-FFPTB (2,50 eV). 2,3-FFPTB absorption spectrum exhibits its maxima at 341 nm and 488 nm while 2,6-FFPTB absorption spectrum exhibits two peaks at 336 nm and 483 nm. For both compounds, the emission spectrum is red-shifted from the absorption and is centered at 671 nm for 2,6-FFPTB and 674

nm for 2,3-FFPTB. These results from solution indicate that both molecules exhibit very similar optical properties.

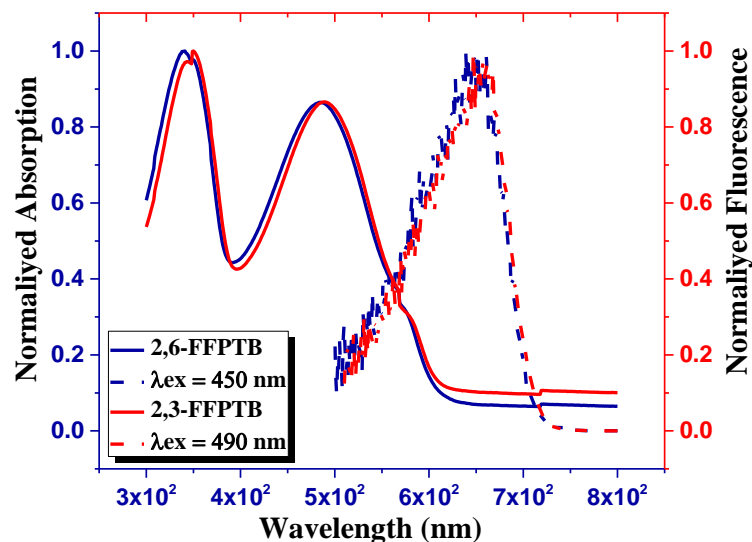


Figure 4.17: Absorption spectrum of 2,6-FFPTB (dark-blue) and 2,3-FFPTB (red) together with their emission spectra taken at excitation wavelengths of 450 nm (2,6-FFPTB) and 490 nm (2,3-FFPTB) in solution (CHCl_3).

4.2.2. Optical properties on films

Absorption and emission spectra were also measured on films. The spin coated films were homogeneous and do not show signs of cracking or dewetting. It is observed as shown in the compared absorption spectra in Figure 4.18, that the spectra on films were slightly blue-shifted in comparison to solution for 2,3-FFPTB while a slight red-shift of spectra on films, relative to the solution is observed for 2,6-FFPTB. Also, this demonstrates that differently from solution, 2,6-FFPTB spectra ($\lambda_{max} \sim 502 \text{ nm}$) on films, are red-shifted from those of 2,3-FFPTB ($\lambda_{max} \sim 466 \text{ nm}$).

Additionally 2,3-FFPTB exhibits a shoulder peak at $\lambda_{max} \sim 505 \text{ nm}$ on its second peak at $\lambda_{max} \sim 466 \text{ nm}$, while the first peak is shown at $\lambda_{max} \sim 340 \text{ nm}$. The same way, 2,6-FFPTB clearly shows a shoulder peak at $\lambda_{max} \sim 535 \text{ nm}$ on the second peak, which has a maximum at $\lambda_{max} \sim 502 \text{ nm}$, while the first peak has a maximum at $\lambda_{max} \sim 342 \text{ nm}$. The red-shift of spectra and the shoulder peaks observed on films are consistent with a modification of the intermolecular interaction and more ordered structure in the solid state. In general, the

absorption peaks for both compounds vary only slightly with the heating/cooling treatment before measurement. Additionally, the absorption intensity increases slightly with annealing upon the film suggesting that temperature treatment influences the optical properties of the materials on film.

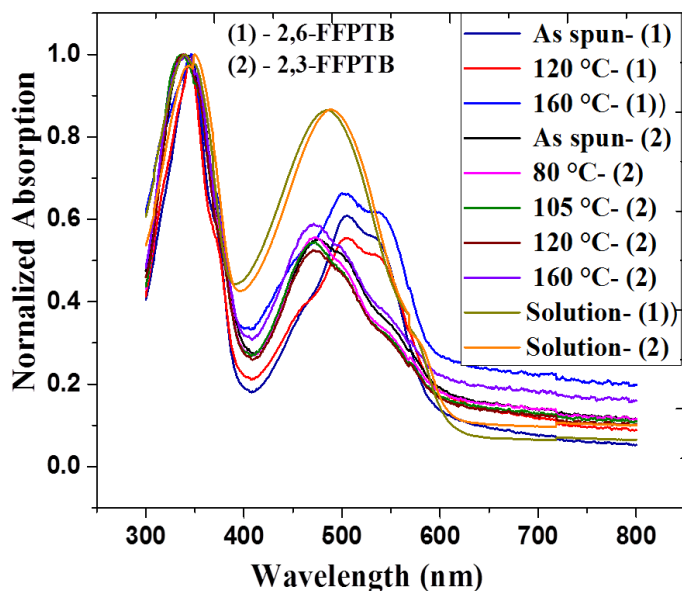


Figure 4.18: Compared absorption spectra of as-spun 2,6-FFPTB films (blue-marine), 2,6-FFPTB films annealed at 120 °C (red), 160 °C (blue); with as-spun 2,3-FFPTB (black), 2,6-FFPTB films annealed at 80 °C (pink), 105 °C (green), 120 °C (wine), 160 °C (violet).

Photoluminescence (PL) emission spectra for both molecules were measured on films as shown in Figure 4.19. No significant difference is observed for fluorescence on 2,3-FFPTB as-spun films and 2,3-FFPTB films annealed at 120 °C and 160 °C, with a maximum emission about 670 nm (Figure 4.19-a)). However, the films annealed at 80 °C and 105 °C show the maximum emission blue shifted relatively to the as-spun, at about 655nm. The fluorescence of 2,6-FFPTB shows a clear blue-shift from 653 nm (as-spun film) to 628 nm, when the film was annealed at 120 °C, just before the transition crystalline → isotropic phase (Figure 4.19-b)). And the film annealed at 160 °C is red-shifted compared to the as-spun film from 653 nm to 662 nm. The variations in features in the PL spectra were attributed to changes in molecular coupling in 2,3-FFFPTB and 2,6-FFPTB films depending on the annealing conditions.

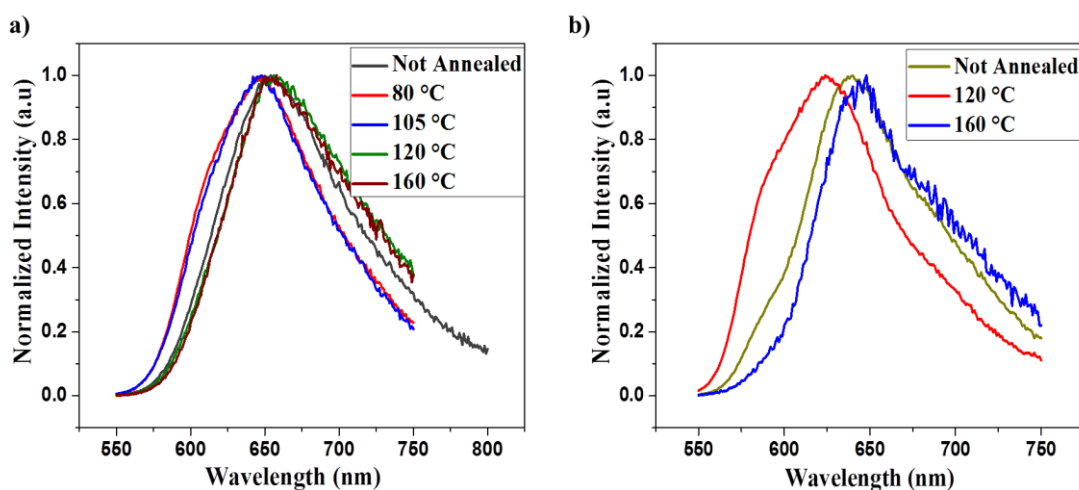


Figure 4.19: Emission spectra of **a)** as-spun 2,3-FFPTB (black), 2,6-FFPTB films annealed at 80 °C (red), 105 °C (blue), 120 °C (green) and 160 °C (wine) excited at $\lambda_{\text{ex}} = 490$ nm; **b)** as-spun 2,6-FFPTB films (dark-yellow), 2,6-FFPTB films annealed at 120 °C (red) and 160 °C (blue) at $\lambda_{\text{ex}} = 530$ nm.

In summary almost no difference was observed on optical properties of 2,3-FFPTB (two smectic phases) and 2,6-FFPTB (no smectic phase) in solution, whereas the results on films confirm a significant difference in optical properties of the two molecules when subjected to annealing through the different mesophases. These variations on optical properties on films suggest differences in molecular packing of the molecules, which is investigated by XRD in the next section.

4.2.3. Molecular packing on films

In-situ XRD

The temperature-dependence of molecular orientation on 2,3-FFPTB and 2,6-FFPTB thin films was studied using in-situ XRD. Figure 4.20 and 4.21 describe respectively the normalized XRD patterns taken from 2,3-FFPTB and 2,6-FFPTB films during heating and cooling.

- 2,3-FFPTB

The as-spun film (Figure 4.20-a)) of 2,3-FFPTB demonstrates a sharp and well defined peak at $2\theta = 3.44^\circ$, corresponding to a lattice constant of 25.95 Å. This confirms that the as-spun 2,3-FFPTB film is crystalline and shows already some degree of molecular ordering without further process. When the film is heated up to 80 °C (just below crystalline \rightarrow smectic I), to 105 °C (transition crystalline \rightarrow smectic I) and to 110 °C (in Smectic I), this peak appears slightly shifted to lower diffraction angle at $2\theta = 3.36^\circ$ (lattice spacing of 26.30 Å). This corresponds to an increase in lattice spacing from 25.95 Å to 26.30 Å. Also, from 80 °C to 110 °C in the first smectic phase, the relative intensity of the peak drops considerably (see Figure 4.20-a)). At 116 °C, the transition smectic I \rightarrow smectic II appears, and this peak shifts back consequently from $2\theta = 3.36^\circ$ to $2\theta = 2.81^\circ$ corresponding to an increase in lattice spacing from 26.30 Å to 31.42 Å. This change in mesophase significantly affects the molecular arrangement in the crystal structure of 2,3-FFPTB as demonstrate here with a subsequent increase in lattice spacing. This second smectic phase persists up to 130 °C just below the transition smectic II \rightarrow isotropic, where a reflection is observed at the relative same position of $2\theta = 2.83^\circ$ (lattice constant of 31.21 Å). Relative intensities in this second smectic phase are reduced compared to those in the first smectic phase, as clearly shown in Figure 4.20-a). For clarity, a zoom-in on the peaks observed at 116 °C and 130 °C during heating is shown in Figure 4.22). From 141 °C, no peaks associated with crystalline structure are observed, indicating that the film is already in the isotropic phase at this temperature.

During cooling, again no peak associated with the crystalline structure is observed from 160 °C to 141 °C, but when the smectic (II) phase is reached (130 °C), a weak peak appears at $2\theta = 2.77^\circ$. The peak is at the same position as during heating, but with a higher relative intensity (Figure 4.20-b)). This peak remains at this same position till 105 °C ($2\theta = 2.76^\circ$), indicating that during cooling, the film still in second smectic phase at 105 °C. At 80 °C during cooling, the peak shift back to $2\theta = 3.37^\circ$ indicating that the film is now in the crystalline phase again. This gives indication of a single smectic phase during cooling, while two smectic phases have been observed during heating. When the film is cooled back to room temperature, the peak is found at the relative same position as before heating ($2\theta = 3.43^\circ$) with almost the same relative intensity (see Figure 4.20-b)). This indicates that, the film cooled back to room temperature show similar crystalline structure as the as-spun film.

Overall, the 2,3-FFPTB film at 80 °C show the highest relative peak intensity both during heating and cooling cycle. Additionally a narrowing of the peak during heating is generally observed (from $FWHM = 0.115^\circ$ as spun, to $FWHM = 0.063^\circ$ at 130 °C).

These results demonstrated increased long range molecular ordering in 2,3-FFPTB, as well as shifts in the crystal structure achieved upon annealing. Thermal treatment (heating/cooling) is observed to induce a narrower XRD peak with increased intensity, consistent with improve long range molecular order in films.

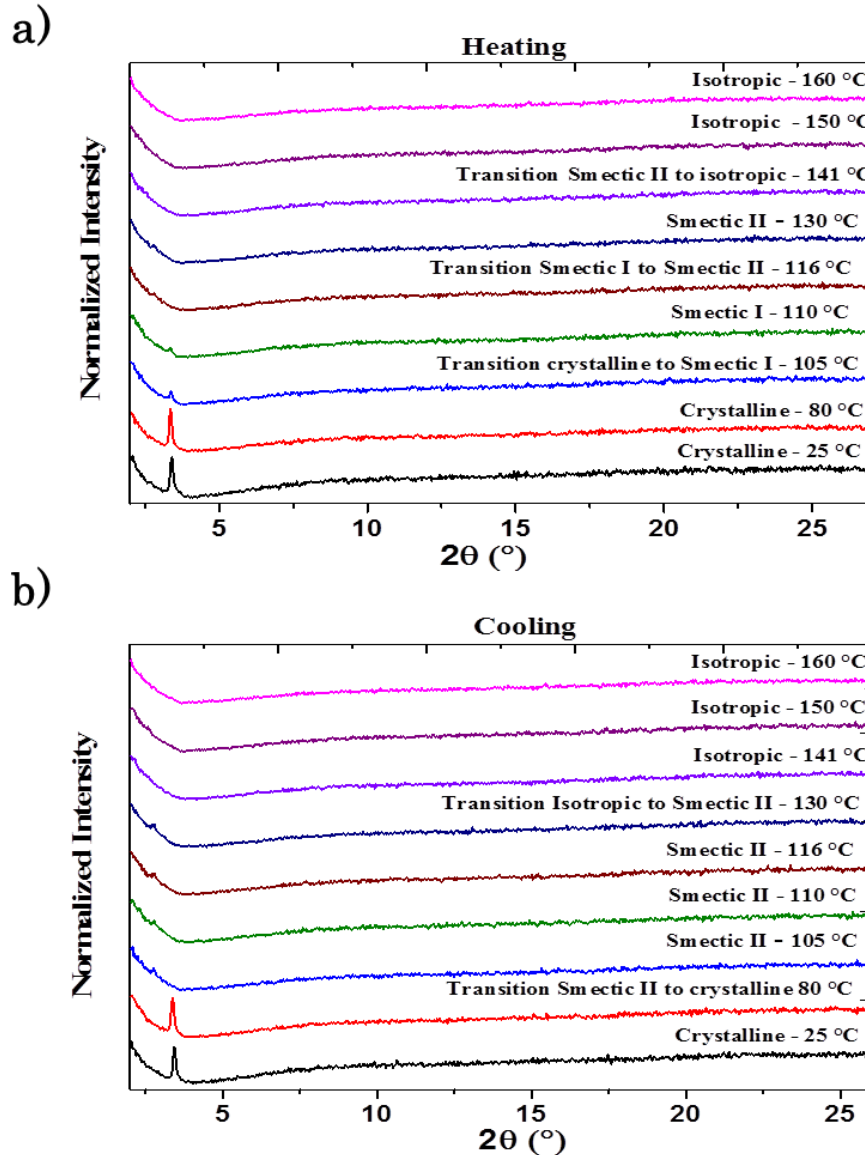


Figure 4.20: In-situ XRD patterns of an 2,3-FFPTB film taken during a) heating and b) cooling.

- **2,6-FFPTB**

During the heating cycle of 2,6-FFPTB (Figure 4.21-a)), the as-spun film exhibits a weak and broad peak at $2\theta = 4.59^{\circ}$ corresponding to a lattice spacing of 19.25 \AA . This is consistent with the fact that 2,6-FFPTB film is crystalline at room temperature. When the film is heated up to 60°C , 100°C and 120°C , this peak appears gradually shifted back to lower diffraction angles (60°C , $2\theta = 4.56^{\circ}$; 100°C , $2\theta = 4.47^{\circ}$ and 120°C , $2\theta = 4.46^{\circ}$), corresponding to a gradual increase in lattice spacing (60°C , $d = 19.38 \text{ \AA}$; 100°C , $d = 19.77 \text{ \AA}$ and 120°C , $d = 19.81 \text{ \AA}$) as shown in Figure 4.21-a). The relative intensity of the peak increases with

temperature and is more prominent and narrower at 100 °C. At temperatures of 131 °C and above, no peaks associated with crystalline structure are observed, indicating that the film turns to an isotropic melt at this temperature.

During the cooling cycle for patterns taken between 160 °C and 120 °C (Figure 4.21-b) no peaks associated with the crystal structure is observed. This indicates that the film is still in the isotropic phase at 120 °C during cooling. The peak associated with the crystal structure starts emerging at 100 °C ($2\theta = 4.45^\circ$), but with reduced relative intensity compared to the heating cycle. At 60 °C, this peak slightly shifts from $2\theta = 4.45^\circ$ to $2\theta = 4.53^\circ$ corresponding to a decrease of lattice constant from 19.86 Å to 19.46 Å. When the film is cooled down to room temperature, the peak is shifted back to $2\theta = 4.61^\circ$ (lattice spacing of 19.17 Å) but with a higher intensity compared to the as-spun film before heating as shown in Figure 4.21-b). This indicates that, the film cooled back to room temperature is more ordered than the as-spun film.

Overall, at 100 °C the film shows an XRD diffraction peak with the highest relative intensity both during heating and cooling cycle. It is observed generally a narrowing of the peak during heating (from $FWHM = 0.176^\circ$ as spun, to $FWHM = 0.091^\circ$ at 120°C). However, the peak broadens during cooling, from $FWHM = 0.086^\circ$ at 100°C to $FWHM = 0.101^\circ$ at room temperature. These results indicate the formation of highly ordered 2,6-FFPTB films upon annealing.

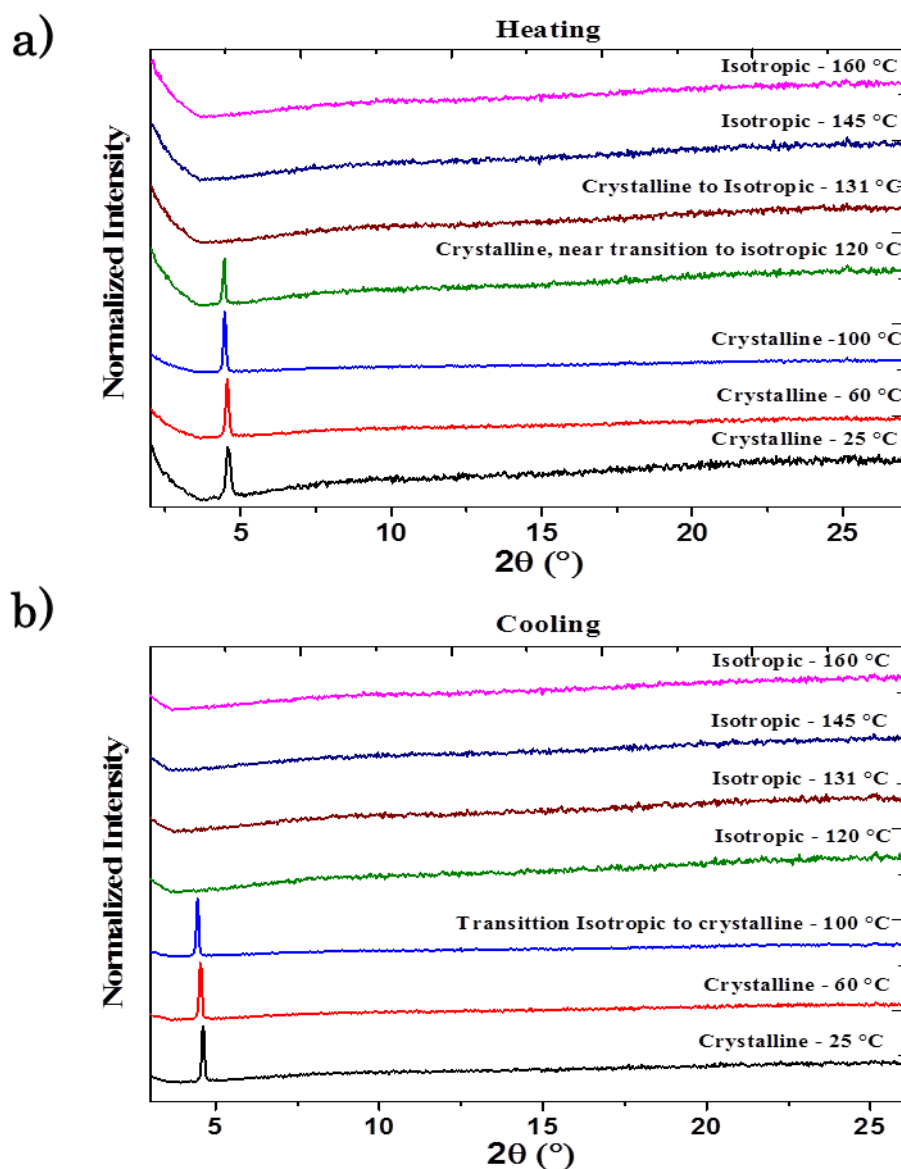


Figure 4.21: In-situ XRD patterns of an 2,6-FFPTB film taken during a) heating and b) cooling.

For both 2,3-FFPTB and 2,6-FFPTB, the in-situ characterization demonstrates that the film crystallinity improves upon annealing and cooling. The peak's narrowing and broadening observed in both cases, suggest shifting of molecules in the unit cell of 2,3-FFPTB and 2,6-FFPTB relative to nearest neighbors. Table 4.3 summarizes the in-situ XRD parameters of 2,3-FFPTB and 2,6-FFPTB.

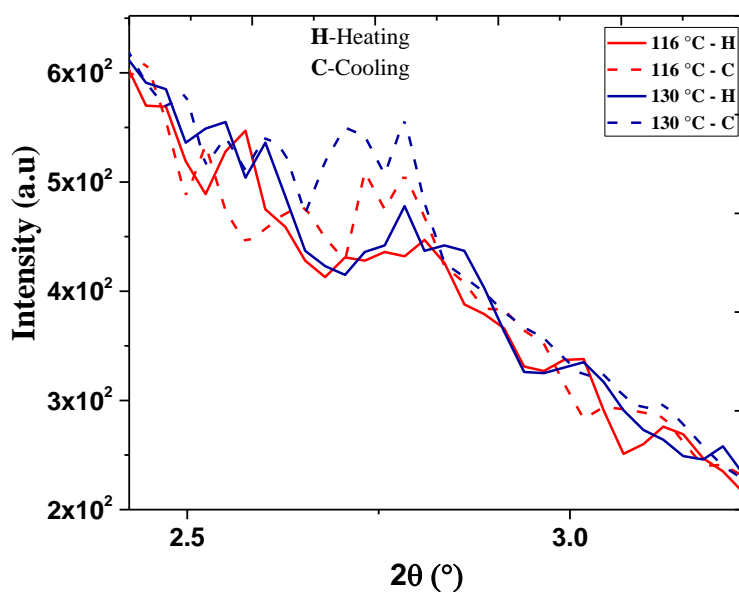


Figure 4.22: Zoom-in In-situ XRD patterns of an 2,3-FFPTB film taken during heating and cooling at 116 °C and 130 °C.

Table 4.3: 2θ , d – spacing and $FWHM$ values of 2,3-FFPTB and 2,6-FFPTB at in-situ measurement during heating and cooling cycle.

		Heating			Cooling		
Molecules	Temperature (°C)	2θ (°)	d -spacing(Å)	$FWHM$ (°)	2θ (°)	d -spacing(Å)	$FWHM$ (°)
2,3-FFPTB	25	3.44	25.95	0.115	3.43	25.70	0.107
	80	3.36	26.30	0.108	3.37	26.10	0.113
	105	3.36	26.30	0.083	2.76	31.99	0.102
	110	3.36	26.30	0.084	2.79	31.60	0.099
	116	2.81	31.42	0.084	2.78	31.73	0.099
	130	2.83	31.67	0.063	2.77	31.83	0.133
2,6-FFPTB	25	4.59	19.25	0.176	4.61	19.17	0.101
	60	4.56	19.38	0.121	4.54	19.46	0.105
	100	4.47	19.77	0.102	4.45	19.86	0.086
	120	4.46	19.81	0.091	–	–	–

XRD patterns from annealed FFPTB films

As the next step, the influence of annealing through the mesophases on the crystal structure of the FFPTB films at room temperature was investigated. The XRD patterns of annealed films were characterized. FFPTB films were annealed at temperatures corresponding to the

transition between the mesophases (120 °C and 160 °C for 2,6-FFPTB ; 80 °C, 105 °C, 120 °C and 160 °C for 2,3-FFPTB), and subsequently cooled down to room temperature before measurement.

The normalized pattern of as-spun 2,3-FFPTB (black), annealed at 80 °C (red), 105 °C (blue), 120 °C (green) and 160 °C (wine) is shown in Figure 4.23. Figure 4.24-a) shows the zoom-in on first order reflection centered at $2\theta \sim 3.35^\circ$. For the as-spun film, a very prominent peak is observed at $2\theta = 3.33^\circ$, corresponding to the lattice spacing of 26.5 Å consistent with the peak observed also in Figure 4.20-a). Additionally, in the low angle region ($2\theta < 10^\circ$), the second order reflection is observed at $2\theta = 6.65^\circ$ (lattice spacing of 13.21 Å), weaker in intensity compared to the first peak (Figure 4.24-c)). This confirms that the as-spun 2,3-FFPTB film is crystalline. When the film is annealed up to 80 °C, just near the transition from crystalline → smectic I, the same peaks present in the as-spun film are observed but with higher relative intensities and slightly shifted ($2\theta = 3.36^\circ$ and $2\theta = 6.74^\circ$) corresponding to a slight decrease in lattice spacing. When the film was annealed at 105 °C in the first smectic phase, the peaks become more prominent and increase to $2\theta = 3.39^\circ$ and $2\theta = 6.80^\circ$ corresponding to a decrease of lattice spacing. At 120 °C, the peaks increase further to $2\theta = 3.42^\circ$ and $2\theta = 6.87^\circ$ and the relative intensity is reduced. In the annealed film at 160 °C in the isotropic phase, the peaks are observed at $2\theta = 3.39^\circ$ and $2\theta = 6.83^\circ$ corresponding to lattice constants of 26.06 Å and 12.92 Å. The peaks at this temperature show the lowest relative intensity for all temperatures, but also the narrowest peaks (see Figure 4.24 & Table 4.4). 105 °C pattern yields the broadest peak with the highest relative intensity.

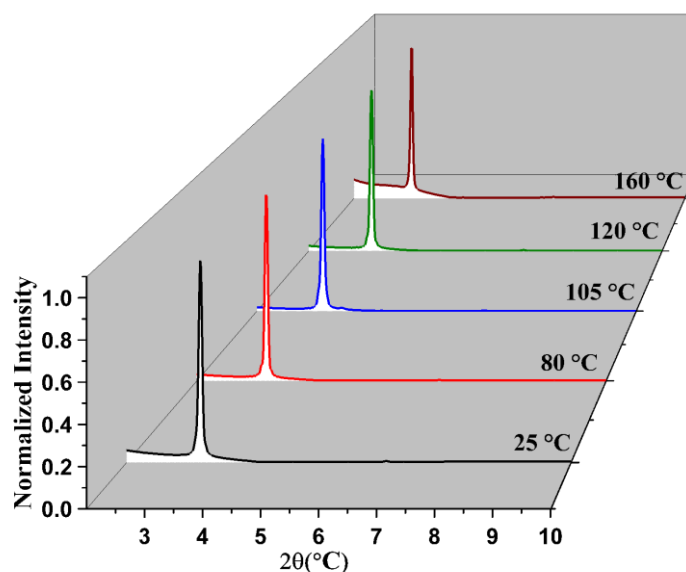


Figure 4.23: Normalized XRD patterns of as-spun 2,3-FFPTB (black), and 2,3-FFPTB films annealed at 80 °C (red), 105 °C (blue), 120 °C (green) and 160 °C (wine).

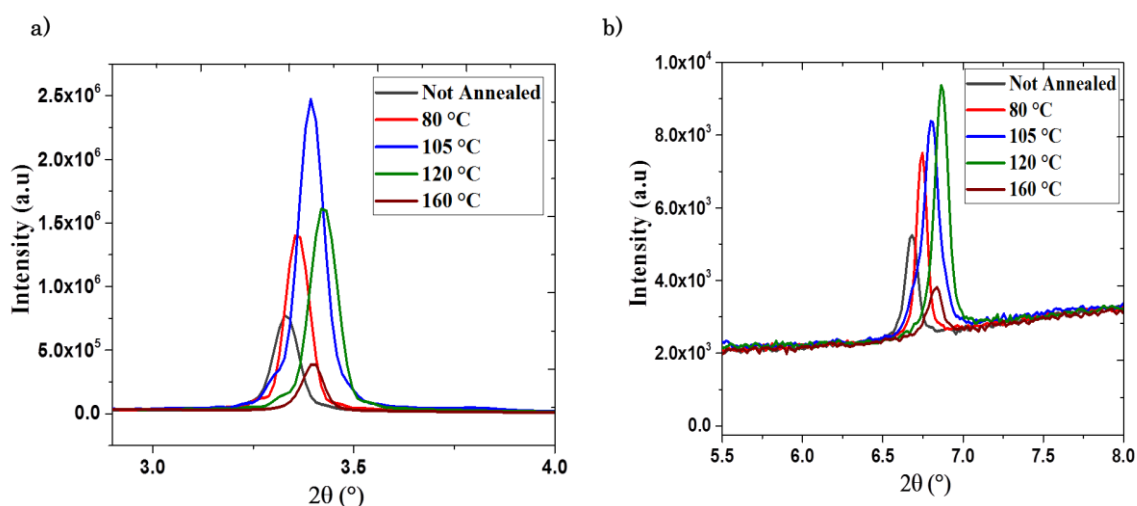


Figure 4.24: Zoom-in normalized XRD patterns of 2,3-FFPTB a) zoom into 1st order reflection at $2\theta \sim 3.35^\circ$ c) zoom into the second order reflection at $2\theta \sim 6.7^\circ$.

Figure 4.25 shows the normalized XRD pattern of 2,6-FFPTB films as-spun (blue), annealed at 120 °C (red) and 160 °C (blue), while Figure 4.26-a) depicts the zoom-in on the first order reflection centered at $2\theta \sim 4.58^\circ$. The pattern taken from the as-spun film yields a very prominent peak at $2\theta = 4.58^\circ$ (lattice spacing of 19.25 Å), consistent with the prominent peak observed during in-situ measurement (Figure 4.21-a). When the film is annealed to 120 °C (just below the transition crystalline \rightarrow isotropic), two more reflections weaker in intensity

appear respectively at $2\theta = 6.27^\circ$ and $2\theta = 9.20^\circ$ corresponding to lattice spacing of 14.07 \AA and 9.60 \AA (Figure 4.26-b)). The peak at $2\theta = 9.20^\circ$ corresponds to the second order of the most prominent peak observed at $2\theta = 4.58^\circ$. This indicates that cooling from a specific mesophase back to room temperature induces the formation of highly ordered layers and increases long range molecular ordering in 2,6-FFPTB films. This result also suggests that cooling from 120°C , near to transition crystalline \rightarrow isotropic phase, helps to achieved more ordered phases of the material. In the film annealed at 160°C , the pattern is similar to that of the as-spun film, with a slight shift in the peak which appears at $2\theta = 4.56^\circ$, corresponding to a slight increase in lattice spacing. The relative intensity of peaks at 160°C also decreases significantly, and is lower compared to the as-spun film. 2,6-FFPTB are very crystalline, and the films annealed at 120°C demonstrate the most prominent and narrow peaks overall (see Table 4.4).

Overall, Steady-state XRD confirms the significant difference in molecular packing among both molecules as observed in the in-situ measurement.

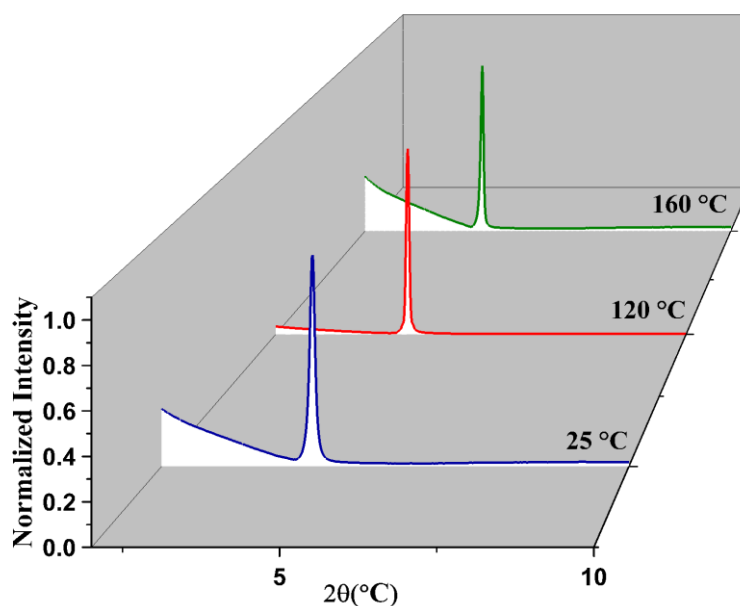


Figure 4.25: Normalized XRD patterns of as-spun 2,6-FFPTB (blue), and 2,6-FFPTB films annealed at 120°C (red) and 160°C (green).

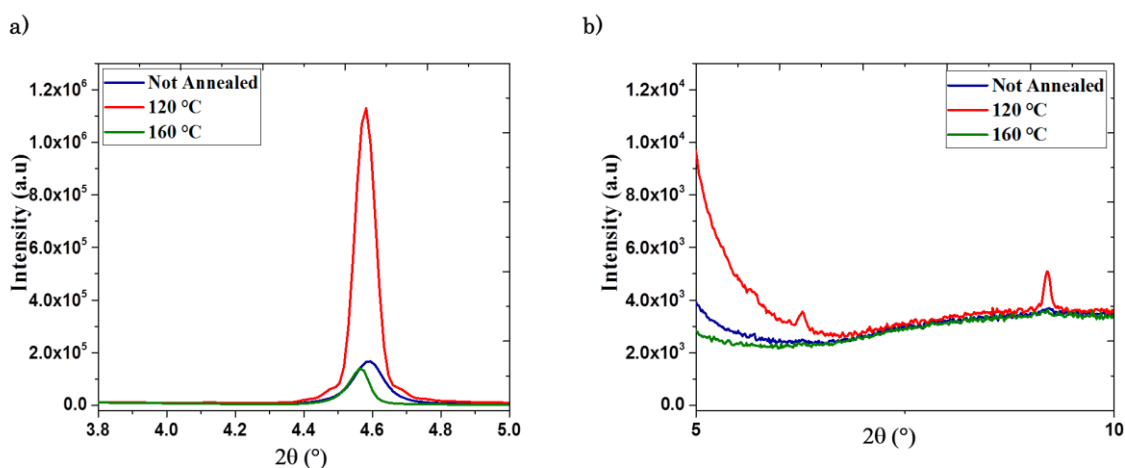


Figure 4.26: Zoom-in normalized XRD patterns of 2,6-FFPTB **a)** 1st order reflection at $2\theta \sim 4.5^\circ$ **b)** zoom into the reflections at $2\theta \sim 6.7^\circ$, $2\theta \sim 9.20^\circ$ (second order reflection).

Table 4.4: 2θ and *FWHM* values of 2,3-FFPTB and 2,6-FFPTB for Steady-state measurement.

Molecules	Temperature ($^\circ\text{C}$)	2θ ($^\circ$)			FWHM		
		1 st peak	2 nd peak	3 rd peak	1 st peak	2 nd peak	3 rd peak
2,3-FFPTB	25	3.33	6.65	-	0.074	0.083	-
	80	3.36	6.74	-	0.070	0.075	-
	105	3.39	6.80	-	0.075	0.104	-
	120	3.42	6.87	-	0.080	0.0907	-
	160	3.39	6.83	-	0.063	0.101	-
2,6-FFPTB	25	4.58	-	-	0.104	-	-
	120	4.57	6.27	9.20	0.071	0.081	0.122
	160	4.56	-	-	0.071	-	-

Steady state polarization optical microscopy (POM)

The effect of cooling on films was also checked using polarization microscopy. Figure 4.27 shows the polarized optical microscopy images taken from the as-spun film of 2,3-FFPTB, and the films annealed at 80 $^\circ\text{C}$, 105 $^\circ\text{C}$, 120 $^\circ\text{C}$ and 160 $^\circ\text{C}$. And Figure 4.28 shows those taken from the as-spun film of 2,6-FFPTB, and films annealed at 120 $^\circ\text{C}$ and 160 $^\circ\text{C}$.

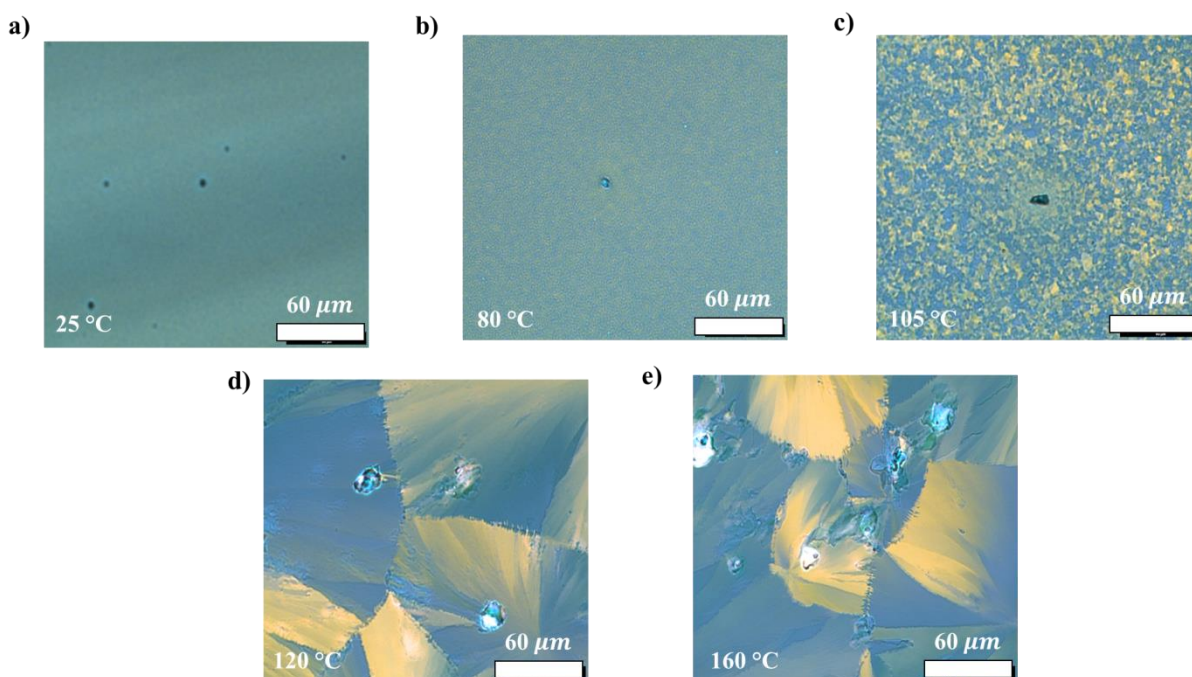


Figure 4.27: Cross-polarized optical microscopy images of **a)** as-spun 2,3-FFPTB and 2,3-FFPTB films annealed at **b)** 80 °C, **c)** 105 °C, **d)** 120 °C and **e)** 160 °C

For 2,3-FFPTB, gradual increase of birefringence in the films is observed, indicating highly ordered domains which increase upon annealing (Figure 4.27). As expected from cooling through different ordered smectic phases, very high crystalline films were obtained. The structural integrity is high even for films that were cooled from the isotropic melt (160 °C).

The same observation is done with 2,6-FFPTB films, which are all crystalline and the size of the crystal domains increases with annealing temperature as seen in Figure 4.28. Despite the lack of a smectic phase for 2,6-FFPTB, an excellent film coverage is observed (Figure 4.28) and also the structural integrity of the film is also conserved even at higher temperatures. For both molecules, cooling from higher temperatures resulted in large ordered domains in the POM images.

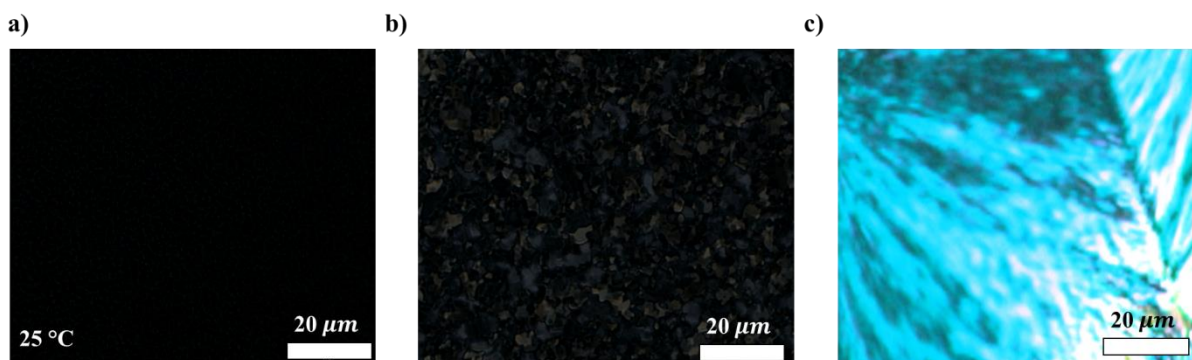


Figure 4.28: Cross-polarized optical microscopy images of a) as-spun 2,6-FFPTB and 2,6-FFPTB films annealed at b) 120 °C and c) 160 °C

4.2.4. Electrical properties: Investigation of Ambipolarity in 2,3-FFPTB and 2,6-FFPTB dyes

The ambipolar transport properties of the materials were investigated by preparing and measuring “hole-only” and “electron-only” diodes. Device architectures and energy band diagrams are given in Figure 4.29.

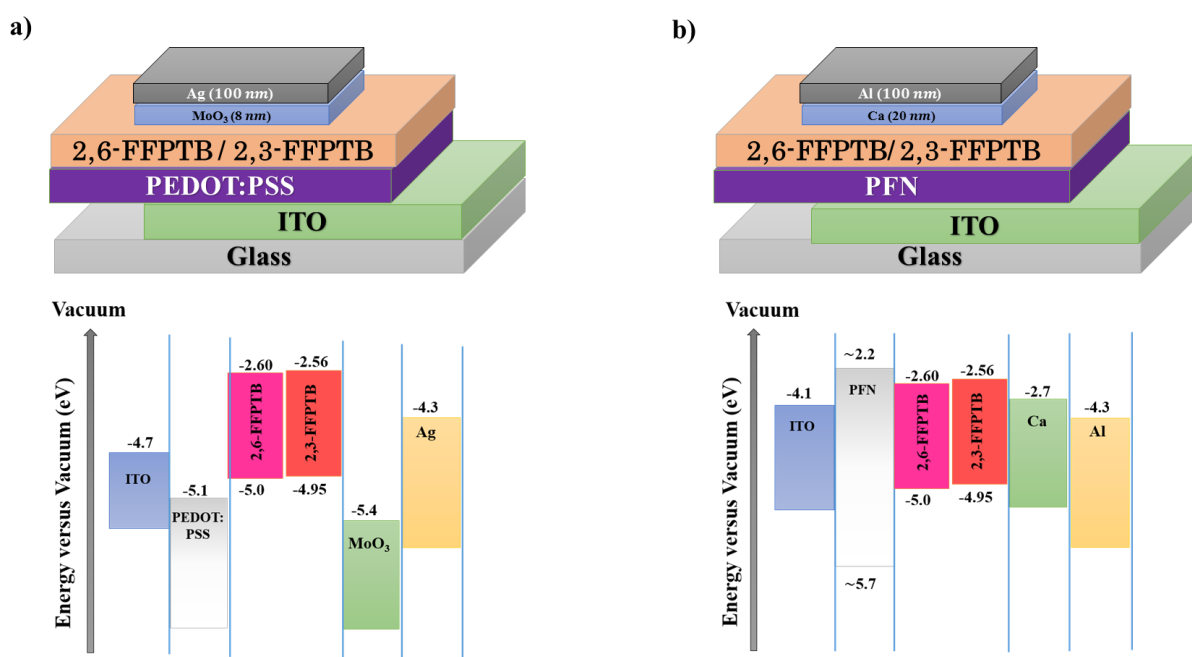


Figure 4.29: Schematic sketch of 2,6-FFPTB & 2,3-FFPTB a) hole-only device b) electron-only device, together with the band diagrams. **N.B:** As proved from the literature ^[108-109], the PFN modifies the work function of ITO by lowering its value for about 0.6 eV.

Hole mobility

Figure 4.30 shows the current density-voltage (JV) characteristics for diodes prepared with 2,3-FFPTB (Figure 4.30-a)) and 2,6-FFPTB (Figure 4.30-b)). For both molecules, annealed films show higher current density than in as-spun films, and current density increases with increasing annealing temperature. For diodes prepared with 2,3-FFPTB, films annealed at 80 °C (crystalline phase) and 105 °C (first smectic phase) demonstrate very similar JV characteristics, while films annealed at 160 °C in the isotropic phase for both, show the highest current density of all samples.

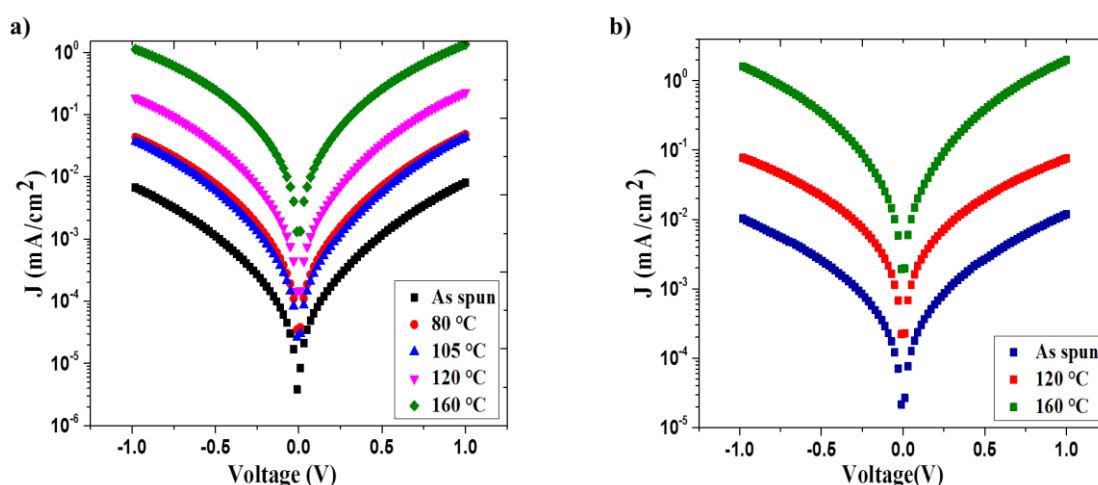


Figure 4.30: Current density-voltage (JV) characteristics for diodes prepared with **a)** as-spun 2,3-FFPTB films (black squares) and 2,3-FFPTB films annealed at 80 °C (red squares), 105 °C (blue squares), 120 °C (pink squares) and 160 °C (green squares); **b)** as-spun 2,6-FFPTB films (blue squares) and 2,6-FFPTB films annealed at 120 °C (red squares) and 160 °C (green squares)

Carrier mobilities were estimated using SCLC theory. The average hole mobility (μ_p) of 2,3-FFPTB devices measured as spun exhibit an average value of $(4.7 \pm 0.3) \times 10^{-7} \text{ cm}^2\text{V}^{-1}\text{s}^{-1}$, which value increases of one order of magnitude upon annealing through 80 °C, 105 °C, 120 °C, until it reaches $(9.5 \pm 0.9) \times 10^{-6} \text{ cm}^2\text{V}^{-1}\text{s}^{-1}$ in films annealed at 120 °C. Films annealed at 80 °C and 105 °C show the same order of mobilities ($(2.3 \pm 0.3) \times 10^{-6} \text{ cm}^2\text{V}^{-1}\text{s}^{-1}$ and $(3.3 \pm 0.3) \times 10^{-6} \text{ cm}^2\text{V}^{-1}\text{s}^{-1}$) as expected from the J-V characteristics (Figure 4.30-a)). When the films were annealed at 160 °C, the average hole mobility drastically increases to reach $(2.3 \pm 0.3) \times 10^{-4} \text{ cm}^2\text{V}^{-1}\text{s}^{-1}$. For 2,6-FFPTB, hole mobilities for the devices measured as spun exhibits an average value of

$(5.1 \pm 0.3) \times 10^{-6} \text{ cm}^2\text{V}^{-1}\text{s}^{-1}$, and increases upon annealing at 120 °C by one order of magnitude to reach $(4.5 \pm 0.3) \times 10^{-5} \text{ cm}^2\text{V}^{-1}\text{s}^{-1}$. When the film was annealed at 160 °C, this value increases even higher to the high value of $(6.1 \pm 0.3) \times 10^{-4} \text{ cm}^2\text{V}^{-1}\text{s}^{-1}$.

Generally in both materials, hole mobility increases over two orders of magnitude (2,6-FFPTB) and three orders magnitude (2,3-FFPTB) upon annealing. .

2,3-FFPTB show the most significant increase in hole mobility from $(4.7 \pm 0.3) \times 10^{-7} \text{ cm}^2\text{V}^{-1}\text{s}^{-1}$ in as-spun films to $(2.3 \pm 0.3) \times 10^{-4} \text{ cm}^2\text{V}^{-1}\text{s}^{-1}$ after annealing at 160°C. This is attributed to cooling through ordered smectic phases, which highly increase crystallinity in LC films [8, 15]. Interestingly 2,6-FFPTB which has no smectic phase, demonstrates overall higher hole mobility (Figure 4.31).

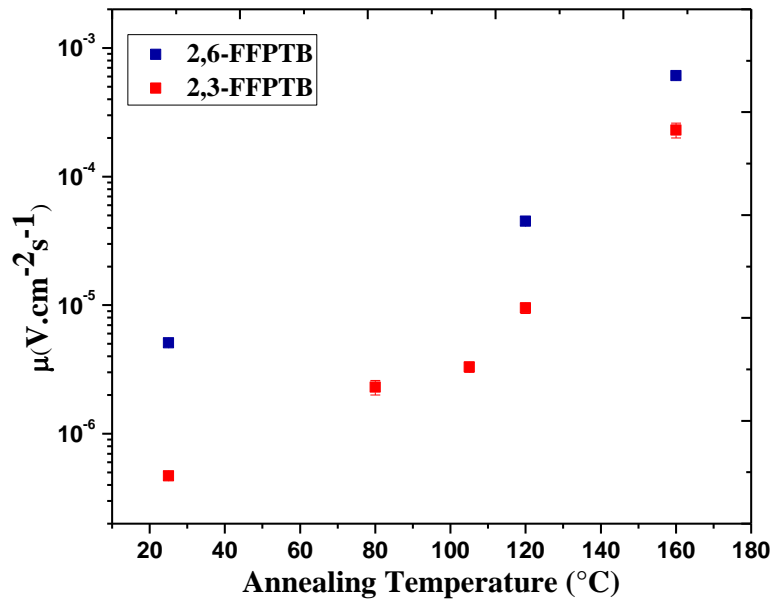


Figure 4.31: Comparison of hole mobility versus annealing temperature in 2,6-FFPTB and 2,3-FFPTB.

Electron mobility

Current density-voltage (JV) characteristics for electron only diodes prepared with 2,3-FFPTB and 2,6-FFPTB are shown in Figure 4.32-a) and b), respectively. For 2,3-FFPTB, the current density increases with annealing temperature in general, and this increase is significant in diodes prepared with 2,3-FFPTB films annealed at 105 °C, 120 °C and 160 °C in the smectic phase and isotropic melt. For diodes prepared with 2,6-FFPTB, as-spun films and films annealed at 120 °C (crystalline phase) demonstrate very similar JV characteristics, with only a slight increase of current density with annealing. But the current density highly increases when films were annealed at 160 °C.

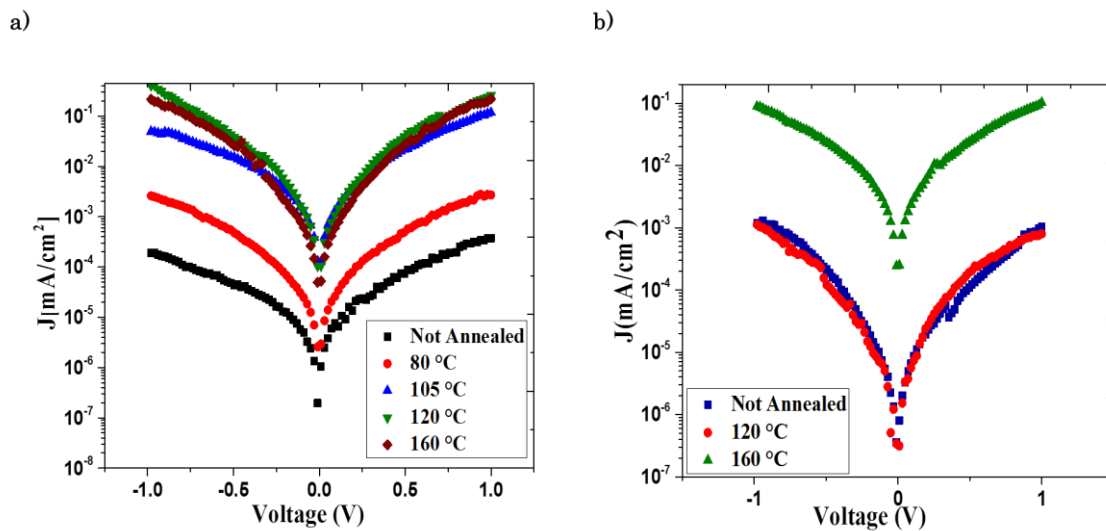


Figure 4.32: Current density-voltage (JV) characteristics for electron-only diodes prepared with **a)** as-spun 2,3-FFPTB films (black squares) and 2,3-FFPTB films annealed at 80 °C (red circles), 105 °C (blue triangles), 120 °C (green triangles) and 160 °C (wine stars); **b)** as-spun 2,6-FFPTB films (blue squares) and 2,6-FFPTB films annealed at 120 °C (red circles) and 160 °C (green triangle).

Electron mobility (μ_n) for 2,3-FFPTB devices measured as spun show relatively low average mobility values of $(5.7 \pm 0.6) \times 10^{-8} \text{cm}^2 \text{V}^{-1} \text{s}^{-1}$. After annealing at 80 °C, this mobility increases of one order to reach the value of $(3.3 \pm 0.3) \times 10^{-7} \text{cm}^2 \text{V}^{-1} \text{s}^{-1}$. When the films were annealed at 105 °C in the smectic I phase, the electron mobility in 2,3-FFPTB drastically increases by three orders of magnitude to $(1.6 \pm 0.2) \times 10^{-5} \text{cm}^2 \text{V}^{-1} \text{s}^{-1}$, and remains in the same range upon annealing at 120 °C in the second smectic phase ($(1.8 \pm 0.2) \times 10^{-5} \text{cm}^2 \text{V}^{-1} \text{s}^{-1}$), and 160 °C ($(1.2 \pm 0.2) \times 10^{-5} \text{cm}^2 \text{V}^{-1} \text{s}^{-1}$) in the isotropic phase. This

result indicates that cooling through ordered smectic phase of the material, help to drastically improve electron transport in 2,3-FFPTB.

In comparison with hole mobility, these results demonstrate that in 2,3-FFPTB crystalline films (as-spun films, annealed at 80 °C), as well as in film annealed at 160 °C, electron mobility is clearly limited compared to hole mobility as shown in Figure 4.34. However, if the films are cooled from smectic phases of 2,3-FFPTB, the electron mobility increases by one order of magnitude higher than hole mobility, as the results confirm: At 105 °C ($\mu_n = (1.6 \pm 0.2) \times 10^{-5} \text{cm}^2 \text{V}^{-1} \text{s}^{-1} > \mu_p = (3.3 \pm 0.3) \times 10^{-6} \text{cm}^2 \text{V}^{-1} \text{s}^{-1}$) and 120 °C ($\mu_n = (1.8 \pm 0.2) \times 10^{-5} \text{cm}^2 \text{V}^{-1} \text{s}^{-1} > \mu_p = (9.5 \pm 0.9) \times 10^{-6} \text{cm}^2 \text{V}^{-1} \text{s}^{-1}$).

These results indicate that electron transport in 2,3-FFPTB appears clearly dominant in the smectic phases, while hole mobility in the crystalline and isotropic phase is dominant. This interesting result clearly established that beside the very good hole transport demonstrated in 2,3-FFPTB, a good electron transport is also achieved, favoured by the presence of smectic phases. It indicates that slight changes in molecular ordering induced by annealing through the different mesophases can influence electron and hole mobility differently.

Measured electron mobilities for the as-spun 2,6-FFPTB devices, exhibit an average value of $(2.0 \pm 0.2) \times 10^{-7} \text{cm}^2 \text{V}^{-1} \text{s}^{-1}$. 2,6-FFPTB films annealed at 120 °C just below the phase transition crystalline \rightarrow isotropic phase, exhibit the same order of mobility with the average value of $(2.6 \pm 0.2) \times 10^{-7} \text{cm}^2 \text{V}^{-1} \text{s}^{-1}$. This value increases significantly to reach average value of $(8.0 \pm 0.5) \times 10^{-6} \text{cm}^2 \text{V}^{-1} \text{s}^{-1}$ upon annealing at 160 °C.

In comparison with hole mobilities (μ_p) obtained with 2,6-FFPTB, these values are generally two order of magnitude smaller (see Figure 4.34). These results demonstrate that electron transport in 2,6-FFPTB though measurable is limited.

Figure 4.33 which depicts the comparison of electron mobility between 2,3-FFPTB and 2,6-FFPTB shows that 2,3-FFPTB is a much better electron transporting material compared to 2,6-FFPTB.

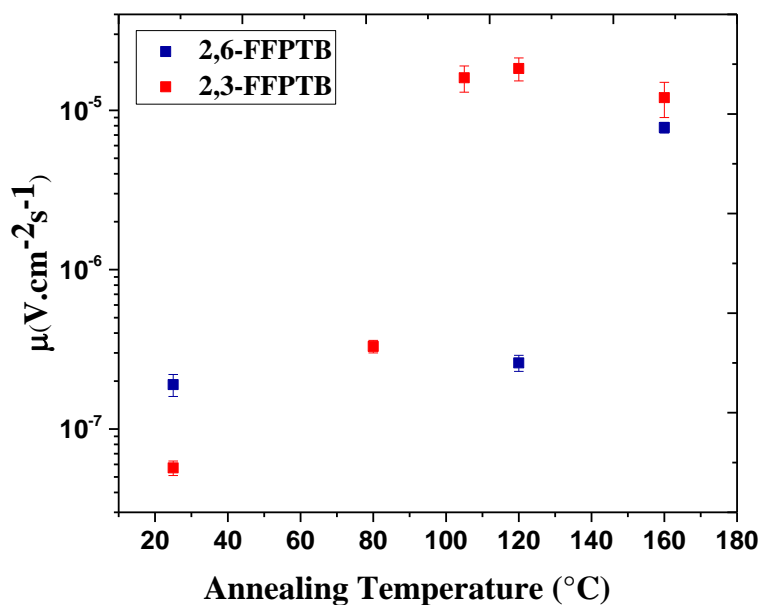


Figure 4.33: Comparison of electron mobility versus annealing temperature in 2,3-FFPTB and 2,6-FFPTB.

A Comparison of electron and hole mobilities in 2,3-FFPTB and 2,6-FFPTB is given in Figure 4.34.

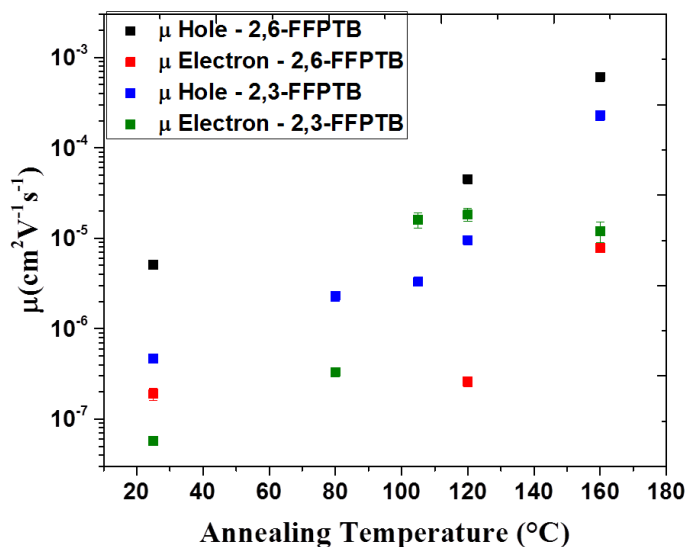


Figure 4.34: Electron and hole mobility versus annealing temperature in 2,3-FFPTB and 2,6-FFPTB.

Discussions

2,3-FFPTB exhibited increased hole and electron transport after annealing (Figure 4.34). This large increase in charge carrier transport after annealing the 2,3-FFPTB through the smectic phases is consistent with the literature, as increased molecular ordering favours smaller positional and energetic disorder^[123, 124]. Interestingly, this molecule also demonstrates good electron transport. In this material, a clear influence of molecular alignment on molecular transport is observed and the results demonstrate an high ambipolar transport in 2,3-FFPTB. This is confirmed by the highest values of mobility achieved from annealing in the isotropic melt for hole transport, and in the smectic phase for electron transport, which are respectively $(2.3 \pm 0.3) \times 10^{-4} \text{ cm}^2\text{V}^{-1}\text{s}^{-1}$ and $(1.8 \pm 0.2) \times 10^{-5} \text{ cm}^2\text{V}^{-1}\text{s}^{-1}$.

These results also demonstrated that the electron and hole transport show different dependence on annealing in 2,3 FFPTB. This indicates that the interplay between molecular aggregation on the short length scale and molecular order on a longer scale can be tuned to control transport. The HOMO and LUMO geometries of the molecules show that the HOMO is delocalised over the molecule while the LUMO is localised on the central acceptor unit. This implies that slight variations in electronic coupling between the molecules will influence hole and electron transfer rates in different ways. This was confirmed by the variation observed in electron and hole mobilities for each molecule (see Figure 4.34). Moreover, in the case of 2,3-FFPTB, the smectic phase leads to a larger dependence of transport on annealing (see Figure 4.34).

In 2,6-FFPTB ambipolar transport is also observed as confirmed by a hole mobilities of $(6.1 \pm 0.3) \times 10^{-4} \text{ cm}^2\text{V}^{-1}\text{s}^{-1}$ after annealing at 160 °C and electron mobilities of $(8.0 \pm 0.5) \times 10^{-6} \text{ cm}^2\text{V}^{-1}\text{s}^{-1}$ upon annealing at 160 °C. Interestingly, although 2,3 FFPTB has two smectic phases, and 2,6 FFPTB does not demonstrate a mesophase, the hole mobility values in 2,6 FFPTB are higher. This indicates that molecular alignment in film relative to the electrodes may not be favourable for transport.

Summary

The electrical transport in two LC dyes which varied only in the position of the fluorine substitution was investigated. 2,3-FFPTB possesses two smectic phases while 2,6-FFPTB

exhibits no mesophase. Cooling from different smectic phase for 2,3-FFPTB resulted in highly ordered films and reduced structural defects in films. For 2,6-FFPTB, highly ordered films were also achieved from cooling in the isotropic melt and both materials show an excellent film coverage even after cooling from temperature as high as 160 °C. XRD studies confirmed a significant difference in molecular packing on films, consistent with the slight variations in the electron density on the molecular backbone induced by variation in the position of the fluorine substitution. This lead to significant variation in charge carrier mobilities in diodes. Hole mobility in the order of $(6.1 \pm 0.3) \times 10^{-4} \text{ cm}^2\text{V}^{-1}\text{s}^{-1}$ in 2,6-FFPTB and $(2.3 \pm 0.3) \times 10^{-4} \text{ cm}^2\text{V}^{-1}\text{s}^{-1}$ in 2,3-FFPTB ; and electron mobility in the order of $(1.8 \pm 0.2) \times 10^{-5} \text{ cm}^2\text{V}^{-1}\text{s}^{-1}$ in 2,3-FFPTB and $(8 \pm 0.5) \times 10^{-6} \text{ cm}^2\text{V}^{-1}\text{s}^{-1}$ in 2,6-FFPTB could be achieved, confirming efficient ambipolar charge carrier transport in these novel LC dyes. The results demonstrate that systematic molecular design of LC semiconductors can be applied to tune electron and hole transport independently.

4.3. Comparison of the charge carrier transport in novels liquid crystal dyes 2,3-FPPTB and 2,6-FPPTB with a study case of novel n-type conducting polymers

The electron and hole transport in the novels liquid crystal dyes 2,3-FPPTB and 2,6-FPPTB being established, a comparison with a study case of their polymeric counterparts appeared necessary to shed more light in the potential of these materials for future electronic applications. During the last decades, building blocks based on conjugated polymers have been tailored for applications in organic electronic devices. In this section, the carrier mobility in two new highly head-to-tail regioregular polythiazoles (rr-PTzs) bearing trialkylsilyloxy-methyl-side-chains (PTzTHX, PTzTNB) synthesized by Dr. Frank Pammer at the University of Ulm, is studied. Dr. Pammer's group performed the synthesis, electronic and bulk-morphology studies, while I investigated charge transport properties in these novel conducting polymers.

4.3.1. Molecular structure of the polymers

Molecular structures of PTzTHX and PTzTNB are given in Figure 4.35 below.

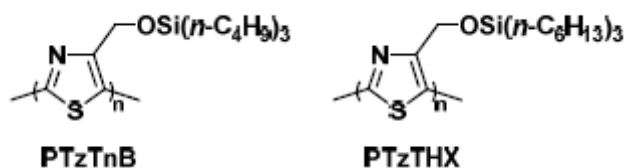


Figure 4.35: Molecular structures of PTzTNB and PTzTHX.

PTzTNB and PTzTHX with different molecular weights were obtained from synthesis, detailed as PTzTNB₈₄ (Mn = 84.3 kDa, PDI = 2.48) and PTzTNB₁₄ (Mn = 14.1 kDa, PDI = 2.13) for PTzTNB, as well as PTzTHX₆₀ (Mn = 59.8 kDa, PDI = 1.70), PTzTHX₄₀ (Mn = 39.5 kDa, PDI = 2.07), and PTzTHX₂₀ (Mn = 20.0 kDa, PDI = 2.34), for PTzTHX. For the electrical characterizations discussed in this work, only PTzTNB₈₄, PTzTHX₄₀, and PTzTHX₆₀ were studied. The polymers exhibit very similar optical and electronic properties, in agreement with the isoelectronic nature of their respective conjugated system.

4.3.2. Electrical characterization of PTzTHX and PTzTNB

Structural order and a high degree of crystallinity are generally considered favorable for charge transport in semi-conducting polymers.^[125] The investigation of structural and optical properties of PTzTHX and PTzTNB as well as their molecular packing on films, indicated that these may be suitable candidates for implementation in organic electronic devices. A critical parameter to evaluate the suitability of new organic materials in this respect remains the charge carrier mobility. As electron poor analogues to poly (3-alkylthiophene)s (P3ATs), *rr*-PTzs represent both possible electron-transporting (n-type) and hole-transporting (p-type) semi-conductors. In order to evaluate the properties of these new materials, series of single carrier devices were therefore prepared under the following configurations: ITO/PFN/*rr*-PTz/Ca/Al for electron-only devices, and ITO/PEDOT: PSS/*rr*-PTz/MoO₃/Ag for hole-only devices respectively (see Figure 4.36-a) and 4.37-a)). Mobility measurements were then performed by analyzing the current-voltage characteristics with space charge limited current (SCLC) theory.

Carrier mobility in PTzTHX determined using SCLC

Figure 4.36-b) and Figure 4.37-b) show the J-V characteristics of PTzTHX and PTzTNB single carrier devices respectively. For hole-only devices of PTzTHX, the as-spun film and the film annealed at 185 °C show very similar current densities, while the current density drastically increases upon annealing at 185 °C compared to the as-spun film for electron-only devices (see Figure 4.36-b)).

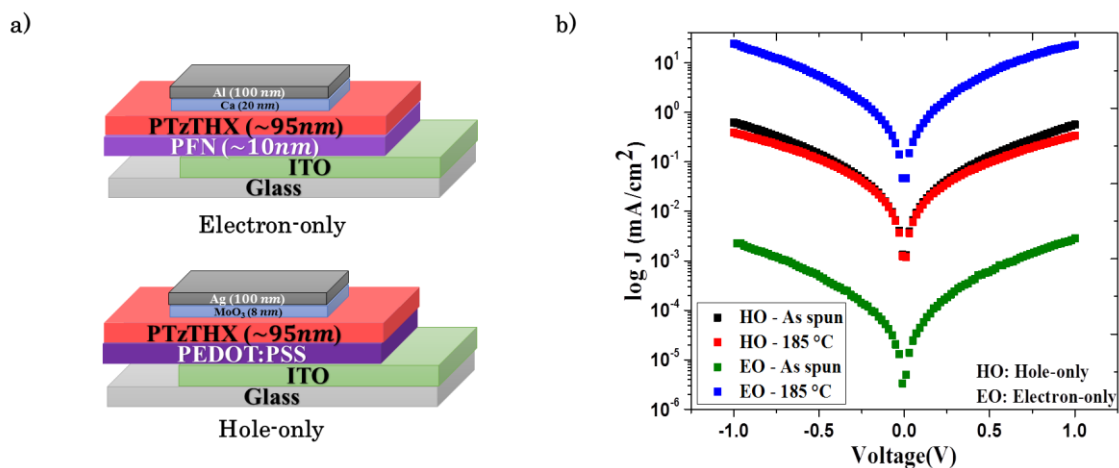


Figure 4.36: a) Electron-only and Hole-only device architectures of PTzTHX; b) Semi-logarithmic plots of J-V of the electron-only and hole-only based devices on PTzTHX, with as-spun films (black; green) and films annealed at 185 °C for 10 minutes (red; blue).

For hole-only devices of PTzTNB, the current density highly increases after annealing at 150 °C, in comparison to the as-spun film. Conversely in electron-only devices, the current density decreases after annealing of the film at 150 °C as seen in Figure 4.37-b).

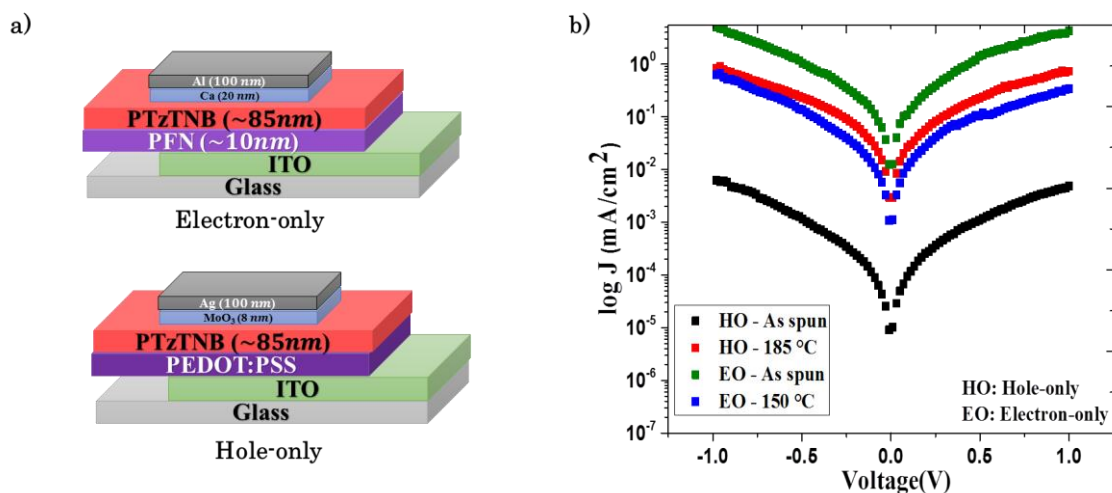


Figure 4.37: a) Electron-only and Hole-only device architectures of PTzTNB; b) Semi-logarithmic plots of J-V curves of the electron-only and hole-only based devices on PTzTNB, with as-spun films (black; green) and films annealed at 150 °C for 30 minutes (red; blue).

The SCL currents for the electron-only and hole-only devices for PTzTHX and PTzTNB are shown in Figure 4.38 below. As illustrated in the Figure, SCL conditions for higher voltages were verified for all devices.

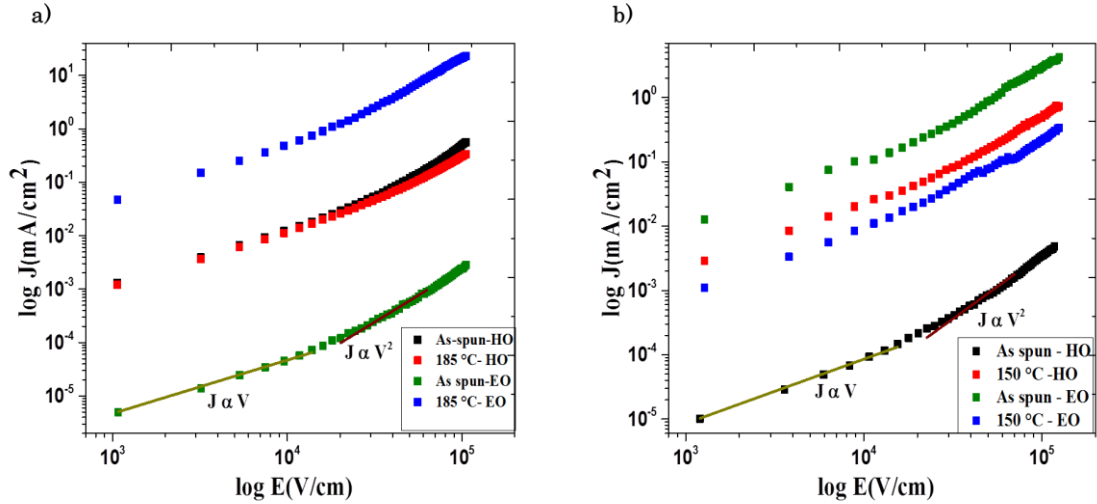


Figure 4.38: log (E)-log (J) curves of the electron-only and hole-only based devices **a)** PTzTHX and **b)** PTzTNB.

Hole mobilities

For films characterized as spun, PTzTHX hole-only devices yielded mobilities with an average value of $5.5 \pm 0.3 \times 10^{-5} \text{ cm}^2\text{V}^{-1}\text{s}^{-1}$, and the mobility does not change after the films were annealed at 185 °C ($4.8 \pm 0.3 \times 10^{-5} \text{ cm}^2\text{V}^{-1}\text{s}^{-1}$). Interestingly, this indicates that annealing has no influence on hole mobility of PTzTHX.

In PTzTNB, hole-only devices yielded average mobility values of $6.2 \pm 0.2 \times 10^{-6} \text{ cm}^2\text{V}^{-1}\text{s}^{-1}$ for the film as cast, which value increases after annealing to reach an average value of $3.8 \pm 0.2 \times 10^{-5} \text{ cm}^2\text{V}^{-1}\text{s}^{-1}$.

Electron mobilities

For PTzTHX, electron mobilities were measured for different batches of PTzTHX₄₀ and PTzTHX₆₀. In PTzTHX₄₀ electron mobilities for the devices measured as spun, exhibit an average value of $5.4 \pm 0.3 \times 10^{-7} \text{ cm}^2\text{V}^{-1}\text{s}^{-1}$, which increases significantly to reach the value of $8.4 \pm 0.3 \times 10^{-5} \text{ cm}^2\text{V}^{-1}\text{s}^{-1}$ after annealing at 185 °C. Comparatively, as-spun films of PTzTHX₆₀ exhibit an average electron mobility of $2.7 \pm 0.2 \times 10^{-7} \text{ cm}^2\text{V}^{-1}\text{s}^{-1}$, which value drastically increased by three orders of magnitude to

$6.4 \pm 0.3 \times 10^{-4} \text{ cm}^2\text{V}^{-1}\text{s}^{-1}$ upon annealing at 185 °C. This finding is consistent with the expected enhancement in electrical properties after crystallization of the polymer film. In comparison with hole mobilities in PTzTHX, these results indicate that electron transport is dominant.

For PTzTNB, electron mobility for devices measured as spun show relatively high average mobility values of $3.0 \pm 0.2 \times 10^{-4} \text{ cm}^2\text{V}^{-1}\text{s}^{-1}$. After annealing, the average mobility is $1.1 \pm 0.1 \times 10^{-5} \text{ cm}^2\text{V}^{-1}\text{s}^{-1}$ indicating that thermal treatment of the film slightly decreases electron transport. Similarly with PTzTHX, these results indicate that electron transport is predominant in PTzTNB.

Overall the observed hole mobilities in both polymers appear about one order of magnitude lower than those reported for the well-studied P3HT under similar conditions ^[126]. This is in agreement with the observed irreversible electrochemical oxidation of PTzs that is likely detrimental to p-type charge transport ^[125]. However, the results indicate that electrons are the predominant charge carrier in PTzTHX and PTzTNB, and that the electron mobility depends in general on the molecular weight of the polymer, as well as annealing. Notably, the devices fabricated from PTzTHX₆₀ ($6.4 \pm 0.3 \times 10^{-4} \text{ cm}^2\text{V}^{-1}\text{s}^{-1}$) showed significantly higher mobilities than those fabricated from PTzTHX₄₀ ($8.4 \pm 0.3 \times 10^{-5} \text{ cm}^2\text{V}^{-1}\text{s}^{-1}$). This is in agreement with the observation that higher molecular weights lead to improved charge transport in P3ATs ^[127]. More importantly, after annealing and concurrent crystallization, PTzTHX₆₀ exhibits electron mobilities that can in fact compete with those of established n-type-polymers such as naphthalenediimide-based P(NDI2OD-T2) ($\mu_e = 1.1 \times 10^{-4}$ to $8.0 \times 10^{-3} \text{ cm}^2\text{V}^{-1}\text{s}^{-1}$); determined via SCLC ^[128]. In parallel, PTzTNB exhibits high value of electron mobility up to $3.0 \pm 0.2 \times 10^{-4} \text{ cm}^2\text{V}^{-1}\text{s}^{-1}$, without annealing of the film.

These interesting results clearly establish rr-PTzs as possible electron-transporting (n-type) complements to the more electron rich rr-P3ATs. Of the known thiophene-based semiconductors, not many n-type polythiophenes have been reported, since the vast majority exhibit hole-transporting (p-type) ^[129-131]. However, for the fabrication of most of the organic electronic components such as complementary circuits, n-type/ambipolar OFETs, OPVs cells, OLEDs and complementary logic circuits, n-type thiophene-based oligomers and polymers are highly desirable ^[129,131]. In that sense, the high value of electron mobility demonstrated by

new PTzs polymers, confirm that these are promising candidates for organic electronic applications.

4.3.3. Comparison of electron and hole mobilities in PTZs and LCs dyes

A comparison of these results with those obtained with the new novel liquid crystal dyes is summarized in the Table 4.5 below. As detailed in the table, the overall results demonstrate that electrical properties are generally enhanced upon annealing at a given temperature for the polymers (slightly higher than the melting point), and by cooling from the different mesophase for the LC dyes. However, much higher values of hole mobility are achieved in LCs dyes compared to the PTzs polymers. Average hole mobility in the range of $10^{-4} \text{ cm}^2\text{V}^{-1}\text{s}^{-1}$ is achieved both for 2,3-FFPTB and 2,6-FFPTB at ($\mu_p = (2.3 \pm 0.3) \times 10^{-4} \text{ cm}^2\text{V}^{-1}\text{s}^{-1}$ and $\mu_p = (6.1 \pm 0.3) \times 10^{-4} \text{ cm}^2\text{V}^{-1}\text{s}^{-1}$ respectively, after cooling from isotropic phase. While the highest value of hole-mobility achieved in the PTzs polymers is in the order of $10^{-5} \text{ cm}^2\text{V}^{-1}\text{s}^{-1}$ for annealed samples ($\mu_p = (4.8 \pm 0.3) \times 10^{-5} \text{ cm}^2\text{V}^{-1}\text{s}^{-1}$ for PTzTHX; $\mu_p = (3.8 \pm 0.2) \times 10^{-5} \text{ cm}^2\text{V}^{-1}\text{s}^{-1}$ for PTzTNB). This result also indicates that hole-mobility in LCs dyes are very comparable to the hole mobility of common polymers used in organic electronics.

Inversely, the electron mobility measured in PTzs polymers was generally one order of magnitude higher than that measured in LC dyes. Electron mobility up to $(6.4 \pm 0.3) \times 10^{-4} \text{ cm}^2\text{V}^{-1}\text{s}^{-1}$ could be achieved in PTzTHX₆₀ for devices annealed at 185 °C, and up to $(3.0 \pm 0.2) \times 10^{-4} \text{ cm}^2\text{V}^{-1}\text{s}^{-1}$ for PTzTNB devices measured as spun, while the highest values of electron mobility reached in LC dyes were $(1.8 \pm 0.2) \times 10^{-5} \text{ cm}^2\text{V}^{-1}\text{s}^{-1}$ and $(7.8 \pm 0.5) \times 10^{-6} \text{ cm}^2\text{V}^{-1}\text{s}^{-1}$ in 2,3-FFPTB and 2,6-FFPTB respectively. However, for lower molecular weights of PTzTHX, the electron mobility in 2,3-FFPTB and PTzTHX₄₀ become comparable ($(8.4 \pm 0.3) \times 10^{-5} \text{ cm}^2\text{V}^{-1}\text{s}^{-1}$ for PTzTHX₄₀ and $(1.8 \pm 0.2) \times 10^{-5} \text{ cm}^2\text{V}^{-1}\text{s}^{-1}$ for 2,3-FFPTB). The same was observed for the annealed films of PTzTNB ($(1.1 \pm 0.3) \times 10^{-5} \text{ cm}^2\text{V}^{-1}\text{s}^{-1}$ for PTzTNB and $(1.8 \pm 0.2) \times 10^{-5} \text{ cm}^2\text{V}^{-1}\text{s}^{-1}$ for 2,3-FFPTB)).

Table 4.5: Summary of mobility measurements for 2,3-FFPTB and 2,6-FFPTB in comparison with PTzTNB and PTzTHX estimated using SCLC.

Materials		Annealing Temperature	$\mu_p (cm^2V^{-1}s^{-1})$ Hole-only	$\mu_n (cm^2V^{-1}s^{-1})$ Electron-only
LC dyes	2,3-FFPTB	As-spun	$(4.7 \pm 0.3) \times 10^{-7}$	$(5.7 \pm 0.6) \times 10^{-8}$
		80 °C	$(2.3 \pm 0.3) \times 10^{-6}$	$(3.3 \pm 0.3) \times 10^{-7}$
		105 °C	$(3.3 \pm 0.3) \times 10^{-6}$	$(1.6 \pm 0.2) \times 10^{-5}$
		120 °C	$(9.5 \pm 0.9) \times 10^{-6}$	$(1.8 \pm 0.2) \times 10^{-5}$
		160 °C	$(2.3 \pm 0.3) \times 10^{-4}$	$(1.2 \pm 0.2) \times 10^{-5}$
	2,6-FFPTB	As-spun	$(5.1 \pm 0.3) \times 10^{-6}$	$(2.0 \pm 0.2) \times 10^{-7}$
		120 °C	$(4.5 \pm 0.3) \times 10^{-5}$	$(2.6 \pm 0.2) \times 10^{-7}$
		160 °C	$(6.1 \pm 0.3) \times 10^{-4}$	$(7.8 \pm 0.5) \times 10^{-6}$
Polymers PTzs	PTzTHX ₄₀	As-spun	-	$(5.4 \pm 0.3) \times 10^{-7}$
		185 °C	-	$(8.4 \pm 0.3) \times 10^{-5}$
	PTzTHX ₆₀	As-spun	$(5.5 \pm 0.3) \times 10^{-5}$	$(2.7 \pm 0.2) \times 10^{-7}$
		185 °C	$(4.8 \pm 0.3) \times 10^{-5}$	$(6.4 \pm 0.3) \times 10^{-4}$
	PTzTNB ₈₄	As-spun	$(6.2 \pm 0.2) \times 10^{-6}$	$(3.0 \pm 0.2) \times 10^{-4}$
		150 °C	$(3.8 \pm 0.2) \times 10^{-5}$	$(1.1 \pm 0.1) \times 10^{-5}$

These results indicate that the new conducting polymers are clearly n-type materials while the LCs dyes are more p-type materials. However, by cooling from the smectic phases of 2,3-FFPTB, good electron transport is achieved, making it comparable with the PTzs polymers. This interesting finding clearly demonstrate that LCs dyes compared to their polymeric counterparts, offer the advantage of achieving a more balanced charge carrier, hence are more favorable for an ambipolar transport in organic semiconductors.

Summary

Electrical characterization of PTzTHX and PTzTNB confirmed these polymers to be n-type materials, with electron mobility reaching up to $(6.4 \times 10^{-4} \pm 0.3) cm^2V^{-1}s^{-1}$. Crucially, mobilities for PTzTHX increased drastically upon annealing of the devices, and were found to

be consistently higher for PTzTHX₆₀ than for PTzTHX₄₀. Both observations point towards a direct correlation between the charge carrier mobility and the highly order crystalline morphology of the polymer films. Compared to LC dyes, it was found out that higher hole mobility was achieved in LC dyes, while the conducting polymers show generally higher values of electron mobility in comparison to LC dyes. Nevertheless, electron mobilities in 2,3-FFPTB possessing two smectic phases become comparable with those of PTzs, when the molecular weight of polymers were lowered for PTzTHX or films annealed for PTzTNB. Although PTzs polymers were better electron transporting materials, charge carrier transport in general could be better controlled in LCs dyes.

4.4. Comparison of hole mobilities in Liquid crystal dyes measured with impedance spectroscopy and space charge limited current

Charge transport in organic materials is mainly quantified by charge carrier mobility. Therefore, both from scientific and technological perspectives, the characterization of charge transport in organic semiconductor is of mean importance. It appears then essential to accurately measure the charge carrier mobility inside devices. Among the most widely used methods in the literature, one can cite space-charge-limited current (SCLC), time of flight (TOF), carrier extraction by linearly increasing voltage (CELIV), double injection (DoI), field effect transistors (FETs), and impedance spectroscopy (IS) ^[97].

For diode architectures, as used in this thesis, SCLC and IS were chosen to be the most suitable methods ^[97, 102] to use for the estimation of mobilities. The detailed theoretical description of these two methods can be found in Chapter 2. Although both techniques rely on extracting carrier mobility from dark electrical characteristics, large discrepancies in the mobility values estimated using these two techniques on the same devices were observed. In this section, I will compare the underlying assumptions for extracting mobility using IS and SCLC and discuss possible reasons for the differences in the mobility values. Extracting reliable mobility values which are comparable between laboratories remains challenging ^[102]. As discussed in the literature ^[97, 102,132] values of mobility depend on the device architecture, measurement method and assumptions of the applied model. It is well-known in the literature that mobility measured from the same material, shows orders of magnitude variations depending on the method applied ^[102]. Though discussions to clarify the possible reasons of discrepancies observed using different techniques for the measurement of mobility in disordered materials have been considered in the literature ^[102, 132-133], this still an open topic for discussions in this research field. Here I attempt to discuss the results on mobility results from the LC dyes investigated in this thesis to add insights in the understanding of limiting factors for an accurate measurement of charge carrier mobility in organic films.

4.4.1. Results

Before proceeding to results, different assumptions made for both techniques are briefly reminded. In the case of SCLC theory, the main assumptions made are that of trap-free transport and field-independent mobility over the voltage range investigated. This technique

also assumes a unipolar transport, insured by a perfect Ohmic contact (no injection barrier) between the metal contact and the HUMO/LUMO of the material under investigation ^[101]. For the IS, the assumption of perfect Ohmic contacts for the device and field independence of mobilities are also considered. IS mainly investigates charge transport kinetics and relaxation processes involved in solid-state devices. Practically, a DC bias V_{DC} together with a much weaker AC voltage are applied to the sample and a SCLC flow is generated ^[97].

So for both techniques, a careful selection of the electrodes is required. Hole-only diodes are those considered for discussion in this section. Considering the HUMO and LUMO values of the three LCs dyes investigated: FPPTB, 2,3-FFPTB and 2,6-FFPTB; ITO/PEDOT:PSS and MoO₃/Ag were chosen as electrodes to ensure Ohmic contact at the electrode/organic interface, and an efficient hole injection/extraction inside devices. The choice of Ag as cathode, was to block injection of electron, so that the device will be hole dominant. Figure 4.39 shows the energy diagrams of the three LCs dyes studied in this thesis.

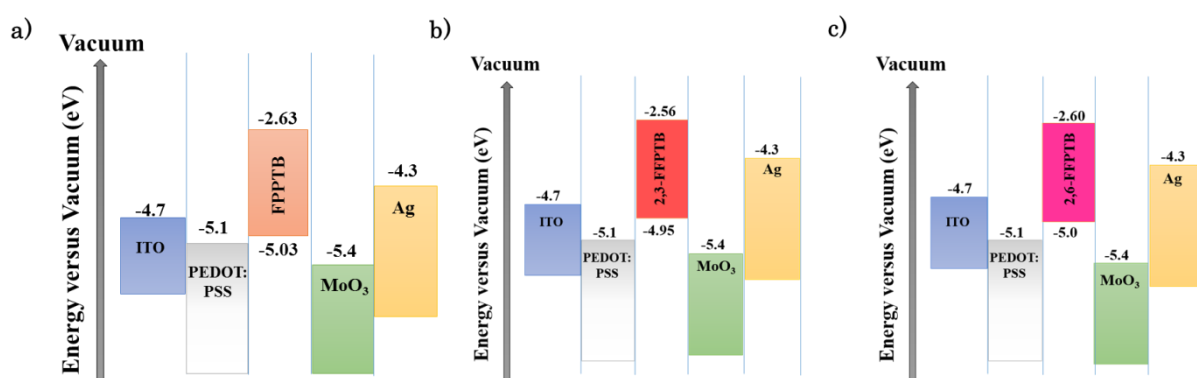


Figure 4.39: Schematic of energy-level alignment diagram showing the LUMO and HOMO energies of the three LC dyes studied and the work functions of the electrode materials: a) FPPTB b) 2, 3-FFPTB c) 2, 6-FFPTB.

The single carrier devices were prepared as detailed in the method section. Mobility measurements were then performed by analyzing Bode plots for $-Z''$ versus f spectra for IS, and the current-voltage characteristics for the SCLC. For IS, the peak frequency extracted from the Bode plot allow for the determination of mobility. Figure 4.40 below recalls the Bode plots of hole-only diodes of FPPTB, 2,3-FFPTB and 2,6-FFPTB.

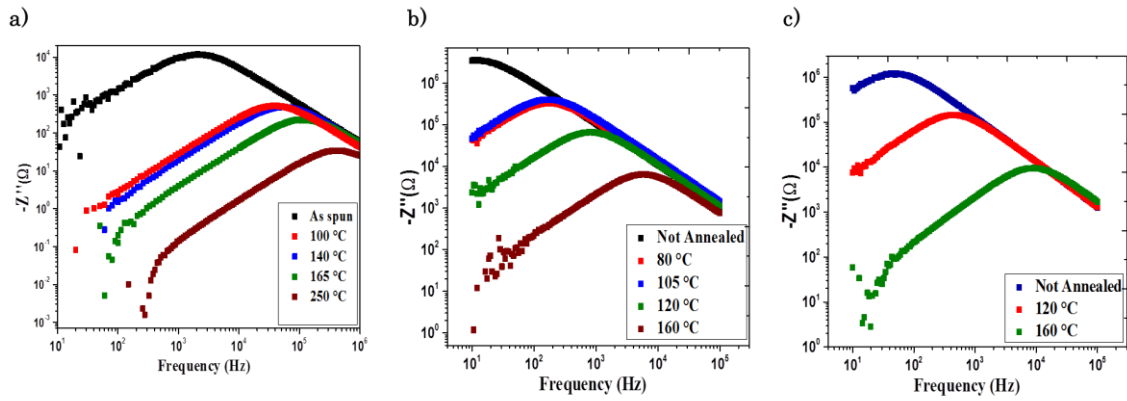


Figure 4.40: Bode plots for $-Z''$ versus f spectra for the hole-only diodes of a) FPPTB, b) 2,3-FFPTB, c) 2,6-FFPTB.

Field-independence mobility, which is a validation criteria for both IS and SCLC techniques, was also investigated for all devices using impedance and this confirms that mobility was field-independent for each material as shown in Figure 4.41.

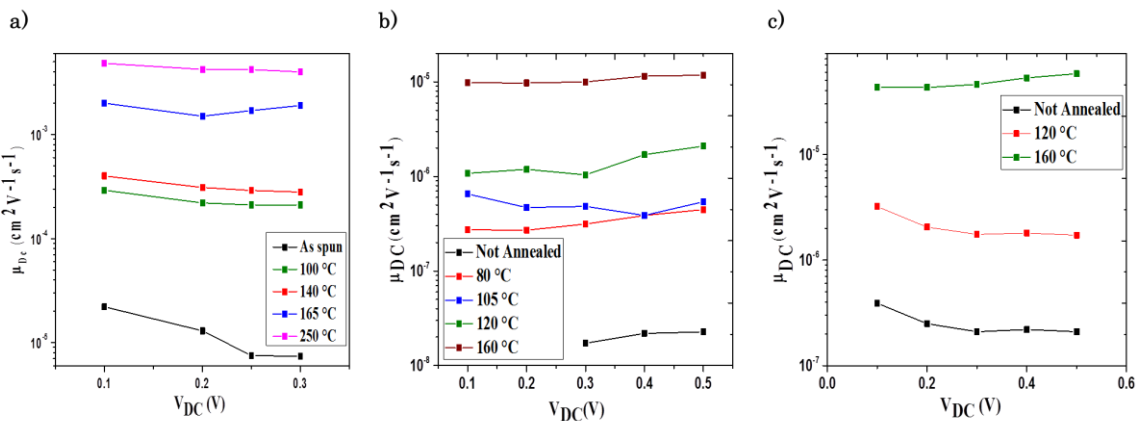


Figure 4.41: Verification of field-independence mobility for a) FPPTB b) 2, 3-FFPTB and c) 2, 6-FFPTB in the voltage ranges as shown on the graphs.

For SCLC, the Space charge limited currents at higher voltage ($J \propto V^2$) was first verified and confirmed, as shown in Figures 4.42 for FPPTB, 2,3-FFPTB and 2,6-FFPTB diodes.

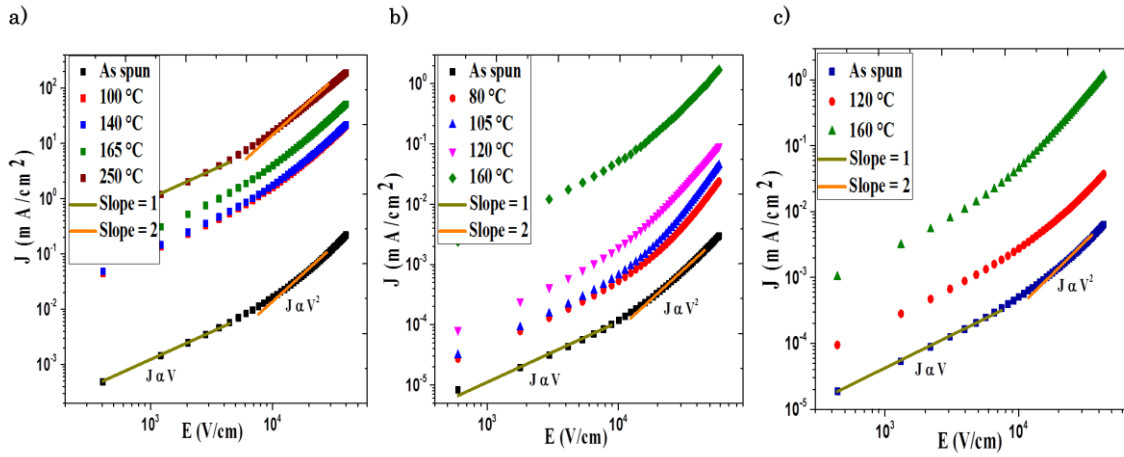


Figure 4.42: log (E)-log (J) curves (SCLC) of hole-only diodes of **a)** FPPTB, **b)** 2,3-FFPTB, **c)** 2,6-FFPTB.

The mobilities values calculated from IS and SCLC for FPPTB, 2,3-FFPTB and 2,6-FFPTB are summarized for each LC dye in the Table 4.6.

Table 4.6: Mobilities values calculated from IS and SCLC for **a)** FPPTB, **b)** 2, 3-FFPTB, **c)** 2, 6-FFPTB.

a) FPPTB

Temperature (°C)	As spun	100	140	165	250
$\mu_{IS}(cm^2V^{-1}s^{-1})$	$(2.2 \pm 0.4) \times 10^{-5}$	$(3.0 \pm 0.5) \times 10^{-4}$	$(4.0 \pm 0.7) \times 10^{-4}$	$(2.0 \pm 0.3) \times 10^{-3}$	$(5.0 \pm 0.8) \times 10^{-3}$
$\mu_{SCLC}(cm^2V^{-1}s^{-1})$	$(1.3 \pm 0.3) \times 10^{-4}$	$(1.3 \pm 0.3) \times 10^{-2}$	$(1.4 \pm 0.3) \times 10^{-2}$	$(9.4 \pm 0.6) \times 10^{-2}$	$(1.4 \pm 0.3) \times 10^{-1}$

b) 2,3-FFPTB

Temperature (°C)	As spun	80	105	120	160
$\mu_{IS}(cm^2V^{-1}s^{-1})$	$(2.1 \pm 0.1) \times 10^{-8}$	$(3.4 \pm 0.2) \times 10^{-7}$	$(5.1 \pm 0.3) \times 10^{-7}$	$(1.4 \pm 0.1) \times 10^{-6}$	$(1.1 \pm 0.1) \times 10^{-5}$
$\mu_{SCLC}(cm^2V^{-1}s^{-1})$	$(4.7 \pm 0.3) \times 10^{-7}$	$(2.3 \pm 0.3) \times 10^{-6}$	$(3.3 \pm 0.3) \times 10^{-6}$	$(9.5 \pm 0.9) \times 10^{-6}$	$(2.3 \pm 0.3) \times 10^{-4}$

c) **2, 6-FFPTB**

Temperature (°C)	As spun	120	160
$\mu_{IS}(cm^2V^{-1}s^{-1})$	$(2.6 \pm 0.1) \times 10^{-7}$	$(2.1 \pm 0.1) \times 10^{-6}$	$(5.0 \pm 0.2) \times 10^{-5}$
$\mu_{SCLC}(cm^2V^{-1}s^{-1})$	$(5.1 \pm 0.3) \times 10^{-6}$	$(4.5 \pm 0.3) \times 10^{-5}$	$(6.1 \pm 0.3) \times 10^{-4}$

The hole mobility values versus annealing temperature determined with IS for all three LC dyes plotted in comparison with SCLC ones are shown in Figure 4.43.

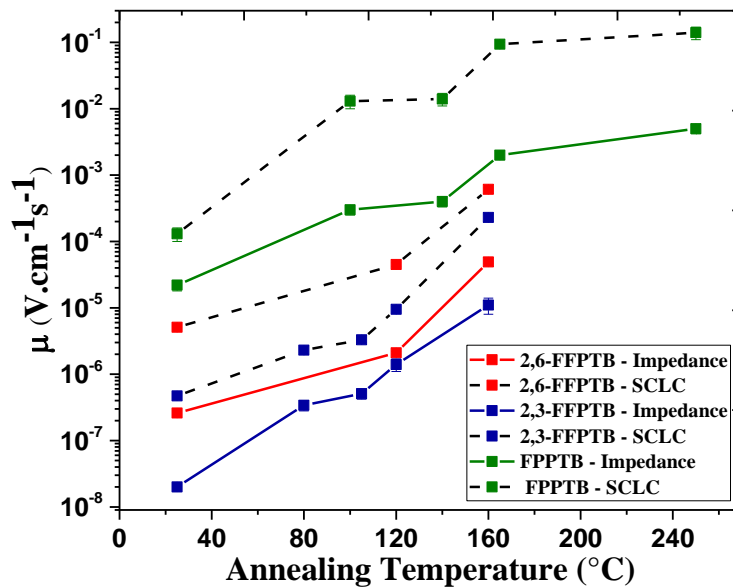


Figure 4.43: IS mobilities (solid lines) values versus temperature, in comparison to SCLC mobilities values (dash lines), for hole-only diodes of: **FPPTB** (green), **2, 3-FFPTB** (blue) and **2, 6-FFPTB** (red).

The results as clearly demonstrated in the Figure 4.43 and Table 4.6, show that SCLC mobilities value are in general for both three materials, higher of one order magnitude compared to those measured using impedance spectroscopy. Since these measurements were performed on the same samples for both techniques, one should have expected to obtain comparable values of mobilities for each LC dye. One first attempt to explain the discrepancies observed is the different measurement conditions. SCLC is a Steady-state current–voltage technique applied upon a voltage range, and governed by the space charge limited (SCL) effect. On the other hand impedance spectroscopy is a frequency-domain

technique applied at a single voltage upon a frequency range and governed by the transit of injected charge carriers ^[97]. Possible reasons to discrepancies arising from one technique or the other are discussed below in more detail.

4.4.2. Discussion

In impedance spectroscopy in general, what is actually extracted from the $-\text{Im } Z$ vs f graph is the transient time of carriers τ_{DC} , which is related to the mobility μ by the equation (13) (Chapter 2). Impedance spectroscopy is based on the specific frequency dependence displayed by the admittance. And the admittance being governed by the transit of injected charge carriers, this implies that τ_{DC} also accounts for carrier injection/extraction rates ^[94, 97, 134]. So, if the injection rate is limited, this lowers the value of mobility and this might be a reason why lower values of IS values of mobilities is observed in comparison to SCLC values. In the literature, studies on charge transport in organic semiconductors using impedance spectroscopy revealed that numerous factors such as the contact resistance, injection barrier, and the presence of localized-states distribution can affect the mobility ^[135]. Below, the influence of these factors on the IS mobilities measured in this thesis are examined.

Masashi Takata et al ^[136] demonstrate using IS for the characterization of OLED, that the mobility of charge carrier decreases with increase of contact resistance if the measured value of mobility is greater than $10^{-5} \text{cm}^2 \text{V}^{-1} \text{s}^{-1}$. And that mobility is accurately determined when its value does not exceed $10^{-5} \text{cm}^2 \text{V}^{-1} \text{s}^{-1}$ for a finite value of contact resistance (1-100 \square) for semiconducting layer of 100nm. For reminder, the impedance data can be modelled with a simple RC element consistent with a single relaxation time in the device. The corresponding equivalent circuit includes in general a contact resistance and a bulk resistance, and their values could be extracted from a Cole-Cole plot of the complex impedance. Considering the results obtained in this work, only FPPTB exhibits hole mobilities beyond $10^{-5} \text{cm}^2 \text{V}^{-1} \text{s}^{-1}$ using IS. And the mobility values of 2,3-FFPTB and 2,6-FFPTB measured with IS does not reach $10^{-4} \text{cm}^2 \text{V}^{-1} \text{s}^{-1}$ (see Table 4.6). The results of FPPTB were modelled with an RC element, and the values of the dispersion parameter of the CPE were negligible. So these devices should really satisfy the requirements.

Takayuki Okachi et al ^[137], performed simulations on OLEDs to evaluate the influence of injection barrier on the mobility using IS measurements. They found that for the Schottky

contact with barrier height less than 0.4 eV, the mobility of carrier injected can be correctly determined by analyzing the frequency dependence of conductance. The same way, in the case where the barrier height is less than 0.2 eV, the mobility can also be determined accurately by analyzing the frequency dependence of capacitance. Their study revealed that if the height barrier exceeds 0.4 eV, the mobility is underestimated especially at low dc bias. This same study demonstrated that the hole mobility of the well-studied small molecule \square -NPD diode measured with IS, was one order of magnitude lower compared to the hole mobility measured on the same material using TOF measurement in a separate study^[138]. The lower value of mobility observed with IS, was due to the higher value of injection barrier estimated to be 0.6 eV^[137, 138]. This highlights the importance of the injection barrier on the analysis, and no or very low injection barrier is strongly recommended to accurately measure mobility using IS. However extracting the height of the injection barriers for the single carrier diodes is non-trivial. This was not investigated explicitly in this thesis. It is assumed, however, that voltage-independent mobility values (as observed in our IS measurements) are a good indication of a negligible injection barrier in the case of LCs devices.

Because organic semiconductors contain inherently localized-states in their forbidden gap^[135], another factor which is likely to affect mobility measured using IS, is the localized-states distribution inside the bulk material. On this point, Takayuki Okachi et al in another study^[139] demonstrated that the drift mobilities in OLEDs can be accurately determined by IS measurements even in the presence of localized states. Their study also showed that the frequency behavior of capacitance is lowered by distributed localized states. This suggests in the case of our study, that the localized-states are most likely not the reason, of the lower values of IS mobilities observed.

After examining these three factors (contact resistance, injection barrier and localized-states distribution) in the context of our study, the argument of a limited injection rate as the reason for underestimated values of IS mobilities, is likely the most plausible.

Another argument to explain this could be a dispersion of charge transport, in which charge carriers undergo relaxation on the timescale of the experiment. But, Liquid crystalline semiconductors demonstrate in general a limited or no dispersive transport^[15]. And this was verified for the case of FPPTB which demonstrated a nearly ideal capacitive behavior, and negligible dispersive transport, independent of annealing conditions.

A study from Tracey M. Clarke et al ^[132] compared five different measurement techniques in the determination of charge carrier lifetime (τ) on the same sample. Their study was performed on a donor acceptor polymer PDTSiTTz, blended with PCBM and involved small perturbation methods: Impedance spectroscopy (IS) and transient photovoltage (TPV); transient charge extraction-based methods: photo-CELIV and time-resolved charge extraction (TRCE); and the optical method transient absorption spectroscopy (TAS). The results demonstrated that the techniques of TAS, TRCE, photo-CELIV and TPV all produce very similar charge carrier lifetimes if the charge density is kept at a high level (close to 100 mWcm² illumination and open circuit conditions), regardless of whether the technique is a transient or small perturbation method, and regardless of whether it is optical or optoelectronic. However, the value of τ measured with IS was significantly lower in comparison to other techniques. At lower carrier density, the discrepancies among different techniques became noticeable. A comparison of TRCE with the small perturbation methods revealed a large difference in carrier lifetime τ between EIS and TRCE. The reasons they provided to explain lower value of τ measured using IS were amongst others: a monomolecular recombination inside the bulk or RC limitations. In particular, the large discrepancy observed between IS and TRCE was attributed to a contribution from the IS Nyquist plots, which have in the case of their study, a much flatter semicircle than that would occur from a simple capacitor/resistor in parallel. This is most likely due to dispersion, and may give underestimated capacitance and thus charge density values. The case of dispersive transport being already eliminated in the case of our study, monomolecular recombination and RC limitations remain then, as possible reasons for lower values of IS mobilities observed.

Considering the SCLC results on the other hand, it is shown as illustrated in Figure 4.42 that SCL current which arises with a slope of 2 on the J-V curves was satisfied for all devices. One can then assume the values of calculated mobilities to be accurate. Nonetheless, as frequently discussed in the literature ^[101-102, 134], it remains quite difficult to conclude only from the J-V characteristics whether the current is based on SCLC or injection limited current (ILC). ILC occurs if the injection current from the contact into the organic is insufficient to deliver the maximum possible SCLC in the material, because of a too large injection barrier ^[140]. SCLC conditions confirmed on the only basis of the agreement between the experimental data and the fitted results, is therefore not always straightforward. Nevertheless, looking at the energy diagram of devices studied in this work (see Figure 4.39), ILC is more unlikely to be favored,

but instead a SCLC condition. If the optical band gaps of the LCs dyes at hand (FPPBT - 2.50 eV; 2, 3-FFPTB - 2.39 eV ; 2,6-FFPTB – 2.40 eV) are considered in comparison with the well-studied hole transporting material α -NPD for instance, α -NPD yields a much larger optical band gap compared to the LCs and is estimated at about 3.1 eV^[141-142]. Therefore, one might expect the height of the injection barrier ITO/PEDOT: PSS/LC, to be smaller than that of ITO/ α -NPD reported to be at about 0.6 eV^[101, 138]. According to the literature^[143-144], the ideal of injection barrier height being to not exceed 0.3 eV for SCLC experiments, B.Z. Wang et al^[101] recommended that the injection barrier height must be verified prior mobility measurement using J-V characteristics. Furthermore, SCLC with trapping has been considered in the literature to account for slopes that are larger than 2 in the higher voltage regime^[101, 145], which phenomenon was not observed in the case of this study.

After looking at the limits of both measurement techniques used in this work, it worth to remind that, they both make assumptions based on space charge limited transport. Another important point, is that they also rely on very accurate measurements of the film thickness d as it is shown in the formula used to calculate because μ in both cases. Practically, SCLC calculations involve d^3 while d^2 is used for IS.

Looking at a specific difference between both techniques, it indicates that SCLC relies on injection (from Ohmic contacts) and the mobility is extracted by averaging transport phenomena over the low voltage regime (Ohmic) and high voltage regime (space charge limited). The charge carrier concentration, and then mobility are obtained by considering the intersection of the two regimes ($J \propto V$; $J \propto V^2$). And this includes another factor of error involved in determining the exact voltage where they intersect. In IS, space charge limited transport is also assumed. But the analysis of the mobility is based on the peak frequency in the Im Z vs frequency plot. This peak is assumed to account for the transit time of carriers in the device. But in the case of dispersive transport, the peak is broadened. However, dispersive transport was proved to be negligible in the case of all the materials studied in this work (as shown by the voltage-independent mobility values). Nevertheless, a lack of a clear understanding of the parameter k remains in the case of IS analysis.

This leads to some relevant reasons which might explain the difference observed in the mobilities values as measured in this work:

There is a larger error associated in estimating SCLC mobilities due to the thickness parameter included in the calculations (d^3 for SCLC and d^2 for impedance).

Mobility value from SCLC needs to be determined from a single voltage point where Ohmic/SCLC behaviors intersect. This means that transport phenomena might be averaged in a wider voltage range.

Though IS is a perturbative measurement, it also includes the injection time. This may result in lower mobilities if injection is limited in any way.

IS gives mobility values at every DC offset in contrast to SCLC where you extract one value from the entire JV curve.

Generally one could assume that impedance spectroscopy is more accurate because, it is a perturbative technique which allows extracting the mobility at each DC voltage independently. Since not large variations in the values of mobility from IS were observed in this study, this suggests that the results are consistent (even if they are lower due to injection/contact resistance).

Summary

To close this discussion, it comes out from this comparative study that the accurate determination of the mobility, in particular for new materials systems remains challenging, independently of the method used. Many relevant points are however worth to be summarized here, which are necessary in the goal of tackling this challenge. A judicious choice of electrodes in the design of single carrier device appears as the most important step to consider, for this is crucial to form perfect Ohmic contacts essential for reliable measurement outcomes. However, forming perfect Ohmic contacts is generally difficult due to the large band gaps of most of the organic semiconductors ^[97, 145]. Nevertheless, achieving this condition remains a prerequisite to reliable mobility measurements using most of the common methods, as such concerned in this study.

The choice of electrodes remains also determinant, to ensure ideal injection barriers for transport that will be bulk-limited instead of interface limited in case of Steady-state methods particularly. Therefore, a prior verification of the height of injection barrier is necessary in the case of new materials, as a guideline in the choice of the most accurate method to use for the

determination of the mobility. Another consideration is that of the design of new materials itself. Most of the common metal and polymer electrodes used in scientific community today have been well studied and characterized. So from the material synthesis point of view, it is desirable to design new materials which HOMO and LUMO frontiers can fit energetically with the existing electrodes, in an optimized way. This would be ideal even though, it remains difficult to realize in a practical way.

5. Conclusions

In this thesis the charge transport properties in newly synthesized soluble liquid crystalline (LC) dyes were examined, with the goal to achieve high mobility crystalline thin films with good thermal stability. The strategy employed for this was to address current bottlenecks in the field of organic electronics associated with film formation and crystal growth morphology, poor structural integrity and low thermal stability. Thin films prepared with LC dyes are shown to be highly ordered, with reduced grain boundaries and crystal defects. Mobility measurements were performed using current-voltage measurements and impedance spectroscopy.

The first material investigated was the calamitic LC dye FPPTB. FPPTB was crystalline at room temperature and was easily processable from solution. Highly ordered films were obtained after cooling from nematic phase (between 149 °C and 230 °C) and isotropic melt (above 230 °C), and the best crystalline order was achieved in films annealed at 140 °C (just below the crystalline \rightarrow nematic transition). It was demonstrated from XRD and POM studies that cooling from the nematic and isotropic phase helps to significantly reduce grain boundaries in films but also induced local structural variations in the molecular packing of crystalline FPPTB. Optical microscopy was used to confirm annealing-induced changes in molecular aggregation of films. High carrier mobilities were achieved with a drastic increase from $\mu = (2.2 \pm 0.4) \times 10^{-5} \text{cm}^2 \text{V}^{-1} \text{s}^{-1}$ in as spun FPPTB films to $\mu = (5.0 \pm 0.8) \times 10^{-3} \text{cm}^2 \text{V}^{-1} \text{s}^{-1}$ in films cooled from the isotropic melt. It was found that the relationship between thermal stability and high carrier mobility values is governed by the interplay between the long range crystal order, and the short range molecular interaction characterized here by increased $\pi - \pi$ interactions between molecular pairs in the FPPTB film.

Based on the findings obtained with FPPTB, two calamitic LC dyes exhibiting very similar molecular structures were investigated, with the focus laid on understanding how variations in the position of the fluorine substitution influence molecular packing and charge carrier mobility. In particular the influence of the ortho-substitution (2,3-FFPTB) and para-substitution (2,6-FFPTB) of fluorine on the benzene ring on ambipolar transport was investigated. In-situ XRD studies demonstrated that the fluorine substitution has a large impact in molecular packing of crystalline 2,3-FFPTB and 2,6-FFPTB films. Very high hole

mobility in the order of $(6.1 \pm 0.3) \times 10^{-4} \text{ cm}^2\text{V}^{-1}\text{s}^{-1}$ in 2,6-FFPTB and $(2.3 \pm 0.3) \times 10^{-4} \text{ cm}^2\text{V}^{-1}\text{s}^{-1}$ in 2,3-FFPTB ; and electron mobility in the order of $(1.8 \pm 0.2) \times 10^{-5} \text{ cm}^2\text{V}^{-1}\text{s}^{-1}$ in 2,3-FFPTB and $(8 \pm 0.5) \times 10^{-6} \text{ cm}^2\text{V}^{-1}\text{s}^{-1}$ in 2,6-FFPTB were achieved. The main finding is the demonstration that cooling from ordered smectic films of 2,3-FFPTB help to achieve high electron mobilities and a high ambipolar transport, which could not be achieved in 2,6-FFPTB possessing no smectic phase. .

Finally electron transport in the novel n-type polythiophene derivatives, PTzTHX and PTzTNB, was investigated. Very high electron mobilities in the order of $(6.4 \pm 0.3) \times 10^{-4} \text{ cm}^2\text{V}^{-1}\text{s}^{-1}$ and $(3.0 \pm 0.2) \times 10^{-4} \text{ cm}^2\text{V}^{-1}\text{s}^{-1}$ were obtained respectively. Compared to the literature, these values were found to be comparable to those of established n-type polymers. The materials were found to demonstrate some ambipolar transport, and, hole mobilities up to $(5.5 \pm 0.3) \times 10^{-5}$ for PTzTHX and $(3.8 \pm 0.2 \times 10^{-5})$ for PTzTNB were measured. The results compared to the LC dyes, show that the PTzs hole mobilities appears lower of one order magnitude indicating that hole transport in LC dyes is more efficient. However PTzs polymers exhibited much higher electron mobility values compared to LC dyes.

Polymers have been widely investigated in the literature for opto-electronic applications; however few studies have examined the potential of LC dyes. These results demonstrate the advantages of the new LC dyes, namely the possibility to exploit self-assembly to achieve highly ordered, thermally stable films with good electrical properties.

In the prospect of electronic applications, charge carrier mobility remains the key parameter to consider. Accurate measurement of the mobility is then of high interest from both a scientific and technological perspective. Impedance spectroscopy (IS) and space charge limited current (SCLC) analyses were used for the extraction of mobility in this work. The overall results demonstrated that mobility values measured using SCLC were in general one order of magnitude higher than mobilities extracted using IS. In the final section of this thesis, the underlying assumption for extracting mobility using IS and SCLC and the possible reasons for the discrepancies in the mobility values were discussed. As main assumptions for accurate mobility measurements, both models assume an Ohmic contact at the electrode/organic interfaces, a field independent mobility over the voltage range investigated and require a low height injection barrier to ensure an efficient injection of charges inside the bulk. Among others reasons, a larger error associated in estimating SCLC mobilities due to

the thickness parameter included in the calculations (d^3 for SCLC and d^2 for impedance) and a limited injection rate were identified as being the main possible reasons for the observed discrepancies. The outcome discussion of this section highlighted the remaining challenge in an accurate determination of the mobility for new materials systems, independently of the method used.

Bibliography

- [1] Coropceanu, V., Cornil, J., da Silva Filho, D.A., Olivier, Y., Silbey, R. and Brédas, J.L. Charge transport in organic semiconductors. *Chem. rev.* **2007**, *107* (4), 926-952.
- [2] Köhler, A., Bässler, H. The Electronic Structure of Organic Semiconductors. *Electronic Processes in Organic Semiconductors, An Introduction.* **2015**, 1-86.
- [3] Vijila, C., Singh, S.P., Williams, E., Sonar, P., Pivrikas, A., Philippa, B., White, R., Naveen Kumar, E., Gomathy Sandhya, S., Gorelik, S., Hobley, J. Relation between charge carrier mobility and lifetime in organic photovoltaics. *J. Appl. Phys.* **2013**, *114* (18), 184503.
- [4] Pivrikas, A., Neugebauer, H., Sariciftci, N.S. Charge carrier lifetime and recombination in bulk heterojunction solar cells. *IEEE journal of selected topics in quantum electronics* **2010**, *16* (6), 1746-1758.
- [5] Sellner, S.; Gerlach, A.; Schreiber, F.; Kelsch, M.; Kasper, N.; Dosch, H.; Meyer, S.; Pflaum, J.; Fischer, M.; Gompf, B. Strongly Enhanced Thermal Stability of Crystalline Organic Thin Films Induced by Aluminum Oxide Capping Layers *Adv. Mater.* **2004**, *16* (19), 1750–1753.
- [6] Yuan, Y.; Giri, G.; Ayzner, A. L.; Zoombelt, A. P.; Mannsfeld, S. C. B.; Chen, J.; Nordlund, D.; Toney, M. F.; Huang, J.; Bao, Z. Ultra-High Mobility Transparent Organic Thin Film Transistors Grown by an Off-Center Spin-Coating Method. *Nat. Commun.* **2014**, *5*, 3005.
- [7] Mas-Torrent, M.; Rovira, C. Novel Small Molecules for Organic Field-effect Transistors: Towards Processability and High Performance *C. Chem. Soc. Rev.* **2008**, *37* (4), 827–838.
- [8] Iino, H.; Usui, T.; Hanna, J. Liquid Crystals for Organic Thin-Film Transistors *Nat. Commun.* **2015**, *6*, 1–8.
- [9] Sirringhaus, H., Brown, P.J., Friend, R.H., Nielsen, M.M., Bechgaard, K., Langeveld-Voss, B.M.W., Spiering, A.J.H., Janssen, R.A., Meijer, E.W., Herwig, P., De Leeuw, D.M. Two-dimensional charge transport in self-organized, high-mobility conjugated polymers. *Nature* **1999**, *401* (6754), 685-688.
- [10] Tsao, H.N., Cho, D.M., Park, I., Hansen, M.R., Mavrinskiy, A., Yoon, D.Y., Graf, R., Pisula, W., Spiess, H.W., Müllen, K. Ultrahigh mobility in polymer field-effect transistors by design. *J. Am. Chem. Soc.* **2011**, *133* (8), 2605-2612.
- [11] McCulloch, I., Heeney, M., Bailey, C.; Genevicius, K., Macdonald, I., Shkunov, M.; Sparrowe, D., Tierney, S., Wagner, R., Zhang, W., Chabinyc, M. L., Kline, R. J.,

- McGehee, M. D., Toney, M. F. Liquid-Crystalline Semiconducting Polymers with High Charge-Carrier Mobility. *Nat. Mater.* **2006**, 5 (4), 328–333.
- [12] Blinov, LM. *Structure and properties of liquid crystals*. Vol. 123. Springer Science & Business Media, **2010**.
- [13] Nagayasu, T., Oketani, T., Hirobe, T., Kato, H., Mizushima, S., Take, H., Yano, K., Hijikigawa, M., Washizuka, I. A 14-in.-diagonal full-color a-Si TFT LCD. In *Display Research Conference, Conference Record of the 1988 International* **1988**, 56-58.
- [14] Bushby, R.J., Kelly, S.M., O'Neill, M. eds. *Liquid crystalline semiconductors: materials, properties and applications*. Vol. 169. Springer Science & Business Media, **2012**.
- [15] Hanna, J.; Ohno, A.; Iino, H. Charge Carrier Transport in Liquid Crystals. *Thin Solid Films* **2014**, 554 (4), 58–63.
- [16] Funahashi, M., Tamaoki, N. Electronic conduction in the chiral nematic phase of an oligothiophene derivative. *ChemPhysChem.* **2006**, 7 (6), 1193-1197.
- [17] Tokunaga, K., Takayashiki, Y., Iino, H., Hanna, J. Electronic conduction in nematic phase of small molecules. *Phys. Rev. B* **2009**, 79 (3), 033201.
- [18] O'Neill, S. M., Kelly, S. M. Ordered Materials for Organic Electronics and Photonics. *Adv. Mater.* **2011**, 23, 566.
- [19] Funahashi, M. Nanostructured Liquid-Crystalline Semiconductors – A New Approach to Soft Matter Electronics *J. Mater. Chem. C* **2014**, 2 (36), 7451.
- [20] Vlachos, P., Mansoor, B., Aldred, M. P., O'Neill, M., Kelly, S. M. Charge-Transport in Crystalline Organic Semiconductors with Liquid Crystalline Order *Chem. Commun. (Camb)*. **2005**, 23, 2921–2923.
- [21] Van Breemen, A. J. J. M., Herwig, P. T., Chlon, C. H. T., Sweelssen, J., Schoo, H. F. M., Setayesh, S., Hardeman, W. M., Martin, C. A., de Leeuw, D. M., Valetton, J. J. P., Bastiaansen, C. W. M., Broer, D. J., Popa-Merticaru, A. R., Meskers, S. C. J. Large area liquid crystal monodomain field-effect transistors. *J. Am. Chem. Soc.* **2006**, 128 (7), 2336-2345.
- [22] Oikawa, K., Monobe, H., Nakayama, K. I., Kimoto, T., Tsuchiya, K., Heinrich, B., Guillon, D., Shimizu, Y., Yokoyama, M. High Carrier Mobility of Organic Field-Effect Transistors with a Thiophene–Naphthalene Mesomorphic Semiconductor. *Adv. Mater.* **2007**, 19 (14), 1864–1868.

- [23] Funahashi, M., Zhang, F., Tamaoki, N. High Ambipolar Mobility in a Highly Ordered Smectic Phase of a Dialkylphenylterthiophene Derivative That Can Be Applied to Solution-Processed Organic Field-Effect Transistors. *Adv. Mater.* **2007**, *19*, 353.
- [24] Funahashi, M. Development of Liquid-Crystalline Semiconductors with High Carrier Mobilities and their Application to Thin-Film Transistors. *Polym. J.* **2009**, *41* (6), 459-469.
- [25] Funahashi, M., Hanna, J. High Carrier Mobility up to $0.1 \text{ cm}^2 \text{ V}^{-1} \text{ s}^{-1}$ at Ambient Temperatures in Thiophene-Based Smectic Liquid Crystals. *Adv. Mat.* **2005**, *17* (5), 594-598.
- [26] Iino, H., Hanna, J. Availability of Liquid Crystallinity in Solution Processing for Polycrystalline thin films. *Adv. Mat.* **2011**, *23* (15), 1748-1751.
- [27] Zhou, K., Dong, H., Zhang, H.L., Hu, W. High Performance n-Type and Ambipolar Small Organic Semiconductors for Organic Thin Film Transistors. *Phys. Chem. Chem. Phys.* **2014**, *16*, 22448.
- [28] Eccher, J., Faria, G. C., Bock, H., von Seggern, H., Bechtold, I. H. Order Induced Charge Carrier Mobility Enhancement in Columnar Liquid Crystal Diodes. *ACS Appl. Mater. Interfaces* **2013**, *5* (22), 11935–11943.
- [29] Schmidt-Mende, L., Fechtenkötter, A., Müllen, K., Moons, E., Friend, R. H., MacKenzie, J. D. Self-Organized Discotic Liquid Crystals for High-Efficiency Organic Photovoltaics *Science* **2001**, *293* (5532), 1119–1122.
- [30] Sun, K., Xiao, Z., Lu, S., Zajaczkowski, W., Pisula, W., Hanssen, E., White, J. M., Williamson, R. M.; Subbiah, J., Ouyang, J., Holmes, A. B., Wong, W. W. H., Jones, D. J. A Molecular Nematic Liquid Crystalline Material for High-Performance Organic Photovoltaics *Nat. Commun.* **2015**, *6*, 1–9.
- [31] Soberats, B., Mayerhoeffer, U., Wuerthner, F. Liquid-Crystalline Squaraine Dyes with Anisotropic Absorption of Near Infrared Light *Adv. Opt. Mater.* **2016**, *4* (8), 1186–1189.
- [32] Metzger, R.M. Unimolecular and Supramolecular Electronics I: Chemistry and Physics Meet at Metal-Molecule Interfaces. Vol. 1. Springer Science & Business Media, **2012**.
- [33] Brütting, W., ed. *Physics of organic semiconductors*. John Wiley & Sons, **2006**.
- [34] Shirakawa, H., Louis, E.J., MacDiarmid, A.G., Chiang, C.K., Heeger, A.J. Synthesis of electrically conducting organic polymers: halogen derivatives of polyacetylene, $(\text{CH})_x$. *J. Chem. Soc., Chem. Com.* **1977**, *16*, 578-580.

- [35] Chiang, C.K., Fincher Jr., C.R., Park, Y.W., Heeger, A.J., Shirakawa, H., Louis, E.J., Gau, S.C., MacDiarmid, A.G., Electrical Conductivity in Doped Polyacetylene. *Phys. Rev. Lett.* **1977**, *39*, 1098-1101.
- [36] Tang, C. W. Two-layer organic photovoltaic cell. *Appl. Phys. Lett.* **1986**, *48* (2), 183-185.
- [37] Tang, C. W., VanSlyke, S. A. Organic electroluminescent diodes. *Appl. Phys. Lett.* **1987**, *51* (12), 913-915.
- [38] Farchioni, R., Grosso, G. (eds.), Organic Electronic Materials. Springer, Berlin, **2001**
- [39] Baranovski, S. (editor): *Charge transport in disordered solids*, Wiley Publishing, Chichester, **2006**
- [40] Amaresh, M., Bäuerle, P. Small molecule organic semiconductors on the move: promises for future solar energy technology. *Ang. Chem. Int. Edition* **2012**, *51* (9), 2020-2067.
- [41] Huang, Q.L., and Li, H.X. Recent progress of bulk heterojunction solar cells based on small-molecular donors. *Chin. Sc. Bull.* **2013**, *58* (22), 2677-2685.
- [42] Sirringhaus, H. Device physics of solution-processed organic field-effect transistors. *Adv. Mat.* **2005**, *17* (20), 2411-2425.
- [43] Yook, K.S., Jun Y.L. Small molecule host materials for solution processed phosphorescent organic light-emitting diodes *Adv. Mat.* **2014**, *26* (25), 4218-4233.
- [44] Bäessler, H. Charge transport in disordered organic photoconductors a Monte Carlo simulation study. *Phys. Stat. sol. (b)* **1993**, *175* (1), 15-56.
- [45] Fishchuk, I. I., Arkhipov, V. I., Kadashchuk, A., Heremans, P., Bäessler, H. Analytic model of hopping mobility at large charge carrier concentrations in disordered organic semiconductors: Polarons versus bare charge carriers. *Phys. Rev. B* **2007**, *76* (4), 045210.
- [46] Miller A., Abrahams, E. Impurity conduction at low concentrations. *Phys. Rev.* **1960**, *120* (3), 745.
- [47] Dirk, H., Bäessler, H. Photoconduction in amorphous organic solids. *ChemPhysChem.* **2008**, *9* (5), 666-688.
- [48] Arkhipov, V. I., Emelianova, E. V., Adriaenssens, G. J. Effective transport energy versus the energy of most probable jumps in disordered hopping systems. *Phys. Rev. B* **2001**, *64* (12), 125125.
- [49] Monroe, D. Hopping in exponential band tails *Phys. Rev. Lett.* **1985**, *54* (2), 146.

- [50] Arkhipov, V. I., Emelianova, E. V., H. Bässler. Equilibrium carrier mobility in disordered hopping systems. *Phil. Mag. B* **2001**, 81 (9), 985-996.
- [51] Emelianova, E. V., Adriaenssens, G. J. Stochastic approach to hopping transport in disordered organic materials. *J. Opto. Adv. Mater* **2004**, 6 (4), 1105-1131.
- [52] Baranovskii, S. D., Faber T., Hensel F., Thomas P. The applicability of the transport-energy concept to various disordered materials. *J. Phys. Cond. Matt.* **1997**, 9 (13), 2699.
- [53] Sirringhaus, H. Organic semiconductors: An equal-opportunity conductor *Nat. Mater.* **2003**, 2 (10), 641-642.
- [54] Rivnay, J., Jimison, L. H., Northrup, J. E., Toney, M. F., Noriega, R., Lu, S., Marks, T. J., Facchetti, A., Salleo, A. Large Modulation of Carrier Transport by Grain-Boundary Molecular Packing and Microstructure in Organic Thin Films. *Nat. Mater.* **2009**, 8 (12), 952-958.
- [55] Horowitz, G., Hajlaoui, M.E. Mobility in Polycrystalline Oligothiophene Field-Effect Transistors Dependent on Grain Size. *Adv. Mater.* **2000**, 12 (14), 1046-1050.
- [56] Weis, M., Gmucová, K., Nádaždy, V., Majková, E., Haško, D., Taguchi, D., Manaka, T. Iwamoto, M. Grain boundary effect on charge transport in pentacene thin films *Jap. J. Appl. Phys.* **2011**, 50 (4S), 04DK03.
- [57] Reinitzer, F. Beiträge zur Kenntniss des Cholesterins. *Wiener Monatschr, Für Chem.* **1888**, 9 (1), 421-441.
- [58] Lehmann, O. Über fließende Krystalle *Z. Phys. Chem.* **1889**, 4 (1), 462-472.
- [59] Kawamoto H. The history of liquid-crystal displays. *Proc. IEEE.* **2002**, 90 (4), 460-500.
- [60] Heilmeyer, G. H., Zanoni, L. A., Barton, L. A. Dynamic scattering: A new electrooptic effect in certain classes of nematic liquid crystals. *Proc. IEEE.* **1968**, 56 (7), 1162-1171.
- [61] Mito, S., Wada, T. Application of liquid crystal to COS (calculator on substrate) system electronic calculator. *Proc. 5th Int. Liq. Cryst. Conf.* **1974**, 247-248.
- [62] Stephen, M. J., Straley, J.P. Physics of liquid crystals. *Rev. Mod. Phys.* **1974**, 46 (4), 617.
- [63] Li, Q. Nanoscience with liquid crystals *Cham: Springer.* **2014**.
- [64] Andrienko D. Introduction to liquid crystals *IMPRS school, Bad Marienberg.* **2006**.

- [65] *materials.duke.edu/XCOURSES/ME83/lcrystals2.pdf*
- [66] Kusabayashi, S., Labes, M.M. Conductivity in liquid crystals. *Mol. Cryst. Liq. Cryst.* **1969**, 7 (1), 395–405.
- [67] Heilmeyer, G.H., Heyman, P.M. Note on transient current measurement in liquid crystals and related systems. *Phys. Rev. Lett.* **1967**, 18 (15), 583–585.
- [68] Chandrasekhar, S., Sedaschiva, B.K., Suresh, K.A. *Pramana* **1977**, 9 (5), 471–480.
- [69] Boden, N., Bushby, R.J., Clements, J., Jesudason, M.V., Knowles, P.F., Williams, G. Onedimensional electronic conductivity in discotic liquid crystals. *Chem. Phys. Lett.* **1988**, 152 (1), 94–99.
- [70] Boden, N., Bushby, R.J., Clements, J., Movaghar, B., Donovan, K.J., Kreuzer, T. Mechanism of charge transport in discotic liquid crystals. *Phys. Rev. B.* **1995**, 52 (18), 13274–13280.
- [71] Arikainen, E.O., Boden, N., Bushby, R.J., Clements, J., Movaghar, B., Wood, A. Effects of side-chain length on the charge transport properties of discotic liquid crystals and their implications for the transport mechanism. *J. Mater. Chem.* **1995**, 5 (12), 2161–2165.
- [72] Adam, D., Closs, F., Frey, T., Funhoff, D., Haarer, D., Schuhmacher, P., Siemensmeyer, K. Transient photoconductivity in a discotic liquid crystal. *Phys. Rev. Lett.* **1993**, 70 (4), 457–460.
- [73] Funahashi, M., Hanna, J. Fast hole transport in a New calamitic liquid crystal of 2-(40-heptyloxyphenyl)-6-dodecylthiobenzothiazole. *Phys. Rev. Lett.* **1997**, 78 (11), 2184–2187
- [74] Tokunaga, K., Iino, H., Hanna, J. Reinvestigation of carrier transport properties in liquid crystalline 2-phenylbenzothiazole derivatives. *J. Phys. Chem. B.* **2007**, 111 (42), 12041–12044.
- [75] Funahashi, M., Hanna, J. Fast ambipolar carrier transport in smectic phases of phenylnaphthalene liquid crystal. *Appl. Phys. Lett.* **1997**, 71 (5), 602–604.
- [76] Feng, X., Marcon, V., Pisula, W., Hansen, M. R., Kirkpatrick, J., Grozema, F., Andrienko, D., Kremer, K., Müllen, K. Towards High Charge-Carrier Mobilities by Rational Design of the Shape and Periphery of Discotics. *Nat. Mater.* **2009**, 8 (5), 421–426.
- [77] Iino, H., Hanna, J., Haarer, D. Electronic and ionic carrier transports in discotic liquid crystalline photoconductor. *Phys. Rev. B.* **2005**, 72 (19), 193203–193206.

- [78] Iino, H., Hanna, J. Electronic and ionic transports for negative charge carriers in smectic liquid crystalline photoconductor. *J. Phys. Chem. B.* **2005**, *109* (47), 22120–22125.
- [79] Ahn, H., Ohno, A., Hanna, J. Impurity effects on charge carrier transport in various mesophases of smectic liquid crystals. *J. Appl. Phys.* **2007**, *102* (9), 093718.
- [80] Said, S.M., Mahmood, M.S., Daud, M.N., Mohd Sabri, M.F., Sairi, N.A. Structure-electronics relations of discotic liquid crystals from a molecular modelling perspective. *Liq. Cryst.* **2016**, 1-22.
- [81] Kirkpatrick, J. An approximate method for calculating transfer integrals based on the ZINDO Hamiltonian. *Int. J. Quant. Chem.* **2008**, *108* (1), 51-56
- [82] Sergeev, S., Pisula, W., Geerts, Y. H. Discotic liquid crystals: a new generation of organic semiconductors. *Chem. Soc. Rev.* **2007**, *36* (12), 1902-1929.
- [83] Wöhrle, T., Wurzbach, I., Kirres, J., Kostidou, A., Kapernaum, N., Litterscheidt, J., Haenle, J. C., Staffeld, P., Baro, A.; Giesselmann, F., Laschat, S. Discotic Liquid Crystals. *Chem. Rev.* **2016**, *116* (3), 1139–1241.
- [84] Kaafarani, B. R. Discotic Liquid Crystals for Opto-Electronic Applications. *Chem. Mater.* **2011**, *23* (3), 378–396.
- [85] Tokunaga, K., Takayashiki, Y., Iino, H., Hanna, J. One-dimensional to three-dimensional electronic conduction in liquid crystalline mesophases. *Mol. Cryst. Liq. Cryst.* **2009**, *510* (1), 250–1384.
- [86] Mery, S., Haristoy, D., Nicoud, J.-F., Guillon, D., Diele, S., Monobe, H., Shimizu, Y. Bipolar carrier transport in a lamello-columnar mesophase of a sanidic liquid crystal. *J. Mater. Chem.* **2002**, *12* (1), 37–41.
- [87] Iino, H., Hanna, J., Haarer, D., Bushby, R.J. Fast electron transport in discotic columnar phases of triphenylene derivatives *Jpn. J. Appl. Phys.* **2006**, *45* (1S), 430–433.
- [88] Iino, H., Takayashiki, Y., Hanna, J., Bushby, R.J. Fast ambipolar carrier transport and easy homeotropic alignment in a metal free phthalocyanine derivative *Jap. J. Appl. Phys.* **2005**, *44* (10L), L1310–L1312.
- [89] Maeda, H., Funahashi, M., Hanna, J. Effect of grain boundary on carrier transport of calamitic liquid crystalline photoconductive materials. *Mol. Cryst. Liq. Cryst.* **2000**, *346* (1), 183–192.

- [90] Maeda, H., Funahashi, M., Hanna, J. Electrical properties of domain boundaries in photoconductive smectic mesophases and their crystal phases. *Mol. Cryst. Liq. Cryst.* **2001**, 366 (1), 369–376.
- [91] Zhang, H., Hanna, J. High $\mu \tau$ product in a smectic liquid crystalline photoconductor of a 2-phenylnaphthalene derivative. *Appl. Phys. Lett.* **2004**, 85 (22), 5251-5253.
- [92] Barsoukov, E., Macdonald, J.R. eds. *Impedance spectroscopy: theory, experiment, and applications*. John Wiley & Sons, **2005**.
- [93] Martens, H.C.F., Brom, H.B., Blom, P.W.M.. Frequency-dependent electrical response of holes in poly (p-phenylene vinylene) *Phys. Rev. B* **1999**, 60 (12), R8489.
- [94] Martens, H.C.F., Huiberts, J.N., Blom, P.W.M. Simultaneous Measurement of Electron and Hole Mobilities in Polymer Light-Emitting Diodes. *Appl. Phys. Lett.* **2000**, 77 (12), 1852–1854.
- [95] Tsang, S. W., So, S. K., Xu, J. B. Application of Admittance Spectroscopy to Evaluate Carrier Mobility in Organic Charge Transport Materials. *J. Appl. Phys.* **2006**, 99 013706.
- [96] Tripathi, D.C., Tripathi, A.K., Mohapatra, Y.N. Mobility Determination using Frequency Dependence of Imaginary Part of Impedance ($\text{Im } Z$) for Organic and Polymeric Thin Films. *Appl. Phys. Lett.* **2011**, 98, 033304.
- [97] Kokil, A., Yang, K., Kumar, J. Techniques for characterization of charge carrier mobility in organic semiconductors. *J. Polym. Sc. Part B: Polym. Phys.* **2012**, 50 (15), 1130-1144.
- [98] Child, C.D. Discharge from hot CaO. *Phys. Rev. (Series I)* **1911**, 32 (5), 492.
- [99] Mott, N.F., Gurney, R.W. *Electronic processes in ionic crystals*. Clarendon Press, **1948**.
- [100] Lampert, M.A., Mark, P. *Current injection in solids*. Academic Press, **1970**.
- [101] Wang, Z.B., Helander, M.G., Greiner, M.T., Qiu, J., Lu, Z.H. Carrier mobility of organic semiconductors based on current-voltage characteristics. *J. Appl. Phys.* **2010**, 107 (3), 034506.
- [102] Blakesley, J. C., Castro, F. A., Kylberg, W., Dibb, G. F., Arantes, C., Valaski, R., Kim, J. S. Towards reliable charge-mobility benchmark measurements for organic semiconductors. *Org. Elect.* **2014**, 15 (6), 1263-1272.

- [103] Yoshimoto, N., Hanna, J. I. A novel charge transport material fabricated using a liquid crystalline semiconductor and crosslinked polymer. *Adv. Mater.* **2002**, *14* (13-14), 988-991.
- [104] Kim, B. G., Jeong, E. J., Chung, J. W., Seo, S., Koo, B., Kim, J. A molecular design principle of lyotropic liquid-crystalline conjugated polymers with directed alignment capability for plastic electronics. *Nat. Mater.* **2013**, *12* (7), 659-664.
- [105] Zhang, G., Zhang, K., Yin, Q., Jiang, X.F., Wang, Z., Xin, J., Ma, W., Yan, H., Huang, F., Cao, Y. High-Performance Ternary Organic Solar Cell Enabled by a Thick Active Layer Containing a Liquid Crystalline Small Molecule Donor. *J. Am. Chem. Soc.* **2017**, *139* (6), 2387-2395.
- [106] Kumar, M., Kumar, S. Liquid crystals in photovoltaics: a new generation of organic photovoltaics. *Polym. J.* **2016**.
- [107] O'Neill, M., Kelly, S. M. Liquid crystals for charge transport, luminescence, and photonics. *Adv. Mater.* **2003**, *15* (14), 1135-1146.
- [108] Huang, F., Wu, H., Wang, D., Yang, W., Cao, Y. Novel electroluminescent conjugated polyelectrolytes based on polyfluorene. *Chem. Mater.* **2004**, *16* (4), 708-716.
- [109] He, Z., Zhong, C., Su, S., Xu, M., Wu, H., Cao, Y. Enhanced power-conversion efficiency in polymer solar cells using an inverted device structure. *Nat. Phot.* **2012**, *6* (9), 591-595.
- [110] Yeh, P., Gu, C. *Optics of liquid crystal displays*. Vol. 67. John Wiley & Sons, **2010**.
- [111] Liu, S. G., Sui, G., Cormier, R. A., Leblanc, R. M., Gregg, B. A. Self-Organizing Liquid Crystal Perylene Diimide Thin Films: Spectroscopy, Crystallinity, and Molecular Orientation. *J. Phys. Chem. B* **2002**, *106* (6), 1307-1315.
- [112] Megow, J., Körzdörfer, T., Renger, T., Sparenberg, M., Blumstengel, S., Henneberger, F., May, V. Calculating Optical Absorption Spectra of Thin Polycrystalline Organic Films: Structural Disorder and Site-Dependent van der Waals Interaction. *J. Phys. Chem. C* **2015**, *119* (10), 5747-5751.
- [113] Scher, H., Montroll, E. W., Anomalous transit-time dispersion in amorphous solids. *Phys. Rev. B* **1975**, *12*, 2455-2477.
- [114] Di Carlo, A., Piacenza, F., Bolognesi, A., Stadlober, B., Maresch, H. Influence of Grain Sizes on the Mobility of Organic Thin-Film Transistors. *Appl. Phys. Lett.* **2005**, *86* (26), 263501.

- [115] Kirsch, P., Tong, Q., Untenecker, H. Crystal Design using Multipolar Electrostatic Interactions: A Concept Study for Organic Electronics Beilstein J. Org. Chem. **2013**, 9 (1), 2367–2373.
- [116] Párkányi, C. ed. *Theoretical organic chemistry*. Vol. 5. Elsevier, **1997**.
- [117] Yuan, J., Ford, M.J., Zhang, Y., Dong, H., Li, Z., Li, Y., Nguyen, T-Q., Bazan, G.C., Ma, W. Toward Thermal Stable and High Photovoltaic Efficiency Ternary Conjugated Copolymers: Influence of Backbone Fluorination and Regioselectivity. *Chem. Mater.* **2017**, 29 (4), 1758-1768
- [118] Mariaca, R., Behrnd, N. R., Eggli, P., Stoeckli-Evans, H., Hulliger, J. Synthesis and crystal engineering of fluorinated stilbenes. *CrystEngComm.* **2006**, 8 (3), 222-232.
- [119] Mariaca, R., Labat, G., Behrnd, N. R., Bonin, M., Helbling, F., Eggli, P., Hulliger, J. Preparation of donor–acceptor substituted fluorostilbenes and crystal chemistry of fluorinated (E)-4-(4-halogeno-styryl)-benzonitriles. *J. Fluor. Chem.* **2009**, 130 (2), 175-196.
- [120] Neretin, I. S., Lyssenko, K. A., Antipin, M. Y., Slovokhotov, Y. L., Boltalina, O. V., Troshin, P. A., Lukonin, A.Y., Sidorov, L.N., Taylor, R. C~ 6~ 0F~ 1~ 8, a Flattened Fullerene: Alias a Hexa-Substituted Benzene. *Ang. Chem.* **2000**, 39 (18), 3273-3276.
- [121] Kozhevina, L. I., Prokopenko, E. B., Rybachenko, V. I., Titov, E. V. The vibrational spectra and force constants of benzylideneaniline and its fluoroderivatives. *J. Mol. Struct.* **1993**, 295, 53-72.
- [122] Yadav, R. A., Singh, I. S. Vibrational studies of trifluoromethyl benzene derivatives— III. p-trifluoromethyl aniline. *Spec. Acta Part A: Mol. Spec.* **1985**, 41(1-2), 191-197.
- [123] Funahashi, M., Hanna, J. High ambipolar carrier mobility in self-organizing terthiophene derivative. *Appl. Phys. Lett.* **2000**, 76 (18), 2574-2576.
- [124] Funahashi, M., Zhang, F., Tamaoki, N. High Ambipolar Mobility in a Highly Ordered Smectic Phase of a Dialkylphenylterthiophene Derivative That Can Be Applied to Solution-Processed Organic Field-Effect Transistors. *Adv. Mater.* **2007**, 19 (3) 353-358
- [125] a) J. Heinze, B. A. Frontana-Uribe, S. Ludwigs, *Chem. Rev.* **2010**, 110, 4724–4771. b) Inzelt, G. *Conducting Polymers*; Springer, Heidelberg, **2008**. c) Freund, M. S., Deore, B. *Self-Doped Conducting Polymers*; Wiley, Chichester, **2007** d) Skotheim, T. A., Reynolds, J. R. *Handbook of Conducting Polymers*, 3rd ed.; CRC Press, Boca Raton, FL, **2007**. e) Kuzmany, H., Mehring, M., Roth, S. *Electronic Properties of Conjugated Polymers*, Springer, Berlin/Heidelberg, **1987**.

- [126] a) M. Giulianini, E. R. Waclawik, J. M. Bell, N. Motta, *Appl. Phys. Lett.* **2009**, *94*, 083302-1–083302-3. b) C. Goh, R. J. Kline, M. D. McGehee, E. N. Kadnikova, J. M. J. Fréchet, *Appl. Phys. Lett.* **2005**, *86*, 122110-1.
- [127] ^{a)} R. J. Kline, M. D. McGehee, E. N. Kadnikova, J. Liu, J. M. J. Fréchet, *Adv. Mater.* **2003**, *15*, 1519–1522. b) R. J. Kline, M. D. McGehee, E. N. Kadnikova, J. Liu, J. M. J. Fréchet, M. F. Toney, *Macromolecules* **2005**, *38*, 3312–3319. c) A. Zen, J. Pflaum, S. Hirschmann, W. Zhuang, F. Jaiser, U. Asawapirom, J. P. Rabe, U. Scherf, D. Neher, *Adv. Funct. Mater.* **2004**, *14*, 757–764.
- [128] Steyrlleuthner, R., Di Pietro, R., Collins, B. A., Polzer, F., Himmelberger, S., Schubert, M., Facchetti, A. The role of regioregularity, crystallinity, and chain orientation on electron transport in a high-mobility n-type copolymer. *J. Am. Chem. Soc.* **2014**, *136* (11), 4245-4256.
- [129] Facchetti, A., Yoon, M. H., Stern, C. L., Katz, H. E., Marks, T. J. Building Blocks for n-Type Organic Electronics: Regiochemically Modulated Inversion of Majority Carrier Sign in Perfluoroarene-Modified Polythiophene. Semiconductors. *Ang. Chem. Int. Edition* **2003**, *42* (33), 3900-3903.
- [130] Letizia, J. A., Facchetti, A., Stern, C. L., Ratner, M. A., Marks, T. J. High Electron Mobility in Solution-Cast and Vapor-Deposited Phenacyl– Quaterthiophene-Based Field-Effect Transistors: Toward N-Type Polythiophenes. *J. Am. Chem. Soc.* **2005**, *127* (39), 13476-13477.
- [131] Facchetti, A., Mushrush, M., Katz, H. E., Marks, T. J. n-type building blocks for organic electronics: a homologous family of fluorocarbon-substituted thiophene oligomers with high carrier mobility. *Adv. Mater.* **2003**, *15* (1), 33-38.
- [132] Clarke, T. M., Lungenschmied, C., Peet, J., Drolet, N., Mozer, A. J. A comparison of five experimental techniques to measure charge carrier lifetime in polymer/fullerene solar cells. *Adv. Energy Mater.* **2015**, *5*(4).
- [133] Pasveer, W. F., Cottaar, J., Tanase, C., Coehoorn, R., Bobbert, P.A., Blom, P.W.M., De Leeuw, D.M, Michels, M.A.J. Unified description of charge-carrier mobilities in disordered semiconducting polymers. *Phys. Rev. Lett.* **2005**, *94* (20), 206601.
- [134] Foertig, A., Baumann, A., Rauh, D., Dyakonov, V., Deibel, C. Charge carrier concentration and temperature dependent recombination in polymer-fullerene solar cells. *Appl. Phys. Lett.* **2009**, *95* (5), 052104.
- [135] Takagi, K., Abe, S., Nagase, T., Kobayashi, T., Naito, H. Characterization of transport properties of organic semiconductors using impedance spectroscopy. *J. Mater. Science: Mater. Elect.* **2015**, *26* (7), 4463-4474.

- [136] Takata, M., Kouda, N., Ishihara, S., Nagase, T., Kobayashi, T., Naito, H. Effect of contact resistance on mobility determination by impedance spectroscopy. *Jap. J. Appl. Phys.* **2014**, 53 (2S), 02BE02.
- [137] Okachi, T., Nagase, T., Kobayashi, T., Naito, H. Influence of injection barrier on the determination of charge-carrier mobility in organic light-emitting diodes by impedance spectroscopy. *Thin Solid Films* **2008**, 517 (4), 1331-1334.
- [138] Helander, M. G., Wang, Z. B., Lu, Z. H. Chlorinated indium tin oxide as a charge injecting electrode for admittance spectroscopy. *Org. Elect.* **2011**, 12 (9), 1576-1579.
- [139] Okachi, T., Nagase, T., Kobayashi, T., Naito, H. Determination of charge-carrier mobility in organic light-emitting diodes by impedance spectroscopy in presence of localized states. *Jap. J. Appl. Phys.* **2008**, 47 (12R), 8965.
- [140] Brütting, W., Berleb, S., Mückl, A. G. Device physics of organic light-emitting diodes based on molecular materials. *Org. Elect.* **2001**, 2 (1), 1-36.
- [141] Costa, J. C., Taveira, R. J., Lima, C. F., Mendes, A., Santos, L. M. Optical band gaps of organic semiconductor materials. *Opt. Mater.* **2016**, 58, 51-60.
- [142] New, E., Howells, T., Sullivanand, P., Jones, T. S. Small molecule tandem organic photovoltaic cells incorporating an α -NPD optical spacer layer. *Org. Elect.* **2013**, 14 (9), 2353-2359.
- [143] Davids, P. S., Campbell, I. H., Smith, D. L. Device model for single carrier organic diodes. *J. Appl. Phys.* **2013**, 82 (12), 6319-6325.
- [144] Liu, C. Y., Chen, S. A. Charge mobility and charge traps in conjugated polymers. *Macrom. Rapid Comm.* **2007**, 28 (17), 1743-1760.
- [145] Nešpůrek, S., Zmeškal, O., Sworakowski, J. Space-charge-limited currents in organic films: Some open problems. *Thin Solid Films* **2008**, 516 (24), 8949-8962.

Publications and Conference contributions

Publications

Tchamba Yimga, N. Boehme, S., Achidi, F., Borchert H., Parisi, J. Kirsch, P. & von Hauff, E. "In preparation" *J. Am. Chem. Soc.* **2017**.

Tchamba Yimga, N., Ramanan, C., Borchert, H., Parisi, J., Untenecker, H., Kirsch, P., & von Hauff, E. Interplay between long range crystal order and short range molecular interactions tunes carrier mobility in liquid crystal dyes. *ACS Appl. Mater. Interfaces* **2017**, 9(7), 6228.

Jäger, J., **Tchamba Yimga N.**, Urdanpilleta, M., von Hauff, E., & Pammer, F. "Toward n-type analogues to poly (3-alkylthiophene) s: influence of side-chain variation on bulk-morphology and electron transport characteristics of head-to-tail regioregular poly (4-alkylthiazole) s." *J. Mater. Chem. C* **2016**, (4) 2587-2597.

Conferences and workshops

Controlling the Electronic Properties in Liquid Crystal Conjugated Small Molecules for Application in Electronics; **N. Tchamba Yimga**, C. Ramanan, H. Borchert, J. Parisi, P. Kirsch, and E. von Hauff; MRS Spring Meeting, 28.03.2016 - 01.04.2016; Phoenix, Arizona, USA; Participation with an **ORAL** presentation.

Controlling the Electronic Properties in Liquid Crystal Conjugated Small Molecules for Application in Electronics; **N. Tchamba Yimga**, C. Ramanan, H. Borchert, J. Parisi, P. Kirsch, and E. von Hauff; DPG Spring Meeting, 06.03.2016 - 11.03.2016; Regensburg, Germany; Participation with an **ORAL** presentation.

Novel donor material inspired by liquid crystals for application in organic photovoltaics; **N. Tchamba Yimga**, C. Ramanan, A. Chanaewa, Leo Polak, A. Peukert, P. Kirsch, & E. von Hauff; 578th. Heraeus-Workshop: Charge Transfer Effects in Organic Heterostructures, 09-12 December 2014, Bad Honnef, Germany. Participation with a **POSTER** presentation.

June 2015: Attended the 65th Lindau Nobel Laureates Meetings, 28th June - 03rd July 2015, Lindau, Germany. Selected as Young Scientist to attend Lectures and Discussion Panels given and held by a total of 70 Nobel Laureates in Physics, Chemistry and Physiology.

June 2014: Selected amongst the 15 participants, for the Sophia Workshop on Analytical Tools for PV, 25.06. - 27.06.2014, Helmholtz-Zentrum Berlin. Experience got in Surface sensitive Synchrotron based materials analysis and Multi resonance EPR/EDMR for film characterization in PV/OPV

Acknowledgements

PhD is a long journey which I couldn't take till the end, without helping minds, supportive hands and loving hearts carrying me all along. Having come to the point of achievement, I want to express here with my heart what I cannot express with my head.

I express my full gratitude to Prof. Dr. Jürgen Parisi, for the great opportunity you gave me to do my PhD work in your group, and for all the scientific support and help provided all along.

My sincere and deep gratitude to Prof Dr. Elizabeth von Hauff for her excellent scientific supervision during my PhD journey. Thanks you Liz, for your ability to create such a highly motivated atmosphere for scientific work and fruitful discussions. I am very grateful for the wonderful scientific experience I have acquired working with you. And beside Science, it has also been a nice human experience.

I thank Prof. Dr. Veit Wagner, for the time you spent reading through my thesis and also for have taken time for my defense.

I sincerely thank PD Dr. Holger Borchert, for the scientific support and advice during my PhD. Thank you Holger, to have so warmly welcomed me to the group in Oldenburg, and for all the inputs you brought to my work. Thanks also for helping me translating my Abstract in German.

I am thankful to Prof Dr. Peer Kirsch, our industrial partner at MERCK for this project. Thanks a lot Peer, for providing all the liquid crystal dyes we used in this work. Thanks also for the time spent performing all the calculations we needed to understand and interpret our results. Thank you for your scientific support, and such a fruitful cooperation.

I would also express my full gratitude to the German Academic Exchange Service (DAAD) for their financial support. My studies in Germany have been made possible only through a fully founded scholarship supported by DAAD.

My sincere gratitude to Dr. Charusheela Ramanan, Dr. Simon Boehme and Dr. Alina Chanaewa. Thanks a lot Sheela for you keen sense of science and the fruitful discussions we had. Thanks for your help with optical measurements and your involvement in the project to make it a success. Thanks a lot Simon for your help with the Raman measurements and for all

the inputs you brought in interpreting them. And to you Alina, who took part in this project from the very beginning in Freiburg. Thanks a lot for all your inputs particularly when it concerns Chemistry, that have been so helpful to me.

Thank you to Ulf Mikolajczak, Matthias Macke and Martin Slaman for the wonderful technical assistance in the Lab in Oldenburg and in Amsterdam. Thanks a lot Ulf for always being available when I needed your help with the XRD. Thanks Mathias for always being there when I needed your support in the Lab. And to you Martin, for all your help during all my stays in Amsterdam.

I would also like to thank all my scientific colleagues and Lab partners from HSEC group in Amsterdam and EHF group in Oldenburg, to have made my working days lighter and enjoyable. A special mention to Andreas Peukert, Tulus, Rany Miranti, Dorothea Scheunemann, Mohamed Sayed and Fabio Salas. It has been nice sharing my PhD journey with you guys.

I now come to those, though being most of the time far from eyes, are always in my heart. I want to express my gratitude to my family and love ones. I dedicate this work to You, my Lovely Mum Jeanne. Thank you to my Siblings: Narcisse, Sylviane, Ranese and Michael. Thanks for your love, affection, prayers and unending support and patience. If I have spent hours and efforts to accomplish what I did, you've spent much more supporting me and loving me unconditionally!

A special Thank to my elder Sister and "second Mum" Anthianniste Pamen. What should I say? Simply Thank you for always being there when I need you, being so patient, kind and affectionate. Thanks for your love, and unceasing prayers to support and bless me.

I would also thank my Brother in law, Roger Teukam for your love and affection. Thank you for always encouraging me, pushing me to give my best. Thank you also for your prayers.

To my little Angels: Yoann, Dave, Eliel, Gaius, Atniel, Naomi Leah, Seraya Anaëlle and Lois. Though not being much aware of what "Aunty" was doing, you had always being there for her. With your smiling faces and tender affection, you always gave me the motivation to do my best when things got tough.

I thank FFL, my "Friend for life" family: Solange, Carine, William, Ariel, Cyrille, Denis and Francine. As the Bible says, there are friends that are closer than a brother...and this is exactly what you have become for me guys, a Family! Thanks for your unending support and affection through all.

I thank Saustin Dongmo for his friendship and support. Thanks Saustin, for all the fun we had, and to have contributed in making my stay in Oldenburg enjoyable.

Thanks to All my Christian Family, my Beloved Brothers and Sisters in Freiburg, Amsterdam, Oldenburg and over. A special mention to Christelle Tsagueu. Your brotherly love and effective prayers have been so precious to me! Our Faithful Lord shall reward you All.

And the last but definitively the Highest, I thank You LORD and Saviour Jesus-Christ for all the strength, grace and peace that You granted me to accomplish this work.

Curriculum Vitae

Nadine Tchamba Yimga,

Born on 7th September 1987, in Bangangté, Cameroon.

ACADEMIC EXPERIENCE

May 2014 – September 2014: Wissenschaftliche Hilfskraft (Research Assistant), Albert-Ludwig University of Freiburg, Germany

October 2011 – March 2012: Research Assistant, University of Yaoundé I, Cameroon

ACADEMIC EDUCATION

Since October 2013: PhD Candidate in experimental Physics, Carl von Ossietzky Universität Oldenburg, Germany

Research project: The role of molecular packing on carrier transport in liquid crystalline dyes

August 2012 - June 2013: **Master of Science**, AIMS and University of Western Cape, South Africa

Major: Physics, Mathematics, and Computing.

Research project: Conception, fabrication and Characterization of a Zinc oxide piezoelectric nanogenerator

November 2008 - April 2011: **Master of Science**, University of Yaoundé I (UYI), Cameroon

Majors: Condenser Matter, Materials Science

Research project: Ab-initio calculation of physical properties of chalcogenide glasses.

October 2005 -October 2008: **Bachelor of Science (Physics)**, University of Yaoundé I, Cameroon

HIGH SCHOOL EDUCATION

July 2005: School leaving certificate, Lycée Classique de Bangangté, Cameroon

SCHOLARSHIP AND GRANT

10.2013 - 06.2017: DAAD Scholarship holder, fellow from the German Academic Service Exchange (DAAD) for the completion of a PhD in Physics, in Germany

08.2012 - 07.2013: AIMS Scholarship for a one year Master program at the African Institute of Mathematical Science (AIMS) in South Africa, registered as student at the University of Western Cape.

04.10.2016 - 18.11.2016: IPID4all Travel Grant, for a research stay at Vrije University Amsterdam (VU), to conduct optical spectroscopy at the Laser-lab as well as electrical characterization on novel conjugated liquid crystal dyes. IPID4all is a DAAD research grant for Mobile Doctorates in System Integration of Renewable Energy.

March 2016: IPID4all Travel-grant Conference, for MRS Spring Meeting in Phoenix, Arizona, USA from 28.3.-1.4.2016.

Erklärung

I declare that I have authored this thesis independently, that I have not used other sources/resources than the declared ones, and that I have explicitly indicated all material which has been quoted either literally or by content from the sources used.

Oldenburg, den 12.04.2017

Nadine Tchamba Yimga